UV writing of advanced Bragg gratings in optical waveguides

Jensen, Jesper Bo Damm

Publication date:
2002

Document Version
Publisher's PDF, also known as Version of record

UV writing of advanced Bragg gratings in optical waveguides

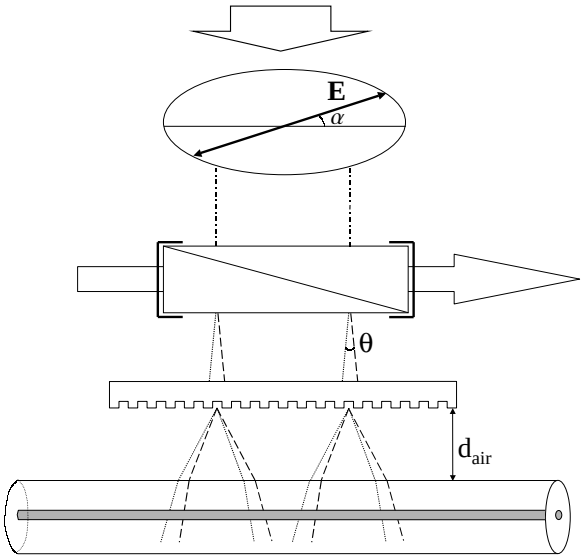

Jesper Bo Damm Jensen
Research Center COM,
Technical University of Denmark.
Ph.D. thesis, July 2002

Abstract

The subject of this Ph.D. thesis is the fabrication of Bragg gratings in optical waveguides. During the study Bragg gratings were written in both planar waveguides and optical fibers using pulsed or continuous-wave lasers operating in the ultraviolet (UV) range. The main result is the development of the novel polarization control method for UV writing of Bragg gratings with advanced apodization profiles including phase shifts. The principle of the polarization control method relies on a spatial separation of the s- and p-polarized components of a linearly polarized UV beam corresponding to half the periodicity of the index modulation profile in the Bragg grating. A phase shift in the grating is realized by shifting the UV irradiance from one polarization to the other during the grating inscription. The amplitude of the modulation can also be varied continuously by changing the ratio between the irradiance in the two polarizations, thus allowing for the inscription of any desired apodization profile including several phase shifts. Bragg gratings with specific amplitude and phase responses were designed using commercial available software. The resulting modulation amplitude profile and phase shifts were then translated into a polarizer angle profile and the Bragg grating were written using a pulsed excimer laser. Only optical fibers were used in this part of the thesis.
The high quality planar waveguides used during the study were produced in the cleanroom facility at the Microelectronic Center, Technical University of Denmark. During fabrication the planar waveguides were annealed in an oxygen rich atmosphere. This reduces the photosensitivity to a negligible level and Bragg gratings cannot be written within reasonable time unless the waveguides are sensitized by deuterium loading. Samples were hence loaded at either 100 bar or 1800 bar prior to the UV exposure. Bragg gratings with uniform coupling strength throughout the grating and apodized gratings were realized by scanning the UV beam along the waveguide with a computer controlled velocity profile. The excellent agreement between simulated and measured spectra indicated that the fabricated planar waveguides were of a very high quality.

Resume

Emnet for denne Ph.D. afhandling er fremstilling af Bragg gitre i optiske bølgeledere. I løbet af studiet blev der skrevet gitre i både planare bølgeledere og optiske fibre ved brug af enten pulserede eller continuous-wave lasere. Alle anvendte lasere udsendte lys i det ultraviolette (UV) område.
Hovedresultatet i denne afhandling er udviklingen af den nye polarisations kontrol metode til fremstilling af Bragg gitre med avancerede apodiserings profiler inklusiv multiple fase skift. Princippet i den nye metode kræver en rumlig adskillelse af s- og p-komponenterne af en lineært polariseret UV stråle svarende til en halv periode af modulations profilen i Bragg gitret. Ved at skifte UV intensiteten fra den ene til den anden polarisation under en gitter skrivning, kan der introduceres et fase skift i Bragg gitteret. Amplituden af modulationen i det refraktive indeks kan yderligere varieres kontinuert, hvilket tillader fremstilling af Bragg gitre med vilkårlige apodiserings profiler. Bragg gitre med specifikke spektrale egenskaber blev designet ved brug af kommerciel tilgængelig software. De resulterende modulation profiler blev oversat til en polarisator vinkel profil og Bragg gitrene blev UV skrevet ved brug af en pulset excimer laser. Til dette projekt blev der udelukkende anvendt optiske fibre.
Planare bølgeledere af særdeles høj kvalitet blev fremstillet i rent rums faciliteterne ved Microelectronik Centeret, Danmarks Tekniske Universitet. I løbet af fremstillingen blev prøverne annealet i oxygenrig atmosfære. Dette reducerer fotofølsomheden betragteligt og Bragg gitre kan kun skrives indenfor en rimelig tid, såfremt de planare bølgeledere bliver loadet med deuterium. I dette studie blev brugt to forskellige deuterium tryk i loading kammeret. Nogle prøver blev loadet ved 100 bar mens andre blev udsat for 1800 bar før UV belysning. Bragg gitre med konstant eller varierende koblingsstyrke blev fremstillet ved hjælp af en computerstyret translations motor. Den udemærkede overensstemmelse mellem simulerede og målte spectra indikerer, at de fremstillede planare bølgeledere er af overordentlig god kvalitet.

Acknowledgements

First of all I would like to thank my supervisors Martin Kristensen, Anders Bjarklev and Jörg Hübner for always having time to discuss both scientific and practical topics during my study. In the fabrication of planar waveguides a special thank goes to Dan A. Zauner for being a very patient tutor and Lasse Leick for being good companion in the cleanroom. Also a large thank to Haiyan Ou and Jean Marc Jouanno for the supply of additional planar waveguides for the experiments on ultra high pressure loaded waveguides and to Mikael Svalgaard and Kjartan Færch for the ultra high pressure loading. While working on the implementation of the polarization control method I have enjoyed a large number of hours in company with Poul Varming, Nikolai Plougmann, Hans-Jürgen Deyerl, Martin Kristensen and Henrik Rokkjær Sørensen. Furthermore I am grateful for the collaboration I have had during this study with my colleagues at Research Center COM, especially Carl Johan Marckmann, Nikolai Plougmann, Hans-Jürgen Deyerl, Poul Varming and others from the Bragg gratings and poling group. In my work with the construction of a continuous-wave laser based laboratory I have benefited greatly form the vast experience of Mikael Svalgaard and his never ending patience and willingness to share his knowledge with others. Furthermore a special thank to Hans-Jürgen Deyerl, Carl Johan Markcmann, Nikolai Plougmann, Mikael Svalgaard and Martin Kristensen for proof reading this thesis. Finally I am indebted to my family, who have been very supportive during my work on this thesis.

Publication list

This list summarize the publications produced during the study.

- J.B. Jensen, N. Plougmann, H.-J. Deyerl, P. Varming, J. Hübner, and M.Kristensen, "Polarization control method for UV writing of advanced Bragg gratings" *Opt. Lett.*, **27** (12), pp. 1004-1006 (2002)

- J.B. Jensen, P. Varming, B. Liu, and W. Gries, "Comparison of Photosensitivity in Germanium Doped Silica Fibers using 244nm and 266nm Continuous-Wave Lasers", in OSA *Trends in Optics and Photonics (TOPS) Vol 54, Optical Fiber Communication Conference OFC2001*, Technical Digest, Postconference Edition (Optical Society of America, Washington DC, 2001), pp. WDD90/1-WDD90/3

- J.B. Jensen, N. Plougmann, H.-J. Deyerl, and M. Kristensen, "Polarization controlled UV writing of Bragg gratings", in OSA *Trends in Optics and Photonics (TOPS) Vol 70, Optical Fiber Communication Conference OFC2002*, Technical Digest, (Optical Society of America, Washington DC, 2002), pp. TuQ4/1-TuQ4/3

- P. Varming, V.C. Lauridsen, J.H. Povlsen, J.B. Jensen, and M. Kristensen, "Design and fabrication of Bragg grating based DFB fiber lasers operating above 1610 nm" in OSA *Trends in Optics and Photonics (TOPS) Vol 37, Optical Fiber Communication Conference OFC2000*, Technical Digest, Postconference Edition (Optical Society of America, Washington DC, 2000), pp. 17-19 vol.3 (2000)

- P. Varming, J.B. Jensen, N. Plougmann, M. Kristensen, and J. Hübner, "New and simple method for fabrication of advanced UV written Bragg gratings", in OSA *Bragg Gratings, Photosensitivity, and Poling in Glass Waveguides*, OSA Technical Digest (Optical Society of America, Washington DC, 2001), paper BWA5-1

- H.-J. Deyerl, N. Plougmann, J.B. Jensen, J. El-Bez, H.R. Sørensen, C. Peucheret, and M. Kristensen, "Low-dispersion fibre Bragg gratings written using the polarization control method", to be presented at *ECOC2002, European Conference on Optical Communication (2002)*, Paper No. 07.2.7

- H.-J. Deyerl, N. Plougmann, J.B. Jensen, H.R. Sørensen, and M. Kristensen, "Polarization control method for UV-writing of advanced Bragg gratings" in *proceedings of WFOPC2002, Workshop on Fibre and Optical Passive Components,* pp. 86-91

- H.-J. Deyerl, H.R. Sørensen, J.B. Jensen, N. Plougmann, and M. Kristensen, "Fabrication and stability of fiber Bragg gratings for WDM applications using a 266nm CW laser", to be presented at *CLEO2003, Conference on Lasers and Electro-Optics (2003)*, session CTuI

- N. Plougmann, J.B. Jensen, H.-J. Deyerl, H.R. Sørensen, and M. Kristensen, "Polarization controlled UV writing of Bragg gratings", in *proceedings of the Summer School on Photosensitivity in Optical Waveguides and Glasses, POWAG2002*, Skt.Petersborg, (2002)

- M. Kristensen, J. Arentoft, J.B. Jensen, H.-J. Deyerl, J. Lægsgaard, C. J. Marckmann, N. Plougmann, Y. Ren, S. Søgaard, and P. Varming, "Bragg gratings and poling" *DOPS-NYT*, **2**, pp, 49-54 (2001)

Contents

Chapter 1

Introduction

The field of Bragg gratings in optical waveguides has experienced a tremendous development since the first fiber Bragg grating was produced by Hill *et al.* in 1978 [1]. This development has been motivated by the world wide growth in the use of optical communication in both high speed long haul communication links and metro systems. In wavelength division multiplexing (WDM) communication systems a large number of channels with individual wavelengths propagate simultaneously in the same fiber, thus increasing the capacity of the systems significantly. Integrated components such as arrayed waveguide gratings (AWG) can multiplex a large number of channels, N, onto a single fiber link and later demultiplex the signals into N different fibers. Bragg gratings cannot compete with AWG's or similar components when it comes to (de)multiplexing WDM signals. The cross-talk between adjacent channels and inherent loss, which both introduces a power penalty in the system and especially the component cost makes the AWG component less attractive when only a single channel is to be redirected or detected at certain network node. Bragg gratings on the other hand are ideal for such single-channel filtering with superior cost efficiency and cross-talk suppression.
With the increased demand for bandwidth the spectral properties of Bragg gratings has attracted much attention. In order to obtain a larger system capacity the channel spacing is reduced and a high utilization of the channel bandwidth is required. The strong side lobes appearing in the spectrum of a Bragg grating with uniform coupling strength, makes such gratings less suited for WDM purposes. An improved side lobe suppression and bandwidth utilization can be obtained by apodizing the refractive index modulation profile of the grating. By applying the relatively simple Gaussian apodization profile the side lobes are suppressed significantly. The bandwidth utilization of Gaussian gratings is still relatively low and other more advantageous apodizations profiles exists. An improved utilization can be achieved by applying a sinc apodizations, which theoretically can provide close to 100% utilization. Writing Bragg gratings with a sinc apodization requires a method, which is capable of introducing multiple phase shifts in the grating. So far the dithering method [2] has been the dominant method for the fabrication of such gratings. This method is highly flexible and capable of writing Bragg gratings with excellent quality. Due to the de-

mand for interferometric control of the fiber position relative to the phase mask, this method is very sensitive to vibrations and alignment of the optical setup. In this thesis the novel polarization control method for UV writing of advanced Bragg gratings is presented. This method is capable of writing Bragg gratings including multiple phase shifts by using a setup, which is easy to implement and hence attractive for industrial fabrication of advanced Bragg gratings.
With the reduced channel spacing and the increased channel bit rate the dispersion properties of the Bragg gratings also becomes important and today much effort is put into both design [3, 4] and fabrication [5, 6, 7, 8] of Bragg gratings with specific amplitude and phase response. In this thesis the focus has been directed towards the spectral properties of Bragg gratings and the their fabrication rather than on the applications of Bragg gratings. This focus manifest itself in the publications produced during the study, where only one paper is focused on an application of Bragg gratings [9]. In this conference paper Bragg gratings are used as reflectors in Distributed Feedback (DFB) fiber lasers operating above 1610 nm. Yet another application of fiber Bragg gratings is as sensor elements. Since the Bragg wavelength is influenced by several fiber properties such as temperature and stress, fiber Bragg gratings have proven to be highly sensitive, robust, and cost efficient as sensors for several applications [10].

This thesis consist of seven chapters, which are organized as follows. Chapter 2 describes the guiding properties of optical waveguides in general. In the weak guidance approximation a scalar wave equation describing the propagation of the optical mode in the optical waveguide can be deduced. The relevant parameters for the optical mode are given by relatively simple expressions as seen in this chapter. The description of the guided mode in a planar waveguide has no exact solution and either approximate or numerical methods must be applied to determine the mode profile. The Marcatili approximation was applied to a planar waveguide with core dimensions ($5.5 \times 5.5\,\mu\mathrm{m}^2$) similar to those used in the study on planar waveguides.
Chapter 3 briefly describes the photosensitivity of germanosilicate optical waveguides towards ultraviolet illumination. A number of different processes in the germanium doped core are believed to be responsible for the UV induced changes. The subject of photosensitivity is complex and the author makes no attempt to cover the whole field. This chapter hence only present a few of the models developed over the last decades. A comparison between the efficiency of two continuous-wave lasers operating at 244 nm and 266 nm is presented at the end of the chaper.
The theory of Bragg gratings is described in Chapter 4, where the coupled mode problem is introduced by considering the Bragg grating as a pertubation of the fiber. An exact solution to the coupled mode equations only exists for uniform gratings. For weak gratings a Fourier transform of the coupling coefficient determines the response from the grating. For stronger gratings this approach is no longer valid. Instead a transfer matrix method can be applied to determine the response from the grating.
The experimental setup is the topic of Chapter 5, which describes the different laser sources used throughout this study. Furthermore the optics and the

phase mask used in order to UV write Bragg gratings in optical waveguides are described.
The main effort in this study is presented in Chapter 6, which in detail describes the different aspects of the novel polarization control method for UV writing of advanced Bragg gratings. Both the principle and the apodization profiles realized by using the model are described. Then follows a description of the method specific optical components required to implement the method and the optimization and alignment of these. Finally the results obtained by using the method are presented and concluding remarks are given at the end of the chapter.
Chapter 7 summarize the effort made on planar waveguides from the fabrication in the cleanroom, the characterization of their photosensitivity to the UV writing of gratings with different apodization profiles. Due to the fabrication process the waveguides needed to be sensitized by deuterium loading, which was performed using both 100 bar and 1800 bar loading pressure. The match between the measured and simulated dual-scan written Bragg gratings indicate that the quality of the waveguides is excellent.
Finally concluding remarks and an outlook on the future applications of the polarization control method is given in Chapter 8.

Chapter 2

Germanosilicate based optical waveguides

2.1 Introduction

This chapter is dedicated to the description of the propagation of light in germanosilicate based optical waveguides. The germanium doped silica glass is by far the most used material in the production of waveguides for optical communication links due to properties described in Section 2.2. Two distinct types of optical waveguides were used in this study: the optical fiber and the planar waveguide. The modal fields of light propagating in optical fibers and planar waveguides are addressed in Sections 2.3 and 2.4, respectively.

2.2 General properties

Silica glass is an obvious choice as the basis material when fabricating telecommunication links for data transmission over long distances. The inherent low loss in the 1550 nm window enables data transmission over distances in the order of 100 km without amplification. The dominant contributions to the loss are vibrational resonances and Rayleigh scattering with its characteristic λ^{-4} dependence on the wavelength of the propagating light. Furthermore does the presence of OH^- ions in the glass introduce loss around 1370 nm. The fabrication of optical fibers is today at a level, where OH^- related loss and scattering at non-uniformities are negligible and the loss is close to the fundamental limit defined by the Rayleigh scattering. At wavelengths in the 1550 nm window this corresponds to a loss of 0.15 dB/km. Defects leading to absorption in the ultraviolet (UV) range introduce loss and fiber manufacturers attempt to eliminate them. Their presence have a fundamental significance for the UV inscription of Bragg gratings in optical waveguides though as described in Chapter 3. Methods to sensitize the waveguides towards UV light exist and Bragg gratings may also be written in optical waveguides, which initially only have negligible UV absorption.

The refractive index n of silica glass is calculated using the Sellmeyer equa-

tion [11]

$$n^2 = 1 + \sum_{i=1}^{3} \frac{A_i \lambda^2}{\lambda^2 - \lambda_i^2} \tag{2.1}$$

where A_i is the strength of the i^{th} oscillator with wavelength λ_i. Two electronic transitions and one lattice vibration are important for the calculation of the refractive index of germanosilicate glass. Since the wavelength of the electronic transitions are both shifted slightly towards 1550 nm and are stronger in germania, GeO_2, doping with germanium increase the refractive index of the glass at wavelengths in the telecommunication window. Other dopants are used to either increase or lower the refractive index, but the far most important dopant is without comparison germaium. In present day fibers for optical communication the refractive index profile in the radial direction have a complex profile using both graded index profiles and suppressed claddings. In the recent years a new type of fibers operating by photonic bandgap confinement [12] has appeared. These fibers may have several special applications in future telecommunication links, but it is most likely that the majority of the thousands of kilometers of optical fibers used in the optical networks still will rely on the principle of total internal reflection of the optical wave at the core-cladding interface.
At the nodes of an optical network signal management including e.g. amplification, add-drop multiplexing, signal broadcasting or splitting may be required. While the optical fiber is excellent in transmitting data over long distances, it is less suited for fabrication of integrated components with complex functionalities. For this purpose the silica-on-silicon planar waveguides are superior to the optical fibers. Components such as arrayed-waveguide-gratings capable of multiplexing (and de-multiplexing) up to 128 channels [13] can be fabricated on a single wafer. Producing such a device using only optical fibers would be highly impractical if not impossible. Using germanium-doped silica as core material in the planar waveguides ensures excellent coupling of light from optical fiber to planar waveguide and *vice versa*. The loss in planar waveguides is higher than in optical fibers due to both scattering at fabrication induced imperfections in the waveguide, bend losses and substrate leakage. Given the short length of the planar waveguides, the relatively high loss is not a problem.

2.2.1 Weak guidance approximation

The full mathematical description of the propagation of electromagnetic fields in optical waveguides requires a complex vector analysis. It may though be simplified if the index step between the core and cladding is small, which is the case for all optical waveguides considered in this thesis. In the so-called weak-guidance approximation [14, 15] the coupling between the vectorial components of the field is neglected. The vector wave equation can the be decoupled into scalar wave equations, one for each component of the optical field. With the z-axis aligned with the optical waveguide, solutions in the form

$$\psi(x, y, z) = \psi(x, y) \exp(-i\beta z) \tag{2.2}$$

are assumed, where β is the modal propagation constant. The scalar wave equation for e.g. the x-direction then takes the form

$$\left[\nabla_\perp^2 + k_0^2 n^2(x,y) - \beta^2\right] \psi_x(x,y) = 0 \tag{2.3}$$

where $k_0 = 2\pi/\lambda$ is the free-space wavenumber of light propagating with the wavelength λ and $\nabla_\perp$ indicate that differentiation only is performed in the plane perpendicular to the direction of propagation. The solutions to this wave equation evidently depends on the refractive index profile, $n(x,y)$, of the waveguide. The modal fields must be bounded everywhere and decay away from the waveguide core. Together with the requirement that both the modal field and its first derivatives are continuous at the core-cladding interface, this leads to an eigenvalue equation for the modal fields and their propagation constants. The following sections describe primarily the results of the mode field analysis for optical waveguides and refer to [16] and [15] for details on the analysis on optical fibers and planar waveguides respectively. Due to the different geometries of the optical fiber and the planar waveguides, the description of the modal fields in the two are presented in two individual sections 2.3 and 2.4, respectively.

2.3 Optical fiber modes

To simplify the analysis, the refractive index profile is assumed to be step-like, with core radius a and refractive indices n_{core} and n_{clad} of core and cladding respectively:

$$n(\rho,\phi) = \begin{cases} n_{\text{core}} & \text{for } \rho \le a \\ n_{\text{clad}} & \text{for } \rho > a \end{cases} \tag{2.4}$$

The cylindrical geometry of an optical fiber suggest that the calculation of the propagating modes is most conveniently performed using cylindrical coordinates, (ρ,ϕ,z), where ρ is the radial distance from the center, ϕ the azimuthal angle, and z is the position along the fiber. The scalar wave equation is then given by [17]

$$\frac{\partial^2\psi}{\partial^2\rho} + \rho^{-1}\frac{\partial\psi}{\partial\rho} + \rho^{-2}\frac{\partial^2\psi}{\partial^2\phi} + \left[k_0^2\, n^2(\rho,\phi) - \beta^2\right]\psi = 0 \tag{2.5}$$

This wave equation allows for a separation of the variables and a solution for the electric field strength may be written in the form

$$\psi = E(\rho)\, \cos(l\phi) \exp\left[i(\omega t - \beta z)\right] \tag{2.6}$$

where the $\exp(i\omega t)$ term describe the time dependence of the mode field, l is the azimuthal mode number, and $E(\rho)$ is a solution to

$$\frac{d^2E}{d\rho^2} + \rho^{-1}\frac{dE}{d\rho} + \left[k_0^2\, n^2(\rho,\phi) - \beta^2 - \frac{l^2}{\rho^2}\right] E = 0 \tag{2.7}$$

This equation is valid for all three components of the wave vector E_{x}, E_{y}, and E_{z}. The solution to this differential equation can be expressed in terms of the

Bessel functions J_l and the modified Bessel functions K_l, $l = 0, 1, 2...$. Given the constraints on the modal field amplitude mentioned above, the complexity of the solution is reduced, and the individual field components are each described by

$$E(\rho) = \begin{cases} A\,J_l(\alpha\rho) & \text{for } \rho \leq a \\ C\,K_l(\gamma\rho) & \text{for } \rho > a \end{cases} \tag{2.8}$$

where the values of A and C are determined from continuity demands, and the parameters α and γ are given by

$$\alpha^2 = n_{\text{core}}^2\,k_0^2 - \beta^2 \tag{2.9}$$

$$\gamma^2 = \beta^2 - n_{\text{clad}}^2\,k_0^2 \tag{2.10}$$

The value of the propagation constant, β, is determined by the continuity demand of the modal field and its first derivatives at the core-cladding interface, i.e. between J_l and K_l. Every mode has a unique β-value, which for a guided mode is in the range

$$n_{\text{clad}}\,k_0 < \beta < n_{\text{core}}\,k_0 \tag{2.11}$$

The fundamental mode of an optical fiber has no cut-off, and any given fiber (with a positive index step) will guide this mode. The cut-off conditions for the higher order modes are found by setting $\beta = n_{\text{clad}}\,k_0 \Rightarrow \gamma = 0$. For the lowest higher order mode, the eigenvalue equation resulting from the continuity demands then reduce to [16]

$$J_0(V) = 0 \tag{2.12}$$

where $V = k_0 a\sqrt{n_{\text{core}}^2 - n_{\text{clad}}^2}$ is the normalized frequency of the mode. From the knowledge of the Bessel functions, Equation 2.12 gives the upper limit on the V-value for single mode fibers to equal $V = 2.405$. At higher values the fiber guides also higher order modes, which rarely is a desirable situation for the system designer. Standard telecommunication fibers hence always operate below this limit.

In the weak-guidance approximation the longitudinal component of the optical fields may be neglected, and the fields are conveniently described by linearly polarized LP_{lp} modes, where l is the azimuthal mode number defined by Equation 2.6 and p the radial mode number. The fundamental mode, referred to as LP_{01}, has no azimuthal field extremes and the Gaussian mode field approximation [14] is often used when describing the transverse mode field in an optical fiber

$$E_x(\rho, z) = E_0 \exp\left(-\frac{\rho^2}{w^2}\right) \exp(i\beta z) \tag{2.13}$$

where E_0 is the field amplitude and w is the $1/e$ radius of the modal field also referred to as the spot size. The latter can be calculated using variational arguments to a precision better than 1%. The result show that w is linearly related to the core-radius, a, through

$$w = a\,(0.65 + 1.619\,V^{-3/2} + 2.879\,V^{-6}) \tag{2.14}$$

The optical modes are rarely completely confined to the core but penetrates into the cladding. This has evidently some implications when for instance a Bragg grating is written in the fiber core. Even with a strong index modulation the grating may still be only weakly reflecting if a large proportion of the mode propagate in the cladding. The number quantifying the proportion of the optical power, which propagate in the fiber core is the confinement factor η. In the Gaussian approximation of the mode profile the confinement factor is given by

$$\eta = \frac{\int_0^a \exp(-\rho^2/w^2)\, 2\pi\rho d\rho}{\int_0^\infty \exp(-\rho^2/w^2)\, 2\pi\rho d\rho} = 1 - \exp(-2a^2/w^2) \tag{2.15}$$

In standard fibers for optical communication systems the confinement factor is in the order of 0.7 to 0.8 and the spot size is approximately 10% larger than the core radius. The final expression needed for the calculation of the fiber parameters is the normalized propagation constant, b, which is given by the approximate expression

$$b(V) \approx (1.1428 - 0.9960/V)^2 \tag{2.16}$$

This parameter links the refractive indices of the core and cladding to the effective refractive index of the mode through

$$n_{\text{eff}} = n_{\text{clad}} + b(n_{\text{core}} - n_{\text{clad}}) \tag{2.17}$$

2.3.1 Optical fiber parameters

Several optical fibers were used during this study. The knowledge of fiber parameters such as the confinement factor, η, is important in the characterization of the changes in the refractive index during exposure to ultraviolet light. An example of a calculation of the relevant parameters for a standard fiber is presented below. The calculation itself is similar for every type of fiber and a table listing the confinement factors of the different fibers used throughout this study is presented at the end of this section.

Confinement factor calculation

The calculation assumes a step index profile, using a core radius of $a = 4.15\,\mu$m, and refractive indices of core, $n_{\text{core}} = 1.4513$, and cladding, $n_{\text{clad}} = 1.4444$. The numerical aperture, $N.A.$, of the fiber is given by

$$N.A. = n_{\text{core}}\sqrt{2\Delta} = 0.142 \tag{2.18}$$

where $\Delta = 4.75 \times 10^{-3}$ is the fractional index step at the core-cladding interface. For small index steps, the normalized mode frequency, V, can be expressed through the numerical aperture

$$V = \frac{2\pi a}{\lambda} N.A. \tag{2.19}$$

The λ occurring in this expression should equal the Bragg wavelength of the grating, since this is the relevant wavelength for the calculation of the confinement factor, when this subsequently is used to determine the UV induced refractive index modulation amplitude. We used the same wavelength, $\lambda = \lambda_{\text{Bragg, F}\to 0}$, to calculate the modulation amplitude for the whole growth curve. The error introduced by this simplification is $\Delta n_{\text{eff}}/n_{\text{eff}}$, which usually is below 0.1%. By extrapolating the measured growth curve to $F = 0\text{J/cm}^2$, we found that $\lambda_{\text{Bragg, F}\to 0} = 1548.78\,\text{nm}$. The normalized mode frequency then equals $V = 2.40$, which is close to the cut-off condition of the second mode in the fiber. This is a normal design approach used in order to ensure the highest possible guidance in the core, while still operating in single mode. With the values of a and V in hand, Equation 2.14 is used to find the spot size, $w = 4.65\,\mu\text{m}$. Calculating the confinement factor is then straight forward using Equation 2.15 and a value of 0.81 is found. The normalized propagation constant constant, $b = 0.53$, is calculated using the expression given in Equation 2.17.

It should be noticed that illumination by ultraviolet light changes the refractive index of the germanium doped fiber core and hence the confinement factor of the guided mode. An increase of 5×10^{-4} in the refractive index of the core of a standard telecommunication fiber results in less that 2 % decrease of the spot size. The corresponding increase in the confinement factor is in the order of 1.4 %, neglecting UV induced compaction of the core.
Deuterium loading increases the refractive index of optical waveguides [18]. An analysis using values for the core and cladding indices in a deuterium-free fiber combined with the extrapolated Bragg wavelength of the loaded fiber does not give an exact description of the modal field. The deviations are negligible though, and confinement factors of the optical waveguides were calculated using this approach.
It is possible to calculate the refractive indices of core and cladding if information about the core radius and spot size are available [19]. The uncertainty in the data is a few percent due to the approximate nature of the expressions for V and b.
The calculated confinement factors for the optical fibers used throughout this study are listed in Table 2.1. The two commercial available MatchedClad and TrueWave fibers have 81 % and 70 % of the guided mode confined to the core, respectively, while the HNLF fiber have a poor confinement of the mode with only 50 % of the light propagating in the core.

	MatchedClad	TrueWave	HNLF
η	0.81	0.70	0.50

Table 2.1: The confinement factors, η, for the fibers used in this thesis. All fibers were supplied by Lucent Technologies Denmark.

2.4 Planar waveguides

This section describes the modal fields of step index rectangular waveguides with dimensions ρ_{x} and ρ_{y}. The refractive index of the waveguide core and cladding are n_{core} and n_{clad}. The geometry of the planar waveguides makes the cartesian coordinate system the most convenient choice when describing the mode fields of the propagating light waves. The light is guided by the principle of total internal reflection along the z-axis with the field slightly penetrating into the cladding very similar to the situation in optical fibers. The mathematical description is more complicated though due to the reduced symmetry of the waveguide core. No exact analytical solution exits for the modal field in a square or rectangular waveguides and either numerical or approximate methods must be applied. The following describes briefly the Marcatili method [15], which is one of the approximate methods. The weak-guidance approximation is still valid and the scalar wave equation seen in Equation 2.3 describing the decoupled transverse components of the optical field can be used. In the Marcatili approximation the two-dimensional problem describing the transverse mode field is decoupled into two one-dimensional problems, which then can be solved independently. The mode field is assumed to have the following distribution

$$\psi(x,y) = A\cos(U_x X)\cos(U_y Y) \tag{2.20}$$

where U_x and U_y are determined by the eigenvalue problems defined by boundary conditions similar to those used in the analysis of the optical fiber. X and Y are the normalized positions $X = x/\rho_x$ and $Y = y/\rho_y$. The mode profile for a planar waveguide with a $5.5 \times 5.5\,\mu\mathrm{m}^2$ core calculated using the Marcatili method is presented in Figure 2.1. The accuracy of the description is improved by introducing an effective refractive index. One of the one-dimensional wave equations of the Marcatili approximation is solved and the resulting propagation constant, β_i, is used to determine an effective refractive index

$$n_i^{\mathrm{eff}} = \beta_i/k_0, \qquad i = x \text{ or } y \tag{2.21}$$

where k_0 is the free-space wavenumber. This effective refractive index is then used to construct an eigenvalue problem for the other transverse direction.
Commercial software calculating the modal fields in a given planar waveguide is available. The program Selene by Kymata [20], has been used to evaluate the confinement factor, η, and modal fields of the planar waveguides fabricated in this study.
In planar waveguides the propagation constants β_x and β_y often differ noticeably making the waveguides birefringent. Optical fibers also show some degree of birefringence but with a significantly smaller magnitude. This is due to the cylindrical geometry of the optical fiber, which has no preferential axis in the transverse plane. In the planar waveguides the presence of the substrate and the rectangular shape of the waveguide core introduces such an axis. The different thermal expansion coefficients of the substrate and the silica glass results in a stress related contribution to the birefringence. In a rectangular waveguide the solutions to the wave equations and hence the derived propagation constants

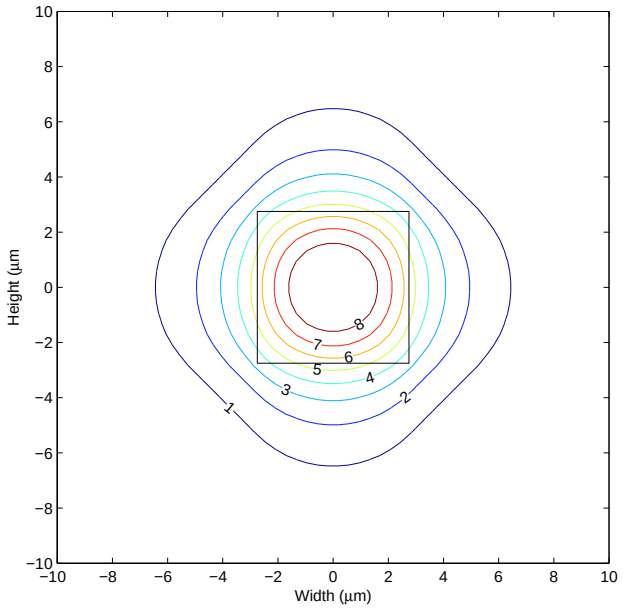

Figure 2.1: Profile for the guided mode of a planar waveguide with $5.5 \times 5.5\,\mu\mathrm{m}^2$ core and index step of $n_{\mathrm{core}} - n_{\mathrm{clad}} = 0.007$. The square symmetry of the core clearly manifests itself in the mode profile (courtesy R. Shim).

are different. Any deviations from the ideal square geometry of the core will evidently also result in birefringence. In the planar waveguides produced in this study, the birefringence corresponds to a difference of 3×10^{-4} between the effective refractive indices for the two transverse directions.

Chapter 3

Photosensitivity in germanosilicate waveguides

3.1 Introduction

Fabrication of high quality Bragg gratings with predictable spectral response requires a detailed knowledge of the relation between the accumulated UV fluence and the induced change in the refractive index. The complex nature of the amorphous silica glass used in the majority of optical waveguides makes a detailed description of the glass matrix complicated. Germanium doping increases the complexity and today no single model explains all the observations made during UV exposure and subsequent thermal annealing. The large variety of models may be divided into microscopic [21, 22] and macroscopic [23] models. While the latter describes the changes in the refractive index as a result of compaction of the core material, the former links the UV induced changes to electronic transitions on the microscopic scale. The compaction model is supported by Atomic Force Microscope studies [24, 25] and axial stress measurements [26], while electron spin resonance measurements correlates the changes in the refractive index to the concentration of point defects [27] thus supporting the microscopic models. It should be emphasized that the microscopic and macroscopic processes are likely to be at play simultaneously and that one approach does not exclude the other. Several microscopic transitions will hence cause rearrangement of the glass matrix on a macroscopic scale. While the macroscopic models quantify the index change through the measured volume change, the microscopic models assume that the creation of defects such as GeE' centers upon UV exposure [28, 27, 29] change the refractive index through the Kramers-Kronig relation [11, 10]

$$\Delta n(\lambda) = \frac{1}{(2\pi)^2} \int_0^\infty \frac{\Delta\alpha(\lambda')d\lambda'}{1-(\lambda'/\lambda)^2} \tag{3.1}$$

where $\Delta\alpha(\lambda)$ is the UV induced change in absorption and λ is the wavelength. There is a general agreement that three "types" of photosensitivity exists [11, 10]. The term "Type I" photosensitivity is used to describe the UV induced changes when the effective refractive index and the refractive index modula-

tion have a monotonous growth during UV illumination. Type II describes the changes occurring at very high laser irradiance, typically above 700 mJ/cm^2 [30]. In this regime physical damage in the fiber core is responsible for large refractive index changes and Bragg gratings can by written by a single pulse. In hydrogen-free high germanium content fibers a third photosensitivity type, Type IIA, starts to dominate when the Type I growth saturate. In this regime, the refractive index modulation decrease and a grating with negative Δn appears. All exposures performed in this study were of Type I. It should be noted, that this chapter does not give a comprehensive coverage of the photosensitivity of optical waveguides, but is merely thought as a brief introduction to the defects and processes, which are believed to be responsible for the changes in the refractive index upon UV exposure. Since a detailed understanding of silica glass is out of the scope of this study the author refers to Scholze [31] for further reading on general glass properties and Othonos & Kalli [10] for a thorough summary of the defects present in germanium doped silica glass.
This chapter is organized as follows, Section 3.2 describes the structure and defects of germanium doped silica glass, Section 3.3 looks at the photosensitization by hydrogen loading, while Section 3.4 briefly comments on the microscopic and macroscopic models explaining the interaction between the glass and the UV radiation. Section 3.5 presents an investigation of the wavelength dependence of the photosensitivity before finally a short summary is given in Section 3.6.

3.2 Point defects in germanosilicate glass

Silica glass is a frozen-in undercooled liquid [31] and shows accordingly no higher order symmetry. The majority of the silicon atoms are bound to four oxygen atoms in slightly perturbed tetrahedral structures, where the oxygen atoms bridge two neighboring silicon atoms. The interconnected ring structures thereby created have a wide size distribution and together with the large variety of defects found in the glass this makes a detailed description of the silica matrix a complex subject. Since the germanium atom has the same number of valence electrons it can take the place of a silicon atom without disrupting the geometry of the glass matrix. When germanium doped silica glass is deposited under oxygen deficient conditions a large variety of defects are formed in the glass matrix. Both microscopic and macroscopic models rely on these defects to absorb UV light in the range around 242 nm since pure silica only has a negligible absorption at wavelengths down to 180 nm. Several absorption bands in the UV range have been reported in Ge-doped silica. Strong singlet-singlet transitions at 180 nm and 242 nm and a weaker singlet-triplet transition at 325 nm are all attributed to germanium related defect centers [32, 28, 33]. Some of the defects believed to be important for the UV induced processes, are depicted in Figure 3.1. Several authors [28, 34] assume that the breaking of a Ge-Ge or Ge-Si wrong bond through absorption of a UV-photon is responsible for the creation of a GeE' center as depicted in Figure 3.2. The reverse process is accelerated when thermal energy is supplied thereby erasing the UV induced change in the refractive index. The return to the original defect allows for the

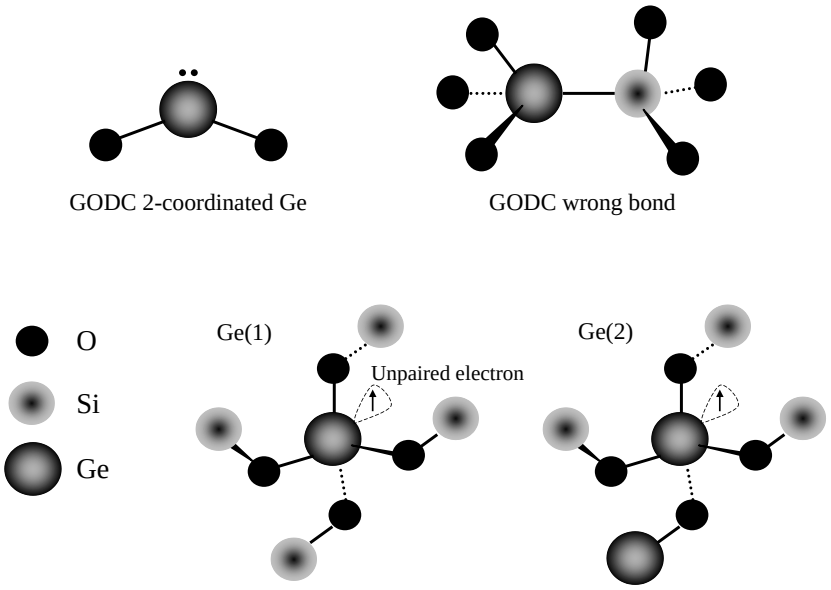

Figure 3.1: Four of the germanium oxygen deficient center defects found in germanium-doped silica glass deposited under oxygen deficient conditions. After [10]

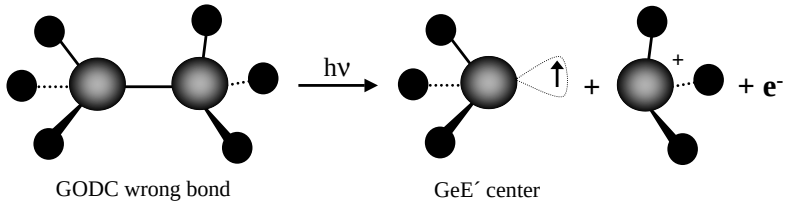

Figure 3.2: The UV induced excitation of a Ge-Ge wrong bond in a neutral oxygen monovacancy (NOV) thereby creating a GeE' defect.

thermal cycling of the process as reported in [35]. Nishii *et al.* [34] suggested an additional two-photon process generating electron trapped centers, which upon further exposure were concerted to GeE' centers.

3.3 Deuterium sensitization

Sensitization by hydrogen loading is known to increase the photosensitivity in germanosilicate waveguides [36]. The wavelength dependence and the dynamics of the UV induced growth of the refractive index in sensitized waveguides differs significantly from that of a non-sensitized waveguide [29]. Furthermore has the Type IIA growth found in high germanium content hydrogen-free waveguides never been reported in hydrogen loaded samples. The function of the hydrogen molecules is believed to be either photochemical [27, 29] or as a resonant energy state speeding up the annihilation of an index reducing defect [22]. The hydrogen isotope deuterium (D) gives a similar increase in the photosensitivity, with the advantage that the Si-OD band have a lower resonance frequency than Si-OH, thus moving the induced loss out of the telecommunication window. All sensitized fibers and planar waveguides used throughout this thesis were loaded with deuterium only.

At temperatures well below 100 °C the deuterium molecules diffuse into the optical waveguide without reacting with the glass. The diffusion coefficient, D_{D_2}, is given by [37]

$$D_{D_2} = 2.28 \times 10^{-4} \cdot \exp\left(\frac{-40.19\,\mathrm{kJ/mole}}{RT}\right) \mathrm{cm}^2/\mathrm{s} \tag{3.2}$$

where $R = 8.31\ \frac{\mathrm{J}}{\mathrm{K \cdot mole}}$ is the gas constant and T is the absolute temperature. The in-diffusion of the deuterium molecules can thus be speeded up by raising the temperature, but this is at the expense of a reduced equilibrium concentration, c_{eq}, in the waveguide. At room temperature c_{eq} is related to the gas pressure in the loading chamber through [38]

$$c_{eq} = 116\,\mathrm{ppm/bar} \tag{3.3}$$

where 1 ppm is defined as 10^{-6} moles of deuterium per mole of SiO_2. In an optical waveguide loaded at 130 bars the equilibrium concentration thus equals $c_{eq} = 1.5\mathrm{mole\%\ D_2}$. This relatively low concentration is sufficient in order to increase the photosensitivity of the optical waveguide significantly. Optical waveguides that are insensitive towards UV exposure without sensitization can become UV sensitive when loaded with deuterium. A good example of this are the planar waveguides presented in Chapter 7, which are oxygen annealed during fabrication. This effectively removes the oxygen deficient centers thus making these waveguides highly insensitive without loading. In the high germanium content waveguides that are UV sensitive already prior to deuterium loading, the induced change in the refractive index is increased by an order of magnitude by loading with $c_{eq} = 1.5\mathrm{mole\%\ D_2}$.
Deuterium loading was performed by placing the waveguides under 100−2000 bars at room temperature in custom made pressure chambers.

3.4 Photosensitivity models

A large number of models have been applied to explain the UV induced changes in germanium doped silica glass upon UV exposure. It is out of the scope of this study to describe all the models in detail and the author refers to [10, 11] for more detailed descriptions. Instead, this section focuses on the UV dipole-quadrupole model [22], the color-center model [21], and the compaction model [23] and gives a brief introduction to the physics behind these.

3.4.1 UV dipole-quadropole model

The UV dipole-quadrupole model assumes that a germanium related oxygen defect center (GODC) acts as a gate for energy transfer from the UV beam to the glass matrix through a non-radiative dipole-quadropole interaction. During initial UV exposure a defect, D_1, is formed in the glass matrix in close vicinity to the GODC. The absorption line of this defect is situated at higher wavelengths than the original site and the refractive index is increased as described by the Kramers-Kronig relation. The energy levels of the GODC and the defect site are depicted in Figure 3.3. The physics behind the creation of D_1 is as follows. A photon excites a GODC from its ground state, $^1S_0$, to the excited state $^1S_1$. By a dipole-quadropole transition the energy is transferred to a nearby site in the silica matrix, thereby generating an excited defect state D_1^*. From D_1^* there is a non-radiative decay with a significant structural rearrangement leading to the lowest energy level of the defect D_1. Structural rearrangement is required for a matrix site in the defect ground state D_1 to return to the original matrix site ground state thus giving D_1 almost infinite lifetime at absolute zero temperature. When the defect has been thermally excited to D_1^*, which resembles the glass matrix ground state geometry, a quadropole-quadropole transition transfers the energy to the GODC and the matrix site returns to its original geometry and the change in refractive index is annihilated.

A second metastable defect state D_2 is generated with continued UV exposure. This state is believed to lower the refractive index of the glass due to a very small overlap integral in the Kramers-Kronig calculation. D_2 may be the result of further rearrangement of the D_1 defect, which would explain that the negative change in the refractive index always is preceded by a positive index change. The D_2 defect may absorb another UV photon and be excited into the bandgap. The matrix site then returns to the original matrix geometry and the index reducing agent is annihilated. This process is speeded up by the presence of hydrogen molecules since their singlet-triplet transition coincides with the energy of D_2 plus 5.12eV. As a consequence hydrogen will catalyze the elimination of the index reducing defect.

The UV induced change in the refractive index is calculated by integrating over the molar germanium volume making the assumption that the germanium

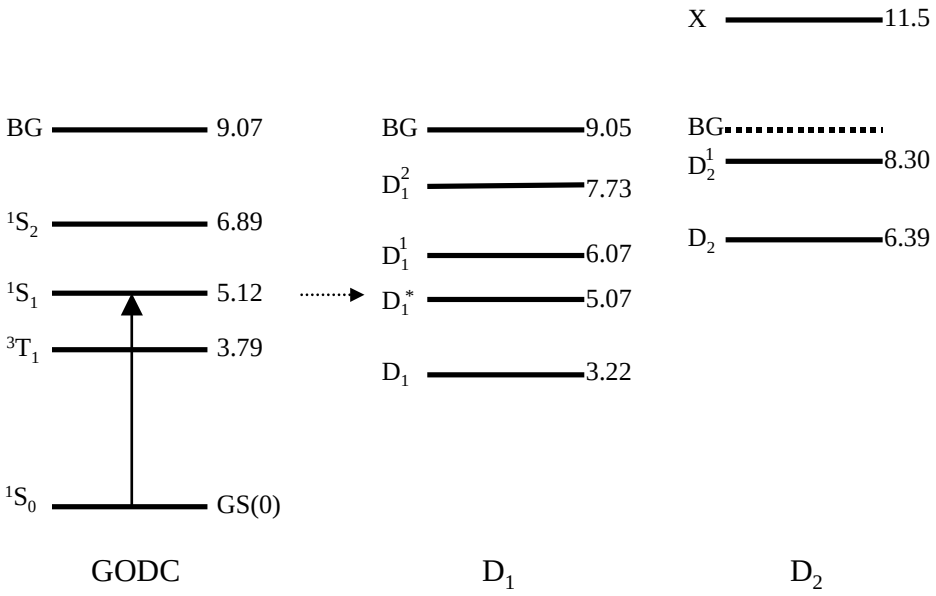

Figure 3.3: Energy levels in the GODC and silica matrix site, where the defects D_1 and D_2 are created. The dotted horizontal line indicates the non-radiative dipole-quadropole transition responsible for the energy transfer from the GODC to the silica matrix. All energies indicated at the right hand side of the energy levels are given in electron volts (eV) relative to the ground state. Adapted from [22]

atoms are distributed with uniform inter-atomic distance:

$$\Delta n \propto \int_0^{r_{max}} \{\Delta n_1 [D_1](r) + \Delta n_2 [D_2](r)\} \rho(r) r^2 dr \tag{3.4}$$

where $r_{\max}$ is the radius of the GODC "unit-cell", $\rho(r)$ the radial density function of germanium atoms, Δn_i the index change per unit volume of the respective defects D_i and $[D_i](r)$ their radial concentration distributions.

A strong argument in favor of the dipole-quadropole model is the description of the erasure of the UV-induced refractive index changes during thermal annealing. Erdogan *et al.* [39] linked the thermally induced decay of the generated defects to an approximately 2 eV wide defect energy level distribution. It may seem physically unreasonable to have such a wide energy distribution with a center energy of 2 eV, even when taking into account the amorphous structure of silica. The dipole-quadropole model on the other hand assumes only two discrete energies to describe the thermal annealing using instead a distribution of the distance r from the defect to the nearest GODC. Thermal annealing of the index raising defect D_1 is described by

$$\frac{d[D_1]}{dt} = -k_{D_1} \left(\frac{r_1}{r}\right)^{10} \exp\left(-\frac{\Delta E_{D_1}}{RT}\right) [D_1] \tag{3.5}$$

where $[D_1]$ is the D_1 defect concentration, k_{D_1} the thermal trial rate, r_1 the distance to the nearest neighbor, ΔE_{D_1} is the thermal activation energy, R the gas constant, and T the absolute temperature. This equation indicates that annealing of the fiber after Bragg grating inscription will erase a number of the generated defects, starting with those closest to the GODC. The remaining defects are then very stable due to the r^{-10} dependence of the decay rather than due to their higher activation energy as assumed by Erdogan *et al.* [39].

3.4.2 Color-center model

Electron spin resonance (ESR) spectroscopy on glass prior to and after UV exposure shows that the induced change in the refractive index is strongly correlated to the creation of GeE' defects [27]. Nishii *et al.* [34] found bleaching of the 242 nm absorption band during the UV illumination accompanied by the growth of a strong absorption centered at 195 nm and a weaker peak at 256 nm. Hosono *et al.* [40] assigned the 195 nm line to the GeE' center, while the bleached band was linked to the Ge-Ge wrong bond [28, 34]. The change in refractive index during UV exposure is quantified by [41]

$$\Delta n = (2.34\Delta\alpha_{242} + 4.96\Delta\alpha_{195} + 5.62\Delta\alpha_{256}) \times 10^{-7} \tag{3.6}$$

where $\Delta\alpha_i$ is the change in the absorption at wavelength i. For a wide range of exposure times, the ratio $\Delta\alpha_{195}/\Delta\alpha_{242} \approx -2$ [41] indicating that the two bands are correlated. The photochemical process depicted in Figure 3.2 is hence a strong candidate for the primary source of the UV induced refractive index change.

The presence of hydrogen molecules in close vicinity to a germanium atom leads to an additional index raising species, GeH, whose contribution to the refractive index per unit concentration is 80 % of the GeE' center contribution per unit volume [27]. Grubsky *et al.* [29] proposed a pathway for the photochemical reaction of hydrogen with the glass, where a normal Ge-O bond exited by the UV light reacts with hydrogen to form SiOH, a GeE' center and atomic hydrogen.

3.4.3 Compaction model

Thermal annealing experiments on UV exposed fibers by Tsai *et al.* [27] showed a contribution to the refractive index, which was not correlated with the concentration of GeE' centers. Early studies by Fiori and Devine [42] indicated that germanosilicate glass densify when illuminated by UV light. Later on Bernardin and Lawandy [23] proposed that UV induced collapse of higher order ring structures in the glass matrix lead to the observed changes in the refractive index. A number of papers have subsequently supported the observation that the changes in the refractive index is correlated with a compaction of the core material [24, 26]. Fonjallaz *et al.* [26] measured the increase in the axial stress in an optical fiber during UV exposure and found that it was correlated with the induced change in the refractive index. Below a certain limit the compaction reported by Fiori and Devine [42] was reversible and thermal annealing returned the thin silica film to its original thickness. Subsequent exposure resulted in practically the same compaction as obtained in the virgin exposure. This duplicates the behavior of the refractive index under thermal cycling, thus supporting the compaction model.

3.5 Wavelength dependence

Given the width of the 242 nm absorption peak in germanium doped silica glass [43, 28] it is evident that UV exposure using a relatively wide range of wavelengths around 242 nm can induce changes in the refractive index. Using hydrogen sensitized fibers the useful wavelength range is expanded even further [29]. High power lasers operating at 257 nm [44] and 266 nm [45] have shown to be useful for Bragg grating inscription. In this study a comparison between the efficiency of a diode-pumped all-solid-state (DPSS) laser operating cw at 266 nm and a frequency doubled argon-ion (FDA) laser laser operating cw at 244 nm [46] was made. The output beam from our seven years old FDA laser was of an unusually poor quality and spatial filtering was required in order to obtain a Gaussian beam profile thus lowering the power at the sample to 15 mW. The DPSS laser beam profile was used without spatial filtering giving a power of 120 mW on the fiber. The beam size was inspected visually by a microscope viewing the blue luminescence from a wafer with germanium doped core layer. This method introduces some uncertainty in beam size and hence beam intensity at the fiber. This error may be eliminated by scanning the beam across a fiber while monitoring the blue luminescence from the fiber using an optical spectrum analyzer [47]. Due to limited beam time this procedure was

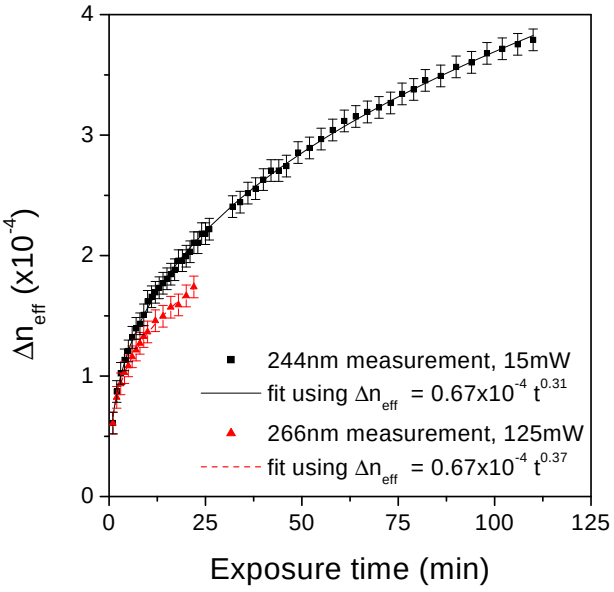

Figure 3.4: Change in the effective refractive index versus exposure time in a non-sensitized HNLF fiber using 15 mW 244 nm and 120 mW 266 nm cw light.

not performed, and the numbers given in this section are attached with some uncertainty. Transmission spectra were measured during grating growth using an ASE source and an optical spectrum analyser with a resolution of 0.01 nm. Both deuterium-free and deuterium loaded fibers were used. The photosensitivity of the fibers was in general lower when illuminated by 266 nm light compared to the 244 nm light as expected from the absorption spectra.
Growth curves[1] showing the change in the effective refractive index versus exposure time in the deuterium-free high germanium content HNLF fiber are displayed in Figure 3.4. These curves show qualitatively identical growth dynamics when using the two wavelengths. Identical beam intensities should be used in order to obtain a correct description of the wavelength dependence of the photosensitivity. To compensate for the 1:8 ratio between the intensity of the 244 nm and 266 nm beams, the measured refractive index change at 244 nm was scaled by a factor $8^{0.5} = 2.828$ assuming that the dependence of the photosensitivity on the intensity, I, is given by $I^{0.5}$ [48]. The change in the effective refractive index is fitted well by a power law [48] for both wavelengths:

$$244\,\text{nm} : \Delta n_{\text{eff}} = 1.90 \times 10^{-4}\, t^{0.37} \tag{3.7}$$

$$266\,\text{nm} : \Delta n_{\text{eff}} = 0.67 \times 10^{-4}\, t^{0.31} \tag{3.8}$$

where a compensation for the difference in beam intensity has been made. The photosensitivity is thus approximately 3-4 times higher when using 244 nm light. The 8 times higher intensity of the 266 nm beam cannot compensate for the reduced absorption due to the $I^{0.5}$ dependence of the photosensitivity and the

[1]The measurement errors on the growth curves presented in this thesis are discussed in Appendix A.

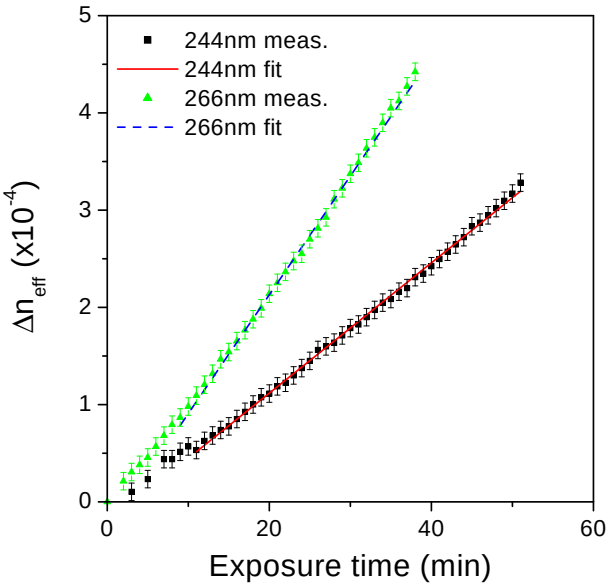

Figure 3.5: Change in effective refractive index versus exposure time in a deuterium loaded MC fiber using 15 mW 244 nm and 120 mW 266 nm light

fastest grating growth in the deuterium-free HNLF fiber was obtained when using the 15 mW 244 nm beam.

The growth of Bragg gratings in deuterium loaded fibers was also investigated with focus on the commercially available MatchedClad (MC) and TrueWave (TW) fibers both loaded at a pressure of 135 bar. A general characteristic of the photosensitivity of the deuterium loaded low to medium germanium concentration fibers used in this study is displayed in Figure 3.5, which shows the change in the effective refractive index versus time for a deuterium loaded MC-fiber. After an exposure time of approximately 10 minutes, the growth in the refractive index is a linear function of the exposure time. This behavior was also observed in planar waveguides as described in Section 7.2. In both sensitized fibers the fastest grating growth was found when using the 120 mW 266 nm beam. The 8 times higher intensity compared to the 244 nm beam evidently compensates for the lower absorption at the larger wavelength. This can be explained by assuming a linear relation between the change in the refractive index and the beam intensity $\Delta n \propto I$. By scaling the photosensitivity curve for the 244 nm light linearly with the beam intensity to 120 mW, the ratio between the induced changes in the refractive index at a given exposure time is now 5:1 in favor of the 244 nm light.

The change in the refractive index modulation amplitude was calculated from the transmission dip using the formula for a uniform grating (Equation 4.23) taking into account the Gaussian shape of the grating by defining an effective length $L_{\text{eff}} = sL$, where s is the taper parameter of the Gaussian beam profile described in Section 4.4.2. This approach was supported by simulations of individual gratings measured during the grating growth. The index modulation

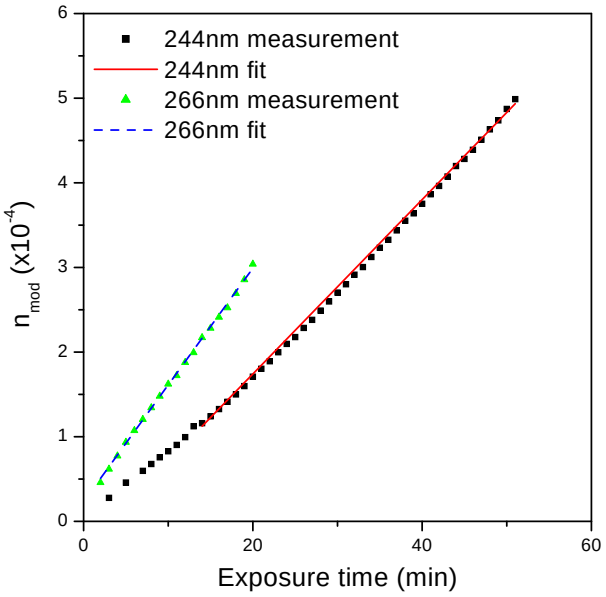

Figure 3.6: Change in the refractive index modulation versus exposure time in a deuterium loaded MC fiber using 15 mW 244 nm and 120 mW 266 nm light

versus exposure time is depicted in Figure 3.6. The qualitatively behavior of the effective refractive index and the refractive index modulation during exposure with the two wavelengths is similar. This indicates that the induced changes when using the two wavelengths are chemically similar and the major difference is the reduced absorption when using the long wavelength UV light.

3.6 Summary

There exist several models explaining the photosensitivity of germanosilicate optical waveguides each describing with success some of the observations made during UV exposure. The diversity of these models indicates that a number of processes are at play. Both microscopic and macroscopic models are used, but today no unified theory exists in spite of the large effort made in the last 20 years. The photosensitivity of germanosilicate optical waveguides has been linked to the presence of germanium related defects capable of absorbing the ultraviolet light. Attention has especially focused on the Neutral Oxygen Vacancy, where an oxygen atom is missing and two germanium atoms are directly bonded. The breaking of this so-called wrong bond results in the creation of a GeE' center. This defect has a strong absorption at 195 nm thereby increasing the refractive index through the Kramers-Kronig relation. Densification of the core material upon UV illumination has also been convincingly linked to a change in the refractive index. Whether this compaction of the core material or the creation of a strong absorption band is the dominating effect depends on the characteristics of the optical waveguide i.e. germanium concentration, hydrogen sensitization and sample history. In conclusion it is thus very likely

that the change in the refractive index during exposure to ultraviolet light is due to the influence of several mechanisms.
Sensitization by deuterium loading facilitates a significant increase in the photosensitivity of germanosilicate optical waveguides with a linear dependence on the accumulated fluence thus making this method very desirable for Bragg grating inscription.
The wavelength dependence on the photosensitivity was investigated using two continuous-wave lasers operating at 244 nm and 266 nm, respectively. The results indicate that when fabricating Bragg gratings in deuterium loaded waveguides, high power lasers operating at wavelengths slightly off the optimum 242 nm are an attractive alternative to frequency Doubled Argon-ion lasers. In non-sensitized waveguides the photosensitivity is significantly higher at 244 nm thus making the frequency Doubled Argon-ion laser the preferable choice.

Chapter 4

Bragg grating theory

4.1 Introduction

The Bragg gratings studied in this thesis consist of a periodic modulation in the refractive index of an optical waveguide core with a periodicity Λ_{mod}. A schematic presentation of a fiber Bragg grating is seen in Figure 4.1, where the wavelength dependent reflection and transmission also are illustrated. Each plane in the grating reflects the incident beam weakly. When the reflected beams from the individual grating planes add constructively there is a significant reflection from the grating. This occurs when half the wavelength of the incident beam equals the optical distance between the grating planes: $\lambda/2 = n_{\text{eff}} \cdot \Lambda_{\text{mod}}$, where n_{eff} is the effective refractive index of the propagating mode. This can be rearranged to give the first order Bragg condition

$$\lambda_{\text{B}} = 2\, n_{\text{eff}} \Lambda_{\text{mod}} \tag{4.1}$$

where λ_{B} is the Bragg wavelength of the grating. The Bragg condition can also be derived from energy and momentum conversation considerations, which shows that the wavevectors of the incident ($\mathbf{k}_{\text{i}}$) and reflected ($\mathbf{k}_{\text{r}}$) beams are related through

$$\mathbf{k}_{\text{i}} + \mathbf{K} = \mathbf{k}_{\text{r}} \tag{4.2}$$

where the grating wavevector, $\mathbf{K}$, depends on the modulation period through $|\mathbf{K}| = 2\pi/\Lambda_{\text{mod}}$. The magnitude of the beam wavevectors is inversely proportional to the signal wavelength, $|\mathbf{k}_{\text{i,r}}| = 2\pi n_{\text{eff}}/\lambda$. The Bragg condition is then derived by simple insertion in Equation 4.2.

Due to the finite length of the modulation profile, the amplitude response from a Bragg grating spread over a relatively wide spectral range. Understanding the interaction between the electric field of an optical pulse and the refractive index modulation profile of a Bragg grating is essential in order to analyze and design Bragg gratings with specific amplitude and phase responses. The most widely used method for the analysis of the scattering of an incident optical field on a Bragg grating is the coupled-mode theory described in Section 4.2. This method assumes that the grating can be considered a pertubation of the optical waveguide. The co- and counter-propagating fields in a grating are then described by

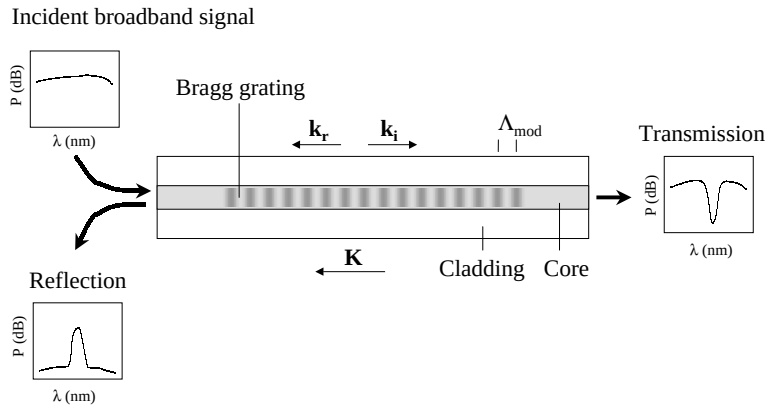

Figure 4.1: Schematic presentation of a Bragg grating with modulation periodicity Λ_{mod}. The wavelength dependence of the reflection is illustrated by the inserted incident, transmitted and reflected spectra.

a superposition of the unperturbed modes of the optical waveguide. For a grating with a uniform refractive index modulation profile an analytical solution exist to the coupled differential equations defined by the coupled-mode theory as described in Section 4.3.1. The strong side lobes encountered in uniform gratings are detrimental for the application of these gratings in Wavelength Division Multiplexing (WDM) systems. With the channel spacing of 50 GHz used in dense WDM systems a significant reflection occurs at neighboring channels thus inducing cross-talk in the communication system. An effective suppression of side lobes can be obtained by apodizing the refractive index modulation profile as seen in Section 4.4. When used in optical communication systems the phase properties of the Bragg grating become important. These are briefly introduced in Section 4.5. Strong low-dispersion gratings with almost square-like reflection peaks may be designed using inverse scattering technique as described in Section 4.6. A special class of Bragg gratings well suited for WDM systems are realized by sampling the grating with a period of hundreds of micrometers. The amplitude response from such a sampled grating shows multiple reflection peaks with the shape of the individual reflection peaks determined by the overall apodization profile as described in Section 4.7.

In optical waveguides with a photosensitive core the interference pattern observed below a phase mask during UV exposure is transferred to a modulation pattern in the refractive index of the waveguide core. Assuming that the UV induced refractive index change is uniform over the cross-section of the waveguide core the refractive index modulation can be written as

$$\delta n_{\mathrm{core}}(z) = \overline{\delta n}_{\mathrm{core}}(z) + n_{\mathrm{mod}}(z) \cdot \cos\left(\frac{2\pi}{\Lambda_{\mathrm{mod}}} z + \varphi(z)\right) \tag{4.3}$$

where $\overline{\delta n}_{\text{core}}(z)$ is the induced change in the local average refractive index of the core. Λ_{mod} and $n_{\text{mod}}(z)$ are the period and amplitude of the modulation profile, respectively. A chirp in the grating is incorporated through $\varphi(z)$, which is constant in chirp-free gratings. Following the analysis by Erdogan [49], Section 4.2 describes only gratings, where the index modulation amplitude is linked to the average refractive index through $n_{\text{mod}}(z) = s \cdot \overline{\delta n}_{\text{core}}(z)$, with s being the fringe visibility of the index modulation profile. The modulation profile can then be written as

$$\delta n_{\text{core}}(z) = \overline{\delta n}_{\text{core}}(z) \left[1 + s \cdot \cos\left(\frac{2\pi}{\Lambda_{\text{mod}}} z + \varphi(z)\right)\right] \tag{4.4}$$

The analysis of gratings with independent average refractive index and refractive index modulation amplitude is presented in Section 4.4.

In this chapter the effective refractive index of the propagating mode in an optical waveguide prior to Bragg grating inscription is referred to as n_{eff}. With UV exposure it grows[1] to a value of $n_{\text{eff}}^{\text{UV}} = n_{\text{eff}} + \overline{\delta n}_{\text{eff}}$. When the UV induced index changes are addressed elsewhere in this thesis, the simplified writing n_{eff} is used instead of $n_{\text{eff}}^{\text{UV}}$.

The results presented in this chapter are well-established and detailed descriptions has been published by several authors [49, 11, 10] prior to this thesis. The chapter is still included though in order to produce a complete description of the subject covered by this thesis.

4.2 Coupled-mode theory

The coupled-mode theory [50] was originally developed for the analysis of uniform gratings only. With the work of Kogelnik [51] the model was extended to cover also gratings with nonunifrom profiles. It assumes that the transverse component of the electric fields propagating in an optical waveguide in which a Bragg grating is present may be expressed by a superposition of the transverse mode fields, $\mathbf{e}_m^{\text{T}}(x, y)$, of the unperturbed waveguide

$$\mathbf{E}^{\text{T}}(x, y, z, t) = \sum_m \left[A_m(z) \exp(i\beta_m z) + B_m(z) \exp(-i\beta_m z)\right] \mathbf{e}_m^{\text{T}}(x, y) \exp(-i\omega t) \tag{4.5}$$

where $A_m(z)$ and $B_m(z)$ are the amplitudes of the m^{th} mode propagating towards $z = +\infty$ and $z = -\infty$, respectively. The propagation constant is related to the effective refractive index of the fiber through $\beta = 2\pi n_{\text{eff}}/\lambda$. In an ideal waveguide the transverse mode fields are orthogonal and no mechanism exist to transfer energy between the modes. A pertubation such as the modulation of the core permitivity seen in a Bragg grating will introduce coupling between

[1] Assuming a positive index change during UV exposure as seen in Type I gratings (Chapter 3).

the modes. The transverse coupling coefficient between modes m and q is given by

$$C_{qm}^{\mathrm{T}} = \frac{\omega}{4} \int\int \Delta\varepsilon(x,y,z)\mathbf{e}_q^{\mathrm{T}}(x,y) \cdot \mathbf{e}_m^{\mathrm{T}^*}(x,y)\, dx\, dy \tag{4.6}$$

where the integration is over the full (x,y)-plane. For a weak pertubation, δn, in the refractive index, n, of a dielectric, the permitivity pertubation is given by $\Delta\varepsilon = 2n\,\delta n$. Assuming a uniform photosensitivity in the waveguide core and no change in the refractive index of the cladding, the transverse coupling coefficient can be written as

$$C_{qm}^{\mathrm{T}} = \zeta_{qm}(z) + 2\kappa_{qm}\cos\left[\frac{2\pi}{\Lambda_{\mathrm{mod}}}z + \varphi(z)\right] \tag{4.7}$$

where the coefficients appearing in this expression are given by

$$\zeta_{qm}(z) = \frac{1}{2}\,\omega\, n_{\mathrm{core}}\,\overline{\delta n}_{\mathrm{core}}(z) \int\int_{\mathrm{core}} \mathbf{e}_q^{\mathrm{T}}(x,y)\mathbf{e}_m^{\mathrm{T}^*}(x,y)\, dx\, dy \tag{4.8}$$

$$\kappa_{qm}(z) = s\,\zeta_{qm}(z)/2 \tag{4.9}$$

Equation 4.7 shows that $\zeta_{qm}(z)$ may be interpreted as a "dc" coupling coefficient while κ_{qm} is the "ac" coupling coefficient. The presence of a coupling mechanism allows for a transfer of energy from one mode to another. The evolution of the A_m and B_m coefficients introduced in Equation 4.5 is then described by

$$\begin{aligned}\frac{dA_m}{dz} &= i\sum_q A_q(C_{qm}^{\mathrm{T}} + C_{qm}^{\mathrm{L}})\exp[i(\beta_q - \beta_m)z] \\ &\quad + i\sum_q B_q(C_{qm}^{\mathrm{T}} - C_{qm}^{\mathrm{L}})\exp[-i(\beta_q + \beta_m)z]\end{aligned} \tag{4.10}$$

$$\begin{aligned}\frac{dB_m}{dz} &= i\sum_q A_q(C_{qm}^{\mathrm{T}} - C_{qm}^{\mathrm{L}})\exp[i(\beta_q + \beta_m)z] \\ &\quad - i\sum_q B_q(C_{qm}^{\mathrm{T}} + C_{qm}^{\mathrm{L}})\exp[-i(\beta_q - \beta_m)z]\end{aligned} \tag{4.11}$$

where C_{qm}^{L} is the longitudinal coupling coefficient. Equations 4.6 to 4.11 constitute the set of equation needed for the coupled-mode analysis. The complexity of these equations can be reduced significantly by a few assumptions as will be demonstrated below.

4.3 Bragg gratings

In optical waveguides satisfying the weak-guidance approximation the longitudinal coupling coefficients appearing in Equations 4.10 and 4.11 are significantly smaller than the transverse coefficients and are hence neglected. When considering reflection in single-mode fibers, where one ideal mode is coupled into an identical counter-propagating mode, only the $q = m$ terms contribute. By furthermore neglecting rapidly oscillating terms, which are not phase matched [11],

the equation system reduce to [49]

$$\frac{dP}{dz} = i\hat{\zeta}P(z) + i\kappa S(z) \tag{4.12}$$

$$\frac{dS}{dz} = -i\hat{\zeta}S(z) - i\kappa^* P(z) \tag{4.13}$$

where $P(z) = A(z)\exp(i\delta_{\mathrm{d}}z - \varphi/2)$, $S(z) = B(z)\exp(-i\delta_{\mathrm{d}}z + \varphi/2)$, and $\hat{\zeta}$ is defined as

$$\hat{\zeta} = \delta_{\mathrm{d}} + \zeta - \frac{1}{2}\frac{d\varphi}{dz} \tag{4.14}$$

δ_{d} is the detuning parameter describing the offset from the Bragg condition in the weak grating limit

$$\begin{aligned}\delta_{\mathrm{d}} &= \beta - \frac{\pi}{\Lambda_{\mathrm{mod}}} \\ &= 2\pi n_{\mathrm{eff}}\left[\frac{1}{\lambda} - \frac{1}{\lambda_{\mathrm{d}}}\right]\end{aligned} \tag{4.15}$$

where $\lambda_{\mathrm{d}} = 2n_{\mathrm{eff}}\Lambda_{\mathrm{mod}}$ is the design wavelength of an infinitesimally weak grating. In single mode optical waveguides the mode fields, $\mathbf{e}^{\mathrm{T}}(x,y)$, of the incident and reflected beams are identical and the coupling coefficients are given by the simple expressions [49]

$$\zeta(z) = \frac{2\pi}{\lambda}\overline{\delta n}_{\mathrm{eff}}(z) \tag{4.16}$$

$$\kappa(z) = \frac{s\pi}{\lambda}\overline{\delta n}_{\mathrm{eff}}(z) \tag{4.17}$$

where $\overline{\delta n}_{\mathrm{eff}}$ is the position dependent change in the effective refractive index averaged over a grating period. In chirp-free gratings $d\varphi/dz$ is zero and $\hat{\zeta}$ describes the detuning from the Bragg condition in the UV exposed optical waveguide with effective refractive index $n_{\mathrm{eff}}^{\mathrm{UV}}$.

The solution to the coupled-mode equations is simplified by introducing the local reflection coefficient

$$\rho(z) = \frac{S(z)}{P(z)} \tag{4.18}$$

Differentiating ρ and combining with Equations 4.12 and 4.13 leads to a Ricatti differential equation

$$\frac{d\rho}{dz} = -i(\kappa\rho^2 + 2\hat{\zeta}\rho + \kappa^*) \tag{4.19}$$

with boundary conditions determined by the grating. Consider the reflection of a forward-propagating wave from a Bragg grating positioned from $-L/2$ to $L/2$. At the beginning of the grating no depletion of the forward propagating wave has occurred, while no back-ward propagating wave exists after the grating. These boundary conditions can be expressed in terms of the field amplitudes by $P(-L/2) = 1$ and $S(L/2) = 0 \Rightarrow \rho(L/2) = 0$.

The measurable reflection, R, from the Bragg grating is given by

$$R = \rho(-L/2)\rho^*(-L/2) \tag{4.20}$$

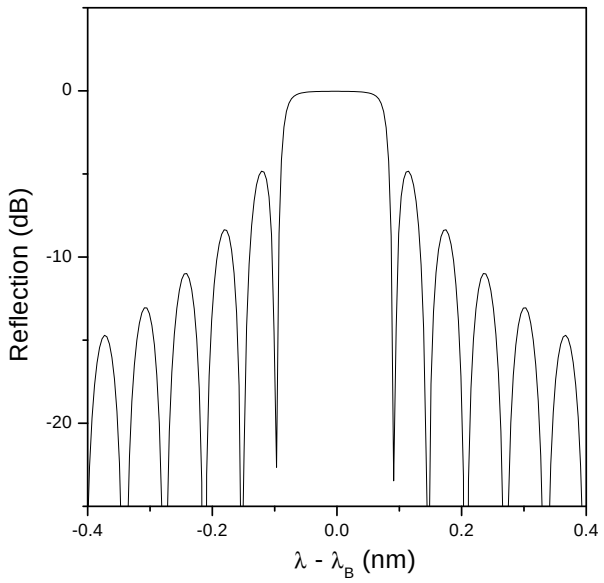

Figure 4.2: Reflection from a uniform grating with $\kappa L = 3.25$ plotted against the offset from the Bragg wavelength $\lambda_{\mathrm{B}} = \lambda_{\max}$ defined in Equation 4.24.

4.3.1 Uniform gratings

In chirp-free uniform gratings none of the coupling coefficients $\hat{\zeta}$ and κ appearing in the coupled differential equations in Equations 4.12 and 4.13 depend on the grating position z. Closed-form solutions can then be found when appropriate boundary conditions are specified. For a uniform Bragg grating with boundary conditions as described above, ρ can be written as

$$\rho(-L/2) = \frac{-\kappa \sinh(\varrho)}{\hat{\zeta}\sinh(\varrho) + i\sqrt{\kappa^2 - \hat{\zeta}^2}\cosh(\varrho)} \tag{4.21}$$

where $\varrho = \sqrt{(\kappa L)^2 - (\hat{\zeta}L)^2}$. The reflection coefficient is then given by

$$R = \frac{\sinh^2(\varrho)}{\left(-\frac{\hat{\zeta}}{\kappa}\right)^2 + \cosh^2(\varrho)} \tag{4.22}$$

An example of the reflection from a 12.5 mm long uniform grating with $\kappa L = 3.25$ is seen in Figure 4.2. The reflection from the grating takes its maximum value

$$R_{\max} = \tanh^2(\kappa L) \tag{4.23}$$

when $\hat{\zeta} = 0$. In a chirp-free grating this corresponds to setting $\delta_{\mathrm{d}} + \zeta = 0$. The wavelength, $\lambda_{\max}$, derived from this expression is given by

$$\lambda_{\max} = \lambda_{\mathrm{d}}\left(1 + \frac{\overline{\delta n}_{\mathrm{eff}}}{n_{\mathrm{eff}}}\right) \tag{4.24}$$

This equation shows that the wavelength, where maximum reflection from the grating is obtained, equals the design wavelength plus a term describing the shift in center wavelength due to the grating inscription. Measuring the change in the center wavelength of a grating during UV illumination will evidently provide information about the change in the effective refractive index and thus about the photosensitivity of the optical waveguide. Several such growth curves are presented in Chapter 3. $\lambda_{\max}$ is usually referred to as the Bragg wavelength, λ_B, of the grating.
By utilizing the approximate relation $\delta n_{\text{eff}} = \eta n_{\text{mod}}$ the expression for the coupling coefficient κ given in Equation 4.17 may be rearranged to

$$\kappa = \frac{\pi \eta n_{\text{mod}}}{\lambda} \tag{4.25}$$

The "ac" coupling coefficient κ is thus linearly proportional to the index modulation amplitude and the confinement factor. A large modulation of the refractive index of a fiber with a strong confinement of the mode to the perturbed waveguide core will thus result in a highly reflecting grating. By straightforward reorganization of Equations 4.23 and 4.25 a formula for the refractive index modulation amplitude is found

$$n_{\text{mod}} = \frac{\lambda}{2\pi\eta L} \ln \left[\frac{1 + \sqrt{1 - 10^{\frac{T[dB]}{10}}}}{1 - \sqrt{1 - 10^{\frac{T[dB]}{10}}}} \right] \tag{4.26}$$

where $T[dB] = -10 \cdot \log(1 - R)$ is the transmission loss given on the dB scale. From the measured transmission spectra during an UV exposure the refractive index modulation amplitude can hence be derived.

4.4 Apodized gratings

The strength of the side lobes of a uniform grating makes it unsuitable as a component for WDM systems. By apodizing the grating it is possible to suppress these side lobes to an acceptable level. In this study only a few of the many existing apodization profiles has been applied and the author refers to [11] for further description of the most commonly used apodization profiles. A closed-form solution to the coupled mode equations only exists for uniform Bragg gratings. In weak gratings with a small coupling between the forward and backward propagating modes an approximate expression for the reflection can be derived for arbitrary apodization profiles. Considering chirp-free gratings only and substituting

$$\rho(z) = \sigma^*(z) \cdot \exp\left(-i\, 2\hat{\zeta}\, z\right) \tag{4.27}$$

into Equation 4.19 and neglecting the σ^2 term the following differential equation is obtained

$$\frac{d\sigma}{dz} = i\kappa(z) \exp\left(-i\, 2\hat{\zeta}\, z\right) \tag{4.28}$$

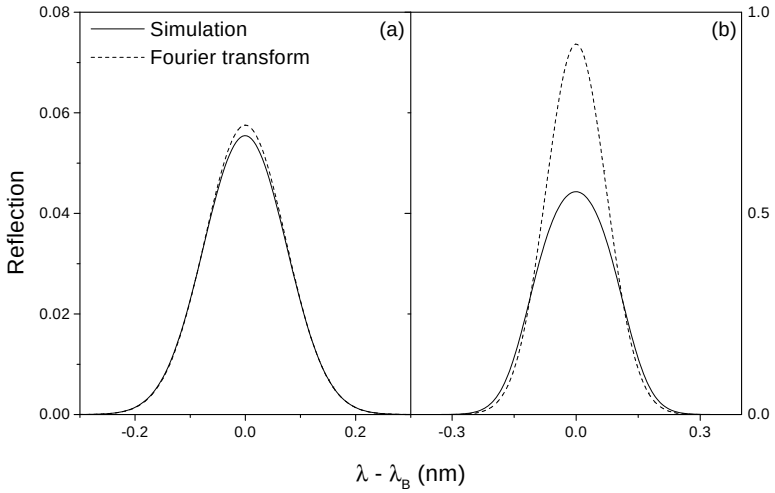

Figure 4.3: Reflection from 10 mm long Bragg gratings with Gaussian apodization of the index modulation profile, both with a taper parameter of $s = 0.3$. The full lines show the simulated reflection, while the dotted lines are calculated from the Fourier transform of the coupling coefficient $\kappa(z)$. The maximum index modulation amplitudes used in the two gratings are: (a) $n_{\mathrm{mod}} = 0.5 \times 10^{-4}$ and (b) $n_{\mathrm{mod}} = 2 \times 10^{-4}$.

An expression for $\sigma(z)$ can then be obtained by integration and applying the boundary condition $\sigma(L/2) = 0$. Since $\kappa(z)$ is finite only in the grating region the integration can be performed from $-\infty$ to ∞. Given that $|\sigma|^2 = |\rho|^2$, the reflection from the grating can be written as

$$R(\hat{\zeta}) = |\sigma(-L/2)|^2 = \left| \int_{-\infty}^{\infty} \kappa(z) \exp\left(-i\, 2\hat{\zeta}\, z\right) dz \right|^2 \tag{4.29}$$

$\hat{\zeta} = \zeta + \delta_{\mathrm{d}}$ depends on the offset from the center wavelength, $\Delta\lambda = \lambda - \lambda_{\mathrm{B}}$ through

$$\hat{\zeta} = -\frac{2\pi n_{\mathrm{eff}}^{\mathrm{UV}}}{\lambda_{\mathrm{B}}^2} \Delta\lambda \tag{4.30}$$

The reflection spectrum from a weak Bragg grating is thus centered at the Bragg wavelength, λ_{B}, and the spectral shape is given by the Fourier transform of the "ac" coupling coefficient $\kappa(z)$. The described Fourier analysis is only strictly valid for weak gratings as mentioned above and illustrated in Figure 4.3. This figure shows a comparison between the simulated reflection and the response calculated from the Fourier transform approximation for two Gaussian gratings[2] with refractive index modulation amplitudes $n_{\mathrm{mod}} = 0.5 \times 10^{-4}$ and $n_{\mathrm{mod}} = 2 \times 10^{-4}$. The transmission loss at the Bragg wavelength of the two gratings are 0.25 dB and 3.5 dB respectively. The Fourier analysis evidently fails to predict

[2] Gaussian gratings are introduced in Section 4.4.2.

the response for strong gratings. It still supplies a good starting point for the design of stronger gratings though.

4.4.1 Calculating grating spectra

The amplitude and phase response from non-uniform Bragg gratings outside the non-depleted beam limit can be calculated by using the Transfer Matrix Method (TMM) [52]. The apodized grating is divided into a number of approximately uniform segments. In each of these segments an analytical solution to the coupled mode equations describing the beam propagation exits. The transfer through a given subsection, say i, is described by the matrix $\mathbf{T}_i$. The response from the whole grating is then calculated from

$$\overline{\mathbf{T}}_{\text{tot}} = \prod_{i=1}^{N} \overline{\mathbf{T}}_i \tag{4.31}$$

4.4.2 Gaussian gratings

The refractive index modulation amplitude profile in a Gaussian grating can be written as

$$n_{\text{mod}}(z) = n_0 \exp\left[-\ln(2) \left(\frac{2(z - z_0)}{s_{\text{Gauss}} L} \right)^2 \right] \tag{4.32}$$

where n_0 is the maximum modulation amplitude obtained at the center of the grating z_0. The FWHM of the grating equals $s_{\text{Gauss}}L$, where L is the grating length and s_{Gauss} the taper parameter. Gaussian apodization of the refractive index modulation amplitude results in a Gaussian shaped reflection peak as seen immediately from the Fourier transform described above. If a grating is written with a Gaussian shaped UV beam parked at the same position during the exposure, the effective refractive index also varies along the grating. This is unfortunate since a significant chirp in the grating is introduced causing strong side lobes at the short wavelength side of the reflection peak. Bragg gratings with a modulation amplitude profile defined by scanning the UV beam with a variable speed along the fiber also show this variation as seen in Figure 4.4(a) In raised Gaussian gratings, where the average refractive index is constant throughout the grating the side lobes can be reduced to a level below $-60\,\text{dB}$ as illustrated in Figure 4.4(b).
Defining the Band Width Utilization (BWU) factor as the ratio between the 1 dB- and the 30 dB-bandwidth of the grating the raised Gaussian grating presented in Figure 4.4(b) is seen to have a BWU of 0.35. This low value indicate that the Gaussian grating is utilizing the wavelength span poorly. The efficiency can be improved by using other apodization profiles as shown in the following section.

4.4.3 Sinc gratings

The ideal grating for WDM systems is characterized by a constant reflection in the stop band and only negligible reflection in the pass band. Fourier analysis

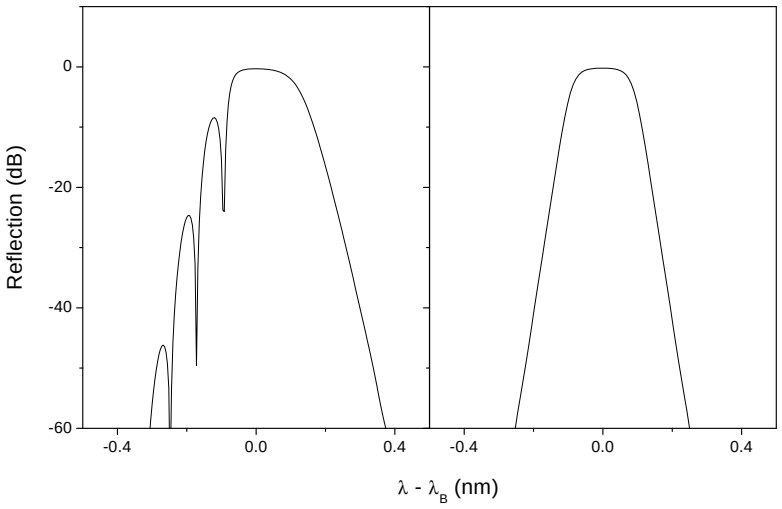

Figure 4.4: Reflection calculated for Bragg gratings with Gaussian apodization of the index modulation profile: (a) $\overline{\delta n}_{\text{core}} \propto n_{\text{mod}}$, (b) constant $\overline{\delta n}_{\text{core}}$. Both gratings are 23 mm long with taper parameter $s = 0.3$ and $n_{\text{mod}} = 2 \times 10^{-4}$.

shows that for weak gratings such a square-like reflection spectrum is obtained by a sinc-apodization of the refractive index modulation. The apodization profile in a sinc grating is written as

$$n_{\text{mod}}(z) = n_0 \frac{\sin\left[2\pi\left(\frac{z-L/2}{s_{\text{sinc}} \cdot L}\right)\right]}{2\pi\left(\frac{z-L/2}{s_{\text{sinc}} \cdot L}\right)} \tag{4.33}$$

An example of a 23 mm long sinc grating with a taper parameter of $s_{\text{sinc}} = 1/6$ is shown in Figure 4.5(a). The sinc profile requires a periodic change in the sign of n_{mod} at positions given by $z = m/2 \cdot sL, m = 1, 2, ...$ This change is realized by a π-phase shift in the grating modulation profile.
The simulated reflection spectrum of a sinc grating is compared with that of a Gaussian grating in Figure 4.6(b). Both gratings have a 1 dB transmission loss at the Bragg wavelength. The apodization profiles used in the simulations are shown in Figure 4.6(a). The reflection spectra presented in this figure clearly show the improved utilization of the optical waveguide bandwidth when applying a sinc apodization as compared to a Gaussian apodization. The "ringing" observed in the reflection from the sinc grating is due to the so-called Gibbs phenomenon [53], and is related to the abrupt termination of the apodization profile. By further apodizing the sinc index modulation profile with a Gaussian taper function a smooth transition from grating to no grating section is obtained. This suppresses effectively the ringing on both the top and sides of the reflection peak, thus increasing the side lobe suppression and giving an almost constant reflection in the stop band.

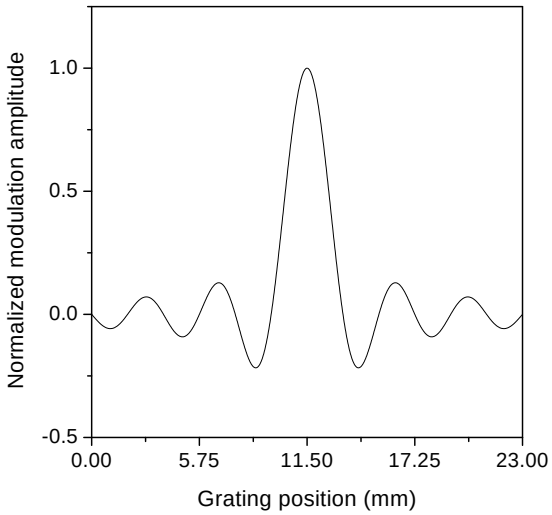

Figure 4.5: Normalized refractive index modulation amplitude n_{mod}/n_0 of a typical 23 mm long sinc grating fabricated in this study. The taper parameter equals $s_{\mathrm{sinc}} = 1/6$. Grating segments with negative values of n_{mod} are phase shifted by π relative to segments with positive values

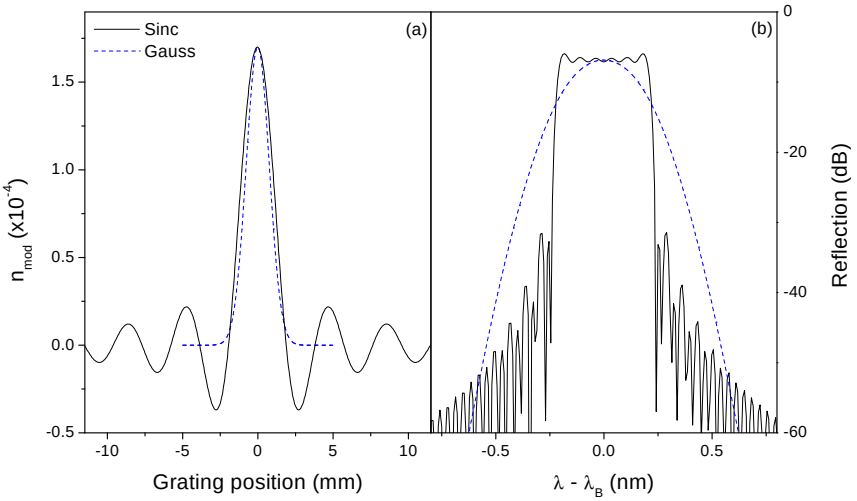

Figure 4.6: (a) Apodization profiles for sinc and Gaussian Bragg gratings of similar strength. (b): The corresponding simulated reflection spectra of weak gratings with a transmission loss of 1 dB at the Bragg wavelength.

4.5 Phase properties of Bragg gratings

The group delay and dispersion of the optical signal reflected from a Bragg grating is related to the phase, θ_p, of the reflection amplitude coefficient ρ. The derivative of the phase $\tau_p = d\theta_p/d\omega$ is identified as the group delay [49] and τ_p can be written as

$$\tau_p = -\frac{\lambda^2}{2\pi c}\frac{d\theta_p}{d\lambda} \tag{4.34}$$

The group delay is symmetric around the center wavelength of the grating similar to the observed reflection spectrum as illustrated in Figure 4.7(b). The dispersion, d_p, of the reflected signal is given by the wavelength derivative of the group delay.

$$\begin{aligned} d_p &= \frac{d\tau_p}{d\lambda} \\ &= -\frac{2\pi c}{\lambda^2}\frac{d^2\theta_p}{d\omega^2} \end{aligned} \tag{4.35}$$

where ω is the temporal frequency of the optical mode. In strong gratings with a large bandwidth the delay is nearly constant at wavelengths around the center wavelength, while in weaker gratings it varies significantly within the whole bandwidth of the grating.

4.6 Design of Bragg gratings

Bragg gratings with requested amplitude and phase responses can be designed by using a layer-peeling algorithm [3]. The grating is approximated by a series of discrete layers with constant coupling coefficients, which are unknown at the beginning of the process. A uniform layer thickness is used thus making the time, Δ, it takes a wavefront to cross any layer constant. The impulse response from the grating at the time $2(N+1)\Delta$ is independent of the grating profile after the $N+1$ layer. Assuming that the coupling coefficients of the N first layers are known, the coefficient for the $N+1$ layer can be deduced by comparing the impulse response on the truncated grating with the desired response from time 0 to $2(N+1)\Delta$. The coupling coefficients of the gratings are thus determined by an iterative approach, where the coefficient for each successive layer is deduced from the coupling coefficients of the previous layers and the requested response from the grating.

4.7 Sampled gratings

Sampled gratings can be fabricated by inserting an amplitude mask just above the phase mask as illustrated in Figure 4.8. Sampling a Bragg grating results in multiple peaks in the reflection spectrum with a periodicity determined by the sampling period. This can immediately be seen by applying the Fourier analysis described previous in this chapter linking the Fourier transform of the coupling coefficient, $\hat{\mathbf{F}}[\kappa(z);\hat{\zeta}]$, to the reflection spectrum of the grating. The coupling

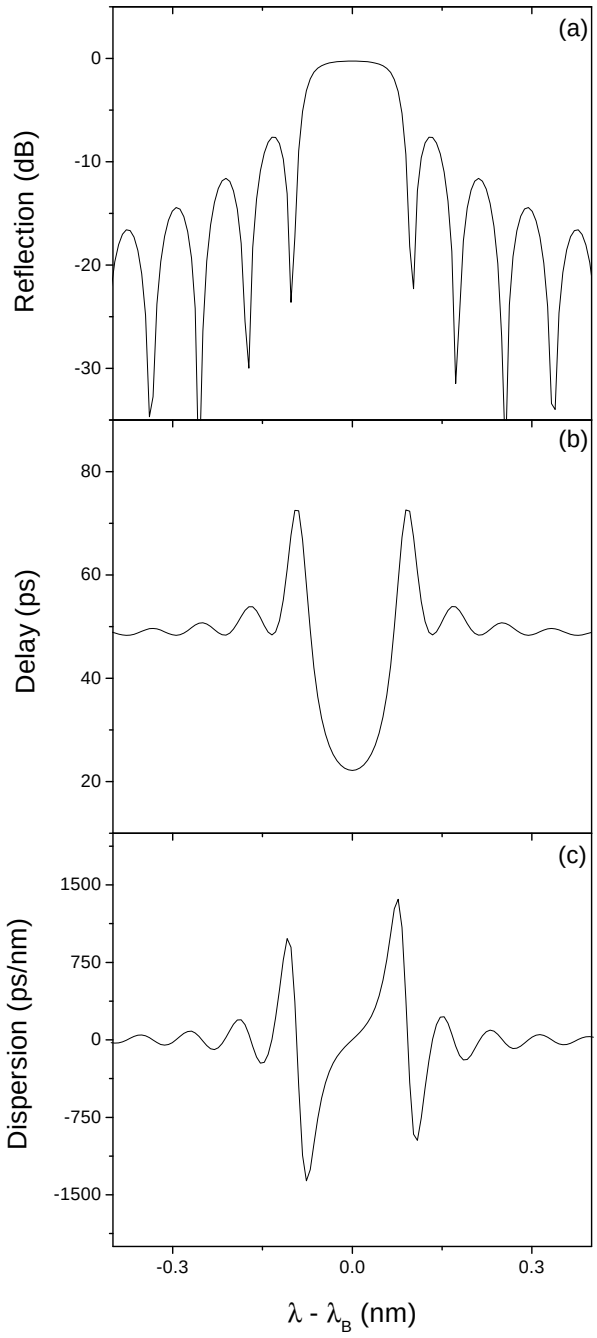

Figure 4.7: Simulated amplitude and phase response from a 10 mm long uniform grating with $\kappa L = 2$: (a) reflection, (b) group delay and, (c) dispersion

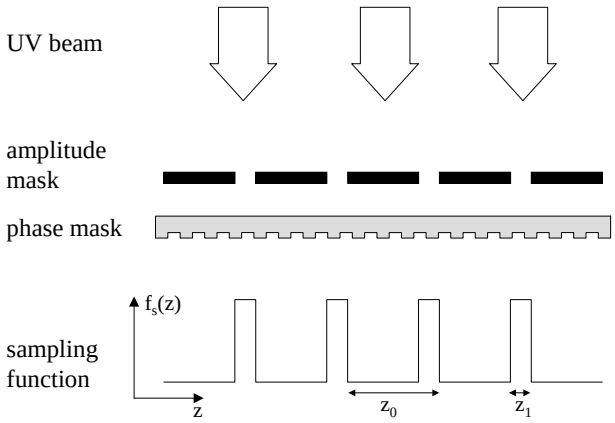

Figure 4.8: Sampled gratings can be fabricated by using an amplitude mask [54], which determines the period, z_0, of the sampling function and the sub-grating length z_1.

coefficient in a sampled Bragg grating can be written as $\kappa_{\mathrm{s}}(z) = g(z) \cdot f_{\mathrm{s}}(z)$, where $f_{\mathrm{s}}(z)$ is the sampling function and $g(z)$ is the apodization of the whole sampled grating. The sampling period and the length of the individual sub-gratings are referred to as z_0 and z_1, respectively. In the following analysis only chirp-free gratings are considered and the author refers to Chin-Hua *et al.* [55] for a treatment of chirped sampled gratings.

In general a multiplication in real space results in a convolution in Fourier space

$$\hat{\mathbf{F}}[g(z) \cdot f(z); \hat{\zeta}] = \frac{1}{2\pi} \int_{-\infty}^{\infty} G(\hat{\zeta} - \hat{\zeta}')\, F(\hat{\zeta}')\, d\hat{\zeta}' \tag{4.36}$$

where $F(\hat{\zeta}) = \hat{\mathbf{F}}[f(z); \hat{\zeta}]$ and $G(\hat{\zeta}) = \hat{\mathbf{F}}[G(z); \hat{\zeta}]$ are the Fourier transforms of $f(z)$ and $g(z)$, respectively. Let $f(z) = f_{\mathrm{s}}(z)$ describe the sampling function, which is assumed to consist of a infinite train of sub-gratings. The corresponding Fourier transform is a series of equally spaced discrete frequencies $F(\hat{\zeta}) = 2\pi \sum_j \delta(\hat{\zeta} - \hat{\zeta}_j)$. Direct insertion in Equation 4.36 then yields

$$\hat{\mathbf{F}}[g(z) \cdot f_{\mathrm{s}}(z); \hat{\zeta}] = 2\pi \sum_j G(\hat{\zeta} - \hat{\zeta}_j) \tag{4.37}$$

The reflection spectrum from a sampled grating hence shows a number of equally spaced peaks with the spectral shape of the individual peaks given by the Fourier transform of the overall grating apodization profile. The center wavelength of the j^{th} reflection peak can be derived from $\hat{\zeta}_j = 0$:

$$\hat{\zeta}_j = \hat{\zeta}_{\mathrm{U}} - j\frac{\pi}{z_0} \tag{4.38}$$

where $\hat{\zeta}_{\mathrm{U}}$ is the detuning parameter of a uniform grating. The center peak, $j = 0$, center wavelength thus equals the Bragg wavelength of an equivalent

non-sampled grating and the spacing between two adjacent reflection peaks may be approximated by

$$\Delta\lambda \approx \frac{2n_{\text{eff}}^{\text{UV}}\Lambda_{\text{mod}}^2}{z_0} = \frac{n_{\text{eff}}^{\text{UV}}\Lambda_{\text{mask}}^2}{2z_0} \tag{4.39}$$

Also the individual sub-gratings may be apodized. The Fourier transform of the sub-grating apodization profile determines the spectral shape of the overall reflection spectrum of the sampled grating [56]. In a uniform sampled grating the strength of the j^{th} reflection peak is thus given by

$$R_j = \tanh^2(|\kappa_j|L) \tag{4.40}$$

where L is the length of the sampled grating and the j^{th} coupling coefficient equals [54]

$$\kappa(j) = \kappa_0 \frac{z_1}{z_0} \frac{\sin(\pi j \frac{z_1}{z_0})}{\pi j \frac{z_1}{z_0}} e^{-i\pi j \frac{z_1}{z_0}} \tag{4.41}$$

The reflection from sampled gratings written in planar waveguides are studied in Chapter 7.

Chapter 5

Experimental setup

5.1 Introduction

This chapter gives a short introduction to the equipment and optical components used in the experimental setup. The first section is dedicated to the description of the UV sources used in this study, while Section 5.3 briefly describes the optical setup including the hardware and software designed to control this. Finally, the phase mask used in the grating inscription is presented in Section 5.4. The lasers, guiding optics and phase masks are the basic building blocks of many optical laboratories and are hence only described briefly. The new setup designed for the novel polarization control method experiments is described in detail in Chapter 6.

5.2 Laser sources

In the presented study three different laser sources emitting in the ultraviolet (UV) range were used; one pulsed excimer laser and two continuous wave (cw) lasers. This section describes briefly the principle of operation of the different lasers and their optical properties.

5.2.1 Excimer laser

When using a gas mixture of krypton and flourine, the excimer laser emits $100-300\,\mathrm{mJ}$ pulses at a wavelength of $248\,\mathrm{nm}$. The pulse duration is in the order of $20\,\mathrm{ns}$ resulting in a peak power of $5-15\,\mathrm{MW}$. When running at a repetition rate of $30\,\mathrm{Hz}$ this corresponds to an average power of $3-9\,\mathrm{W}$. The optical properties of the excimer laser used in this study was carefully investigated by Jörg Hübner and the author refers to his thesis [56] and references therein for a detailed description of the excimer laser and its optical properties. The general principle of operation is the creation of the highly unstable KrF molecule, which has a lifetime in the order of nanoseconds. The reaction between the noble gas krypton and florine requires a large amount of energy, which is supplied by a homogeneous discharge of the gas. In order to ensure homogenity, the gas is preionized prior to the discharge. Helium and Neon are used as buffer gas absorbing

the kinetic energy of the krypton and flourine atoms after dissociation. Given lifetime of the excited KrF molecule and the cavity length of approximately 1 m the photons only experience a few round trips before leaving the laser cavity. This gives a limited pulse shaping and a large proportion of the beam power is emitted in higher order modes.
The beam shape is rectangular with an almost constant intensity along the long axis, henceforth referred to as the top-hat profile, while the short axis has a Gaussian profile. The excimer laser used in this study was equipped with unstable resonators resulting in a beam divergence in the order of 0.4 mrad along both axes. The spatial coherence length, L_{coh} describing the divergence induced transverse nonuniformity of the excimer pulse is 250 μm and 350 μm for the Gaussian and top-hat profiles respectively [56]. The temporal coherence length, L_{coh}^{temp}, is inversely proportional to the spectral bandwidth $\Delta\lambda$ of the laser. Due to the poor mode shaping in the excimer laser L_{coh}^{temp} is only in the order of 30 μm. The limited temporal coherence makes the excimer laser unsuitable for holographic writing techniques, but causes no problems when using direct writing with a phase mask (Section 5.4). Using normal incident light the diffracted 1^{st} and -1^{st} order beams travel the same distance from the phase mask to the waveguide core and even the slight difference in the path length when using the polarization control method is below 1 μm and the short temporal coherence length is not a significant problem.
The pulse to pulse intensity fluctuations normally averages out during exposures where the waveguide is exposed to thousands of pulses at any given point along the Bragg grating. When using ultra high pressure loaded high-germanium content fibers, which are highly sensitive to UV light, the number of pulses required is significantly smaller and may in weak or medium strength gratings not be sufficiently high to average out these fluctuations.
In spite of the shortcomings with the limited coherence and the pulse to pulse fluctuations, the excimer laser still offers an attractive robust source of high intensity ultraviolet light for inscription of Bragg gratings in optical waveguides.

5.2.2 High coherence sources

The poor beam quality of the excimer laser limits its use in the fabrication of very delicate gratings. Attractive alternatives for UV writing of very high quality gratings are the intracavity frequency doubled argon ion (FDA) and the diode pumped all-solid-state (DPSS) lasers both operating continuous wave (cw).

Frequency doubled Argon ion laser

In the initial stage of this study a frequency doubled argon ion Innova 300 FreD laser operating at 244 nm was available. This laser emits only a single line with a temporal coherence length in excess of 1 cm [44]. An output power of 50 mW was obtained when the laser was running close to the maximum tube current. Thorough spatial filtering, using 10 μm or 15 μm pinholes, was required in order to remove non-Gaussian components of the beam. The spatial

filtering and loss at other components in the optical setup reduced the beam power to 15 mW on the sample. The beam was slightly astigmatic, which should be taken into account when using a highly focused beam. It was linearly polarized in the horizontal direction. This laser was used in the investigation of the photosensitivity of non-sensitized and deuterium loaded optical fibers for a comparative study of the efficiency of the FreD laser with that of a quadrupled Nd:YAG laser as described in Section 3.5.

Diode pumped Solid state laser

The Spectra Physics LAS DeltaTrain diode-pumped all-solid-state (DPSS) laser [57] offers improved beam quality relative to the excimer and a easier day-to-day use than the frequency doubled argon ion laser. It uses an actively stabilized unidirectional ring cavity to frequency double a diode-pumped Nd:YAG laser with intracavity frequency doubling at 532 nm. The resulting output beam has an excellent quality and good pointing stability. Furthermore the 2 hours warm-up time required when using FDA lasers is not necessary. It emits up to 300 mW cw at a wavelength of 266 nm. The reduced photosensitivity this far away from the 242 nm absorption peak in germanosilicate glass is partially compensated by the high output power and the high quality beam shape, which makes the power consuming spatial filtering needless.

5.3 Optical setup

Two separate optical setups were active during this study. A laboratory with an excimer laser and another with the cw lasers described above.

5.3.1 Excimer laboratory

High power optics was used throughout this setup due to the very high peak power of the excimer pulses. When the pulses are emitted the long axis is aligned vertically. The mirrors used to guide the beam towards a rail with lenses and the final mirror rotate the beam 90°, so that the short axis of the beam is aligned with the direction of motion of the translation stage. In this setup the beam is moved relative to the optical waveguide. The laser is equipped with a red diode acting as a guide when aligning the mirrors and subsequently the waveguide relative to the beam. Both dimensions of the beam are focused using Galilean beam telescopes. This is a two-lens system, with the general expression for the resulting focal length f:

$$f = \frac{f_1 f_2}{f_1 + f_2 - d} \tag{5.1}$$

where f_1 and f_2 are the focal lengths of the first and second lenses respectively, and d is the distance between the lenses. When the Galilean telescope is set to work as a beam compressor a focusing lens with focal length f_1 is placed in front of an expanding lens of focal length $-f_2$. If the distance d is chosen so

that it equals the sum of the focal lengths, the beam emerging from the compressor is a collimated beam with a magnification s equal to the ratio f_2/f_1. Using the lenses available in the excimer laboratory, the beam was focused by approximately a factor two in both dimensions. The lenses are mounted on the same rail as the last of the guiding mirrors. Any deviation from the ideal lens distance would otherwise result in a change in the beam size, and thereby beam intensity, when the last mirror is moved along the optical waveguide. When only the center part of the beam is used, UV absorbing glass plates are placed after the lenses, thereby defining the beam dimensions. For the dual scan gratings presented in this thesis simulations using a convolution of the scanned profile with the almost uniform center part of the Gaussian beam profile, showed that the beam size along the waveguide should be kept below 2 mm. This is also close to the limit, where the assumption that the center part of the Gaussian profile has a uniform intensity profile still is valid.
Software was designed using the commercial graphical programming language Labview from National Instruments. Uniform, Gaussian and raised Gaussian exposure profiles were programmed with the velocity of the translation stage being controlled during the exposure.
When the polarization control method was implemented new software was designed in collaboration with Poul Varming and Nikolai Plougmann and new optics was included. The modifications required to implement this novel method are explained in Section 6.6.

5.3.2 Cw laboratory

Given the relatively low peak power supplied by the cw lasers, the optics for this laboratory does not need to be suited for high power performance. Given the dimensions of the beam spot and the quality of the beam it is evident that this setup requires very delicate optics in order to utilize the high beam quality. After a Gaussian expansion of the beam, where the spatial filtering mentioned in Section 5.2.2 is made, an aperture removes the fringes on the beam. Mirrors guide the beam towards a stationary rail where the last guiding mirror is mounted. The beam is focused either by a spherical lens positioned just above the sample or a cylindrical lens situated on the rail before the mirror. By using the spherical lens a beam diameter of 20 μm was obtained. With such a beam, wavelength tuning of Bragg gratings in individual waveguides on a planar waveguide was accomplished. When exposing optical fibers a cylindrical lens was primarily used focusing the spherical beam in the direction perpendicular to the waveguide to a beam width of 100 μm. A schematic presentation of the optical setup for the cw laboratory is seen in Figure 5.3.2.

Software was designed to facilitate UV writing in planar waveguides of any shape with uniform, Gaussian or raised Gaussian modulation profiles. As opposed to the excimer laboratory the laser is running at all times and a computer controlled shutter turns the beam on and off. This is done to ensure a stable laser performance and beam position. Two computer controlled translation stages facilitate full x-y control of the optical waveguide position relative to the beam. When using the relatively small cw beam compared to the excimer

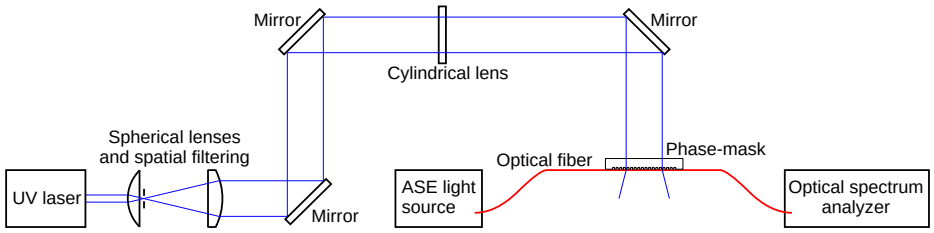

Figure 5.1: Schematic presentation of the setup used to write Bragg gratings in the cw laboratory.

beam, it is evidently important to be able to align the cw beam correctly on the optical waveguide. The waveguide itself may be placed under any angle relative to the x-y coordinate system defined by the translation stages. Two positions on the waveguide are determined using the blue luminescence seen during UV exposure of the germanium doped core. Either the luminescence is measured directly with an optical spectrum analyzer while scanning across the waveguide or alternatively the designed software, which store digital images of the blue luminescence during a scan and analyze these images to find the position giving the maximum luminescence is used. Due to the rapid initial decay of the blue luminescence it is of vital importance when determining these positions that the part of the waveguides used for this purpose is partially bleached by UV exposure prior to this routine.
It is furthermore possible to evaluate the beam profile by scanning a pigtailed fiber through the UV beam, while measuring the blue luminescence with an optical spectrum analyzer [47]. This procedure enables the user to characterize the beam shape and to some extent the beam size, when changes in the optical setup have been made.
The use of this setup has unfortunately been limited due to the age of the FDA laser and problems with the purchased DPSS laser, which only has worked satisfactorily for 2 days in the first 5 months after its initial delivery.

5.4 Phase mask

The holographic side-writing method for UV writing of Bragg gratings first presented by Meltz *et al.* [58] requires high coherence lasers. In order to obtain an interference pattern the output from the laser is divided into two beams, which subsequently are combined again at the fiber. This procedure evidently put some strong demands on the temporal coherence length of the laser beam in order to obtain high visibility modulation profiles. When Hill *et al.* introduced the side-writing method [59] the requirements on the laser coherence were reduced significantly. By using a phase mask the distance from the diffracting

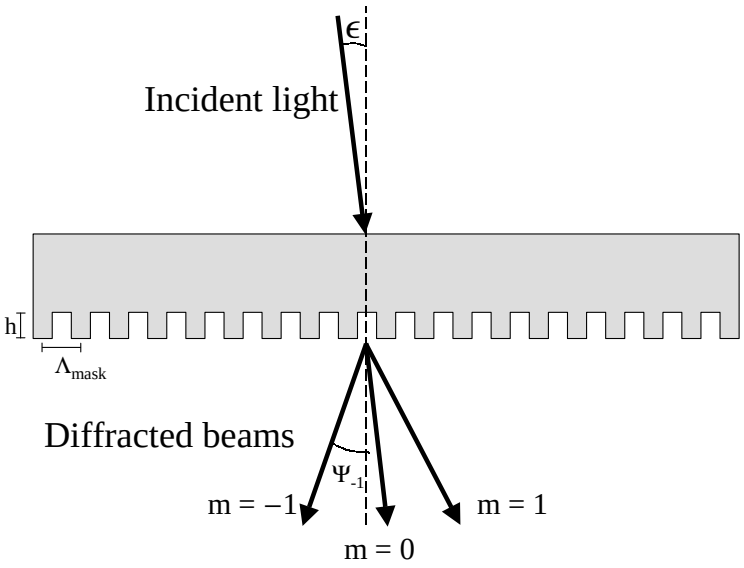

Figure 5.2: Schematic picture of a phase mask used for direct writing of Bragg gratings. With accurate control of the height h and duty cycle of the corrugation the zero order diffraction is effectively suppressed.

phase mask to the waveguide core is in the order of 100 μm and the path length difference between the interfering beams is significantly smaller. The development of the phase mask method opened up for the use of low coherence lasers, such as the excimer laser described in Section 5.2.1, in the fabrication of Bragg gratings in optical waveguides.
A phase mask consists of a piece of UV transparent glass with a periodic corrugation on the bottom side as depicted in Figure 5.2. The corrugation pattern is etched precisely to a depth h, where light propagating at λ_{UV} through a section with glass is exactly π out of phase with light that has propagated in an etched section:

$$h(n_{silica} - n_{air}) = m\frac{\lambda_{\mathrm{UV}}}{2}, \tag{5.2}$$

where m is an odd integer. When the ratio between the width of the etched regions and their mutual distance also is carefully designed, the power in the zero order diffracted beam can be reduced significantly. With the accuracy of present day phase mask production facilities, devices with zero order suppression in excess of 99% may be fabricated. The optical power then propagates primarily in the -1^{st} and 1^{st} orders of the diffracted beam at angles Ψ_1 and Ψ_{-1} relative to the normal of the phase mask given by

$$\sin\Psi_{\pm 1} = \pm\frac{\lambda_{\mathrm{UV}}}{\Lambda_{\mathrm{mask}}} + \sin\epsilon \tag{5.3}$$

where Λ_{mask} is the periodicity of the phase mask corrugation. With careful alignment of the angle ϵ of the incident light relative to the normal of the phase mask, the $\sin\epsilon$ contribution is negligible. The period Λ_{intf} of the pattern created when the 1^{st} and -1^{st} order beams interfere is then given by

$$\Lambda_{\text{intf}} = \frac{\lambda_{\text{UV}}}{2\,\sin\Psi_{\pm 1}} = \frac{\Lambda_{\text{mask}}}{2} \tag{5.4}$$

Light propagating in a waveguide with an effective refractive index n_{eff} will be reflected by a given Bragg grating when the vacuum wavelength λ matches the Bragg condition

$$\tilde{m}\frac{\lambda}{2n_{\text{eff}}} = \Lambda_{\text{intf}}, \qquad \tilde{m} = 1, 2, .. \tag{5.5}$$

where $\tilde{m}$ is the reflection order. All the spectra presented in this thesis show the first order reflection $\tilde{m} = 1$. This leads to the simple expression for the wavelength, λ_{Bragg}, at which light is reflected from a Bragg grating written in a waveguide with effective refractive index, n_{eff}, using a phase mask with periodicity, Λ_{mask},

$$\lambda_{\text{Bragg}} = n_{\text{eff}}\Lambda_{\text{mask}} \tag{5.6}$$

5.4.1 Significance of spatial coherence length

As mentioned earlier in 5.2.1 the limited spatial coherence length of the excimer laser is not a major problem, when the phase mask is positioned in direct contact with the waveguide. In the implementation of the polarization control method a distance, z_{air}, between the phase mask and the optical fiber is required. The transverse distance, d, between the positions on the phase mask from where the 1^{st} and -1^{st} order diffracted beams interfering at a certain lateral waveguide position originate from, is given by

$$d \approx 2[z_{\text{air}}\,\phi + z_{\text{clad}}\,\phi/n_{\text{clad}}] \tag{5.7}$$

where z_{clad} and n_{clad} is the cladding thickness and refractive index at UV wavelengths, respectively. The maximum distance z_{max} the waveguide can be placed away from the phase mask is found by demanding that $d < L_{\text{coh}}$. With the optical components used in our setup, the phase mask to fiber distance is in the order of $60\,\mu$m, which is well below the value of $z_{\text{max}} \approx 500\,\mu$m calculated using data for standard telecommunication fibers together with the spatial coherence length of the excimer laser of $L_{\text{coh}} = 250\,\mu$m.

Chapter 6

Polarization control method

6.1 Introduction

The motivation for the development of the polarization control method is the desire for a flexible, stable and easy-to-use method for UV writing of Bragg gratings with advanced apodization profiles including several discrete phase shifts. The double-exposure technique [60] can be used to write chirp-free gratings with an apodization of the refractive index modulation amplitude profile. It is relatively simple to use, but is incapable of producing Bragg gratings with phase shifts. Using advanced phase masks with variable diffraction efficiency [61] allows for inscription of simple apodized modulation profiles. Phase shifts may also be incorporated in the phase mask [62] and gratings for DFB lasers may be written directly. The phase mask design approach supplies a highly controlled and thus very reproducible method for UV writing of Bragg gratings with slightly advanced index modulation profiles. The design and production of phase masks for more advanced gratings with e.g. sinc shaped apodization profiles is complicated and no reports on the fabrication of highly advanced gratings using custom designed phase masks has been given. Another disadvantage of the phase mask design approach is that every phase mask only applies for a single type of grating. Yet another approach is post-exposure treatment by e.g. local UV exposure [63] to raise the refractive index and thereby induce a phase shift. Thermal post-processing may also be applied but neither of the post processing methods are especially applicable for multi phase shift gratings. In the moving fiber-scanning beam technique [2] the phase mask and optical fiber are moved relative to each other. A π phase shift is introduced in the grating by a movement corresponding to half the periodicity of the index modulation. This technique is highly flexible and can produce gratings of very high quality [64, 5]. Given the need for interferometric control of the relative position of phase mask and fiber, this technique is evidently very sensitive towards vibrations in the experimental setup.
We have developed the novel polarization control method [65, 7] for UV writing of advanced Bragg gratings with the possibility of including several phase shifts. The experimental realization of the method is to some extent similar to the conventional scanning beam technique, in which the UV beam is scanned

along the fixed optical fiber and phase mask. The method is flexible, requires only uniform phase masks and is significantly more stable towards vibrations in the experimental setup than the moving fiber-scanning beam technique. This chapter is devoted to the description of the polarization control method and the gratings written in optical fibers using this method. The principle of the polarization control method is described in Section 6.2, while Sections 6.3 to 6.5 present the apodization profiles realized during this study. Section 6.6 introduces the optics needed to upgrade the setup for the double-exposure technique to the polarization control method. Section 6.7 describes the characterization and optimization of the experimental setup. The results are presented in Section 6.8, a comparison with the competing methods is found in Section 6.9 and finally concluding remarks and a brief outlook are given in Section 6.10.

The polarization control method has so far only been used to write Bragg gratings in optical fibers. In the remainder of this chapter this is the only type of optical waveguide, which will be considered. The method is evidently also capable of writing advanced Bragg gratings in planar waveguides.

6.2 Principle

The principle of the polarization control method is illustrated in Figure 6.1. The method is based on a spatial separation of the two orthogonal polarizations states of a linearly polarized ultraviolet (UV) beam. A polarization beam splitter positioned just above the phase mask separates the two polarization states of the incident beam into two single-polarization-state beams with diverging propagation vectors. Both beams are diffracted at the phase mask and two separated interference patterns appear. The lateral separation of the patterns increases with the distance from the phase mask. At a given distance the separation corresponds to half the period of the interference pattern. When the core of an optical fiber is positioned at this distance, a π phase shift between the two UV induced refractive index modulation profiles is realized. During a scanning exposure, a π phase shift in the Bragg grating is introduced by changing the irradiance from one of the single-polarization-state beams to the other. This section describes in detail the principle of the polarization control method.

After passage through a pile-of-plates polarizer the UV beam is linearly polarized and may be described by a linear combination of two orthogonal linearly polarized waves [66]. In the polarization control method the linearly polarized beam is most conveniently expressed in terms of the s- and p-polarization states. The direction of the p-polarization field vector is parallel to the long axis of the fiber, while the s-polarization is perpendicular to both the direction of propagation and the fiber as illustrated in Figure 6.2. The irradiance in the two polarization states is given by Malus's law

$$I_p = I_0 \cos^2 \alpha \,, \qquad I_s = I_0 \sin^2 \alpha \tag{6.1}$$

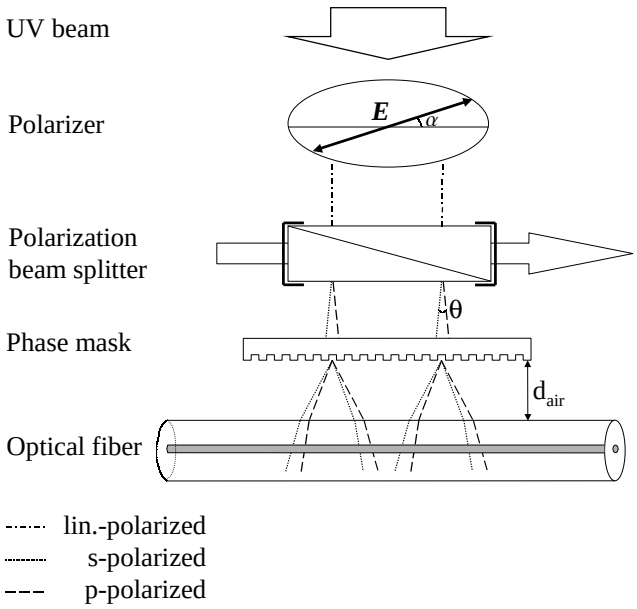

Figure 6.1: Schematic presentation of the principle of the polarization control method. Two phase shifted refractive index modulation profiles are generated in the fiber core by the diverging s- and p-polarized parts of the UV beam. The ratio of UV irradiance in the two polarizations and hence the relative strength of the modulation profiles is adjusted by a polarizer mounted on a computer controlled rotation stage.

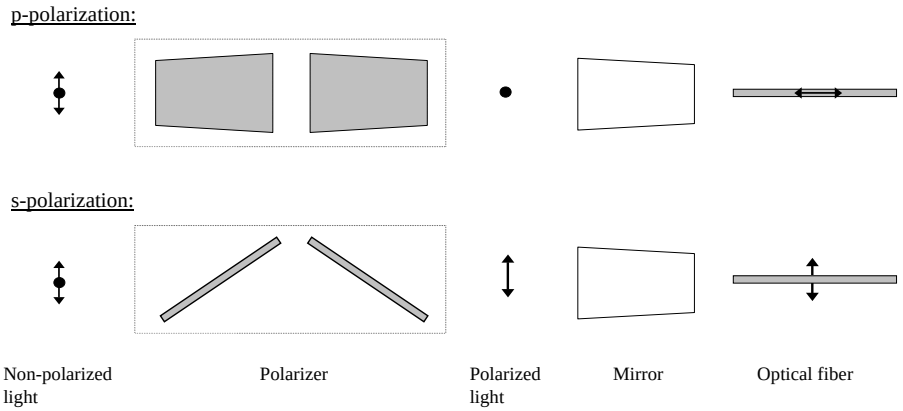

Figure 6.2: Propagation of the two polarizations through the optical setup. The non-polarized light emitted from the Excimer laser is polarized and guided towards the optical fiber by a mirror. The polarization beam splitter has been omitted for clarity. At the fiber the p-polarized light is aligned parallel to the fiber axis, while the s-polarization field vector is perpendicular to the axis.

where I_0 is the irradiance of the linearly polarized beam and α is the angle between the transmission axis of the polarizer and the field vector of the p-polarized beam. When emerging from the polarization beam splitter, the s- and p-polarizations still propagate in the plane of incidence. The deviation angle, θ, between the propagation vectors of the two beams equals the wedge angle of the beam splitter as seen in Figure 6.10. Both single-polarization-state beams are diffracted at the phase mask and interfere independently of each other to give two separated interference patterns below the mask. Given the different directions of the propagation vectors, the patterns are displaced by a distance, w, given by the deviation angle and the distance, d, from the phase mask. When exposing an optical fiber the difference in the refractive indices of silica and air must be considered when the distance is calculated. In the photosensitive core of the optical fiber, the irradiance modulation profiles write two refractive index modulation profiles. At a certain distance between the phase mask and the surface of the fiber, d_{air}, the lateral separation between the two refractive index modulation profiles corresponds to half a period. An expression for d_{air} is given in the following section relating it to the periodicity of the phase mask, the cladding thickness and refractive index and the deviation angle of the polarization beam splitter. Is should be mentioned that all Bragg gratings presented in this chapter were written with a fiber to phase mask distance corresponding to a π phase shift between the separated p- and s-polarization interference patterns.

6.2.1 Phase mask - fiber distance

The dominating 1^{st} and -1^{st} order diffracted beams emerge from the phase mask with an angle $\Psi_{\pm 1}$ given by

$$\sin \Psi_{\pm 1} = \pm \frac{\lambda_{\mathrm{UV}}}{\Lambda_{\mathrm{mask}}} + \sin \epsilon \tag{6.2}$$

where λ_{UV} is the wavelength of the UV source, Λ_{mask} the phase mask periodicity, and ϵ is the angle-of-incidence on the UV beam. Both single-polarization-state beams obey this law with the difference being the angle-of-incidence. The s-polarized light leaves the Wollaston prism at an angle $\epsilon_s = \epsilon = \theta/2$, where θ is the divergence angle of the polarization beam splitter. The angle of the p-polarized light relative to the normal of the beam splitter equals $\epsilon_p = -\epsilon$. The spatial separation between the two refractive index modulation profiles induced by the two single-polarization-state beams can be evaluated from the offset between their 1^{st} order diffracted beams. Given the small divergence angle, the approximation $\sin \epsilon \approx \epsilon$ is justified and the 1^{st} order diffraction angles for the s- and p-polarizations are

$$\sin \Psi_1^{s,\,\mathrm{air}} = \frac{\lambda_{\mathrm{UV}}}{\Lambda_{\mathrm{mask}}} + \epsilon \tag{6.3}$$

$$\sin \Psi_1^{p,\,\mathrm{air}} = \frac{\lambda_{\mathrm{UV}}}{\Lambda_{\mathrm{mask}}} - \epsilon \tag{6.4}$$

Using Snell's law and the small angle approximation $\sin \Psi_1 \approx \Psi_1$ the angle of the refracted light in the fiber cladding is given by

$$\Psi_1^{i,\,\mathrm{clad}} = \frac{\Psi_1^{i,\,\mathrm{air}}}{n_{\mathrm{silica}}} \qquad i = s, p \tag{6.5}$$

which is valid for both polarizations. Geometrical considerations can be used to determine the distance, w, between the lateral positions, where the 1^{st} order diffracted s- and p-polarized beams emerging from the same position on the phase mask intercept the fiber core. The distance can be expressed through the angles described above

$$\begin{aligned} w \;=\; & d_{\mathrm{air}} \left[\tan\left(\Psi_1^{s,\,\mathrm{air}}\right) - \tan\left(\Psi_1^{p,\,\mathrm{air}}\right) \right] \\ & + r_{\mathrm{fiber}} \left[\tan\left(\Psi_1^{s,\,\mathrm{clad}}\right) - \tan\left(\Psi_1^{p,\,\mathrm{clad}}\right) \right] \end{aligned} \tag{6.6}$$

where r_{fiber} is the radius of the fiber. In the limit of small ϵ, w can be expressed as [19]

$$w = d_{\mathrm{air}} \frac{2\epsilon}{(1-\tau^2)^{3/2}} + r_{\mathrm{fiber}} \frac{2\,\epsilon\, n_{\mathrm{silica}}^2}{(n_{\mathrm{silica}}^2 - \tau^2)^{3/2}} \tag{6.7}$$

where $\tau = \frac{\lambda_{\mathrm{UV}}}{\Lambda_{\mathrm{mask}}}$. This is the general expression for the offset between the refractive index modulation profiles induced in the optical fiber core. For a given fiber with fixed values of n_{silica} and r_{fiber}, the offset is controlled by adjusting the distance d_{air}. In the case where a π phase shift is requested, w is set to

$\Lambda_{\text{mask}}/4$ and the phase mask must be placed at a distance from the fiber given by

$$d_{\text{air}} = \frac{\Lambda_{\text{mask}}}{8\epsilon}\left(1-\tau^2\right)^{3/2} - \frac{r_{\text{fiber}}}{2\,n_{\text{silica}}^2}\frac{\left(1-\tau^2\right)^{3/2}}{\left[1-\left(\tau/n_{\text{silica}}\right)^2\right]^{3/2}} \tag{6.8}$$

In the approximation $\tau \ll 1$ this reduces to the pocket calculator friendly expression

$$d_{\text{air}} = \frac{\Lambda_{\text{mask}}}{8\epsilon} - \frac{r_{\text{fiber}}}{n_{\text{silica}}} \tag{6.9}$$

For the standard settings used in our experiments the parameters appearing in this expression have the following values $r_{\text{fiber}} = 62.5\,\mu\text{m}$, $\lambda_{\text{UV}} = 248\,\text{nm}$, $\Lambda_{\text{mask}} = 1069\,\text{nm}$, $\epsilon = 0.0012\,\text{rad}$, and $n_{\text{silica}} = 1.509$ is the refractive index of silica at 248 nm. Equation 6.9 then show that the distance should be in the order of $68\,\mu$m. This number is only a crude estimate of the correct distance, given that $\tau = 0.23$ and the uncertainty in the wedge angle of the polarization beam splitter. Furthermore does the analysis above not take into account the higher refractive index of the core by assuming a constant value of n_{silica} throughout the fiber.

6.2.2 Index modulation profile

It is henceforth assumed that the phase mask is placed at the distance from the fiber giving a phase shift of π between the interference patterns of the two single-polarization-state beams. By using the refractive index modulation profile induced by the p-polarized beam as reference, the irradiance profiles, $I_p^{\text{intf}}(z)$ and $I_s^{\text{intf}}(z)$ can be expressed as

$$I_p^{\text{intf}}(z) = 2I_p\left[1+\cos\left(\frac{2\pi}{\Lambda_{\text{mod}}}z+\varphi_0\right)\right] \tag{6.10}$$

$$I_s^{\text{intf}}(z) = 2I_s\left[1+\cos\left(\frac{2\pi}{\Lambda_{\text{mod}}}z+\varphi_0+\pi\right)\right] \tag{6.11}$$

where φ_0 is a constant phase and $\Lambda_{\text{mod}} = \Lambda_{\text{mask}}/2$ is the periodicity of the refractive index modulation profile. The accumulated fluence, F, equals the irradiance, I, multiplied by the exposure time t. With the irradiance of the two polarizations given by Malus's law (Equation 6.1) the total fluence profile, $F(z) = F_p(z) + F_s(z)$, at the fiber core equals

$$\begin{aligned} F(z) &= F_0\left\{\cos^2\alpha\left[1+\cos\left(\frac{2\pi}{\Lambda_{\text{mod}}}z+\varphi_0\right)\right]\right. \\ &+ \left.\sin^2\alpha\left[1+\cos\left(\frac{2\pi}{\Lambda_{\text{mod}}}z+\varphi_0+\pi\right)\right]\right\} \end{aligned} \tag{6.12}$$

where $F_0 = I_0\,t$. This expression can immediately be reduced to

$$F(z) = F_0\left[1+\cos(2\alpha)\cdot\cos\left(\frac{2\pi}{\Lambda_{\text{mod}}}z+\varphi_0\right)\right] \tag{6.13}$$

As a result of the photosensitivity of the optical fiber core this fluence profile will introduce a refractive index profile with same periodicity Λ_{mod}. The

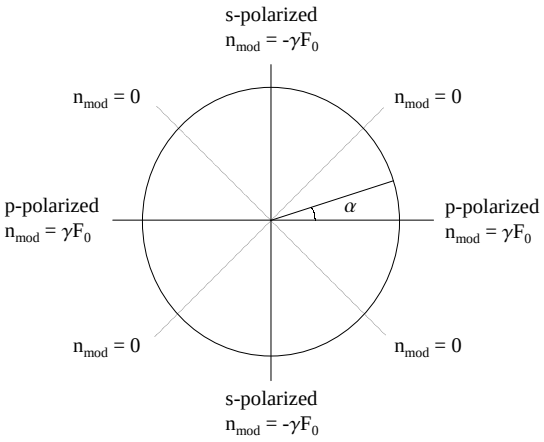

Figure 6.3: The polarization of the linearly polarized UV beam and the magnitude of n_{mod} at different polarizer angles. The dotted lines with $n_{\mathrm{mod}} = 0$ mark the cross-over angles, where a phase shift is introduced.

UV induced changes are related to the accumulated fluence through the photosensitivity parameter, γ, which can have a complex dependence on both the accumulated fluence, the pulse wavelength and fluence, and several fiber related parameters such as germanium concentration and fabrication history [22]. When γ depends on the accumulated fluence, this dependence must be included in the grating design in order to obtain high quality gratings. For the moment it is assumed to be constant, $\gamma(F) = \gamma$, which is an excellent approximation in large fluence ranges of the deuterium loaded fibers used in this study as illustrated in Figures 6.17 and 6.18. With a linear photosensitivity curve (constant γ) the UV induced refractive index change is given by

$$\Delta n(z) = \Delta n_{\mathrm{avg}}(z) + n_{\mathrm{mod}}(z) \cdot \cos\left(\frac{2\pi}{\Lambda_{\mathrm{mod}}} z + \varphi_0\right) \tag{6.14}$$

where $\Delta n_{\mathrm{avg}}(z) = \gamma F_0$ is the average refractive index change and $n_{\mathrm{mod}}(z)$ is the refractive index modulation amplitude. The variation of $\Delta n_{\mathrm{avg}}(z)$ along the optical fiber is included only to emphasize the flexibility of the polarization control method. So far only chirp-free gratings with a constant total fluence throughout the grating have been written. The z-dependence of the refractive index modulation amplitude is related to the polarizer angle, α, through

$$n_{\mathrm{mod}}(z) = \gamma F_0 \cos(2\alpha) \tag{6.15}$$

This equation shows that it is possible to control the amplitude of the refractive index modulation profile as well as the phase by changing the polarizer angle. When α equals either $2k \cdot 90°$ or $(2k-1) \cdot 90°$, where k is an integer, the index modulation reaches its maximum value. These situations correspond to pure p- or s-polarization of the UV beam, respectively, as indicated in Figure 6.3. In between these polarizer angles the modulation amplitude gradually decreases as the angle approaches $(k - \frac{1}{2}) \cdot 90°$, which corresponds to a situation with equal

irradiation in the two single-polarization-state beams. The two out-of-phase refractive index modulation profiles then add to give zero total modulation amplitude. The negative values of n_{mod} in certain polarizer angle intervals corresponds to a phase shifted modulation profile as described in Section 4.4.3. A phase shift is introduced in the Bragg grating by crossing one of the $(k-\frac{1}{2})\cdot 90°$ angles, which are marked by dotted lines in Figure 6.3. By rotating the polarizer during a scan along the fiber, advanced refractive index modulation profiles can evidently be induced, while keeping the effective refractive index constant. The polarization control method can hence write apodized gratings in a single scan. This is an improvement relative to the double-exposure technique, which requires a second scan to raise the effective refractive index to a constant level throughput the grating. In the following text the description is limited to the $-90°$ to $90°$ window. This simplifies the analysis without reducing the validity of the results due to the intrinsic symmetry of the system.
In the initial stage of the implementation of the polarization control method, priority was given to two apodization profiles. The fairly simple Gaussian profile in which no phase shifts are present, and the sinc-grating including several phase shifts. Once the method was developed to a satisfactory level more advanced profiles such as dispersion reduced gratings were designed using commercial software and realized using the method. Given the expression for the modulation amplitude seen in Equation 6.15, the polarizer angle profile for any desired modulation profile can be calculated using

$$\alpha(z) = 0.5 \arccos\left(\frac{n_{\mathrm{mod}}}{\gamma F_0}\right) \tag{6.16}$$

The Gaussian, the sinc and the asymmetric sinc-like dispersion reduced gratings are treated in individual sections starting with the Gaussian gratings.

6.3 Gaussian gratings

In a Gaussian grating the refractive index modulation amplitude takes the form

$$n_{\mathrm{mod}}(z) = n_0 \exp\left[-\ln(2)\left(\frac{2(z-L/2)}{s_{\mathrm{gauss}}L}\right)^2\right] \tag{6.17}$$

where n_0 is the maximum index modulation, s_{gauss} is the taper parameter, and L is the grating length. The refractive index modulation amplitude has its maximum value in the center of the grating, while it smoothly decrease away from the center with a symmetric dependence on the distance from the center as seen in Figure 6.4(a). This figure shows the normalized modulation amplitude n_{mod}/n_0 of a 23 mm long Gaussian grating with a taper parameter of $s_{\mathrm{gauss}} = 0.3$. The Gaussian profile is realized by suppressing one of the polarizations completely in the center, while gradually changing towards having nearly equal fluence in the two single-polarization-state beams at the edges of the grating. The polarizer angle used to write the Gaussian grating described above is seen in Figure 6.4(b), while the corresponding fluence profiles for the two polarizations are depicted in Figure 6.4(a).

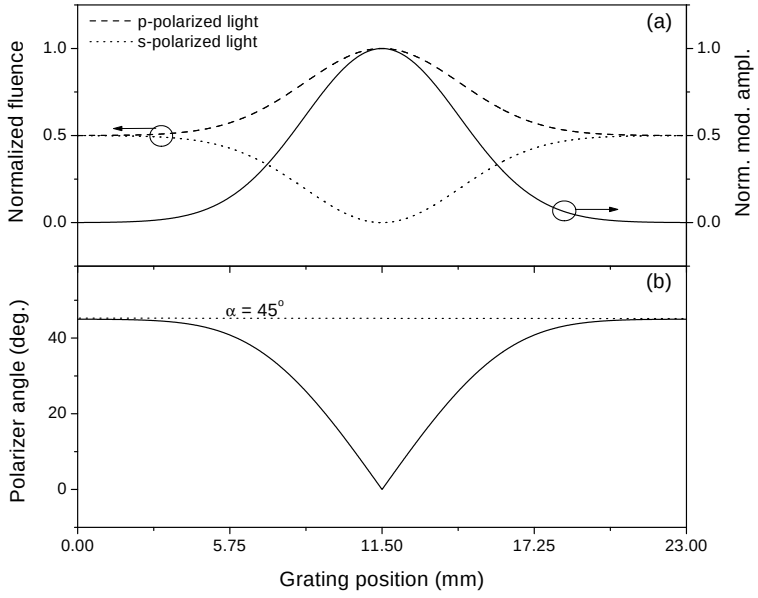

Figure 6.4: Gaussian grating with refractive index modulation profile described by Equation 6.17. (a) shows the modulation profile and the distribution of the irradiance between the two polarizations along the grating, while (b) shows the polarizer angle profile required to realize the grating.

6.4 Sinc gratings

When the polarizer crosses either the $-45°$ or the $45°$ angle there is a change in the dominant polarization of the UV light and a phase shift is realized. This feature is the cornerstone of the polarization control method. The possibility to induce a phase shift in the grating is the major advantage when compared with for instance the double-exposure technique. It facilitates the inscription of gratings with a sinc apodization, which is required in order to write gratings with a square reflection peak (Section 4.4.3). The sinc grating apodization profile is described by the following expression

$$n_{\mathrm{mod}}(z) = n_0 \,\mathrm{sinc}\left(\frac{2\pi(z - L/2)}{s_{\mathrm{sinc}} L}\right) \tag{6.18}$$

where $\mathrm{sinc}(x) = \sin(x)/x$ and s_{sinc} is the taper parameter, which describes the width of the center peak and the periodicity of the phase shifts. In a pure sinc grating the index modulation profile still has a significant magnitude at the edges of the grating. Truncating the grating abruptly will result in a ripple in the reflection spectrum and hence a poor side lobe suppression. This is the so-called Gibbs phenomena [53]. In order to improve the side lobe suppression an additional Gaussian apodization of the sinc grating is applied. This tapering of the modulation amplitude reduces the steepness of the sides of the reflection peak but the side lobe suppression is increased significantly. The full expression

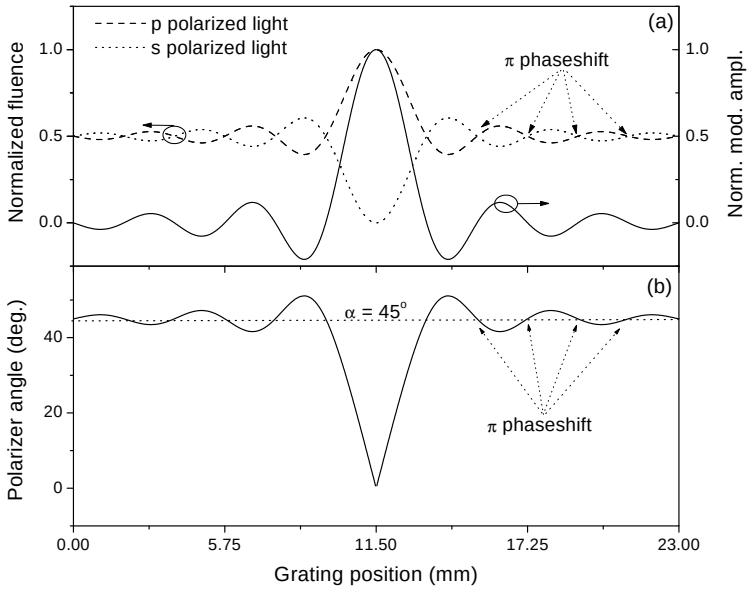

Figure 6.5: Sinc grating with refractive index modulation profile described by Equation 6.19 using $s_{\text{sinc}} = 1/6$, and $\sigma_{\text{Gauss}} = 7$. (a) shows the modulation profile and the distribution of the irradiance between the two polarizations along the grating, while (b) shows the polarizer angle profile required to realize the grating.

for the symmetric sinc gratings fabricated during this study is then given by

$$n_{\text{mod}}(z) = n_0 \,\text{sinc}\left(\frac{2\pi(z - L/2)}{s_{\text{sinc}} L}\right) \cdot \exp\left[-\ln(2)\left(\frac{2(z - L/2)}{\sigma_{\text{Gauss}} \cdot s_{\text{sinc}} L}\right)^2\right] \qquad (6.19)$$

where $\sigma_{\text{Gauss}} = s_{\text{gauss}}/s_{\text{sinc}}$ is the ratio between the taper parameters for the sinc grating and the additional Gaussian apodization. An example of a sinc grating profile is seen in Figure 6.5. A negative refractive index modulation amplitude corresponds to a phase shifted modulation profile as mentioned earlier in this chapter.

6.5 Asymmetric gratings

The prediction of the amplitude response from a Bragg grating using the Fourier transform of the index modulation profile is only strictly valid for non-depleted pulses. In strong gratings the reflection depletes the incident pulse and the Fourier analysis is no longer valid. Inverse scattering techniques exist [3, 4], which can design the refractive index modulation amplitude profile required in order to obtain a specified amplitude and phase response. Very strong dispersion reduced gratings with transmission-loss up to 80 dB have been realized by implementing designs [67] calculated using the commercial software IFO Gratings [68]. In the recent years the dispersion properties of Bragg gratings have achieved an increasing interest [69, 70, 6]. The symmetric sinc grating has a

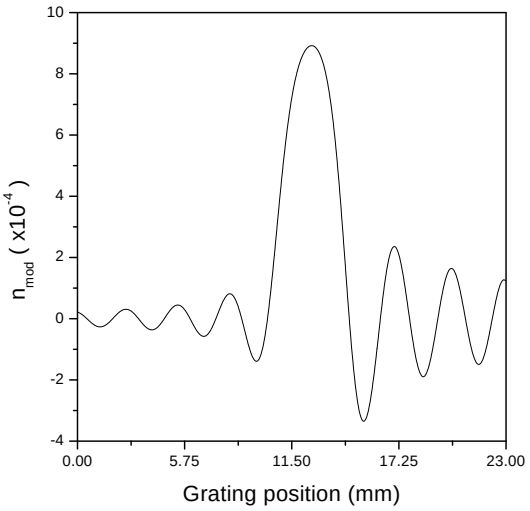

Figure 6.6: Refractive index modulation profile of dispersion reduced asymmetric grating. The incident pulse is assumed to enter the grating from the left hand side. Designed using the commercial software IFO Gratings 4.0 [68].

fairly high dispersion thus leading to a poor performance in optical communication systems. Dispersion reduced gratings were designed by requiring a linear phase in and outside the stop band, i.e. a constant group delay. The calculated index modulation amplitude profiles typically have the characteristics seen in Figure 6.6, where the signal pulse is assumed to enter the grating from the left hand side. The center peak is slightly asymmetric and shifted towards the far end of the grating. Furthermore the phase shifts after the center peak have a different periodicity that those before. The improved dispersion properties of a designed grating relative to a symmetric sinc grating is illustrated in Figure 6.7. This figure shows that the group delay ripple in the center of the stop band is reduced significantly in the designed grating compared to that seen in the symmetric sinc grating. Only at the edges, where the reflection of the grating drops quickly, the delay oscillates rapidly. Figures 6.7(a) and 6.7(b) furthermore illustrate that the Gibbs phenomena both influence the amplitude and the phase of the reflected signal causing ripples in the reflection and group delay. By tapering the index modulation profile with a Gaussian apodization these ripples are reduced significantly. When using a strong tapering, with a vanishing refractive index modulation profile at the edges of the grating, we obtain an excellent suppression of the side lobes and the group delay ripple as seen in Figure 6.7(c). The improved dispersion properties and side lobe suppression are at the expense of a slightly reduced steepness of the reflection peak. By careful design of the grating a high steepness and a large side lobe suppression can be achieved. The deviation from the perfect square filter response is only in worst cases comparable to what is obtained in gratings with simple apodizations profiles.

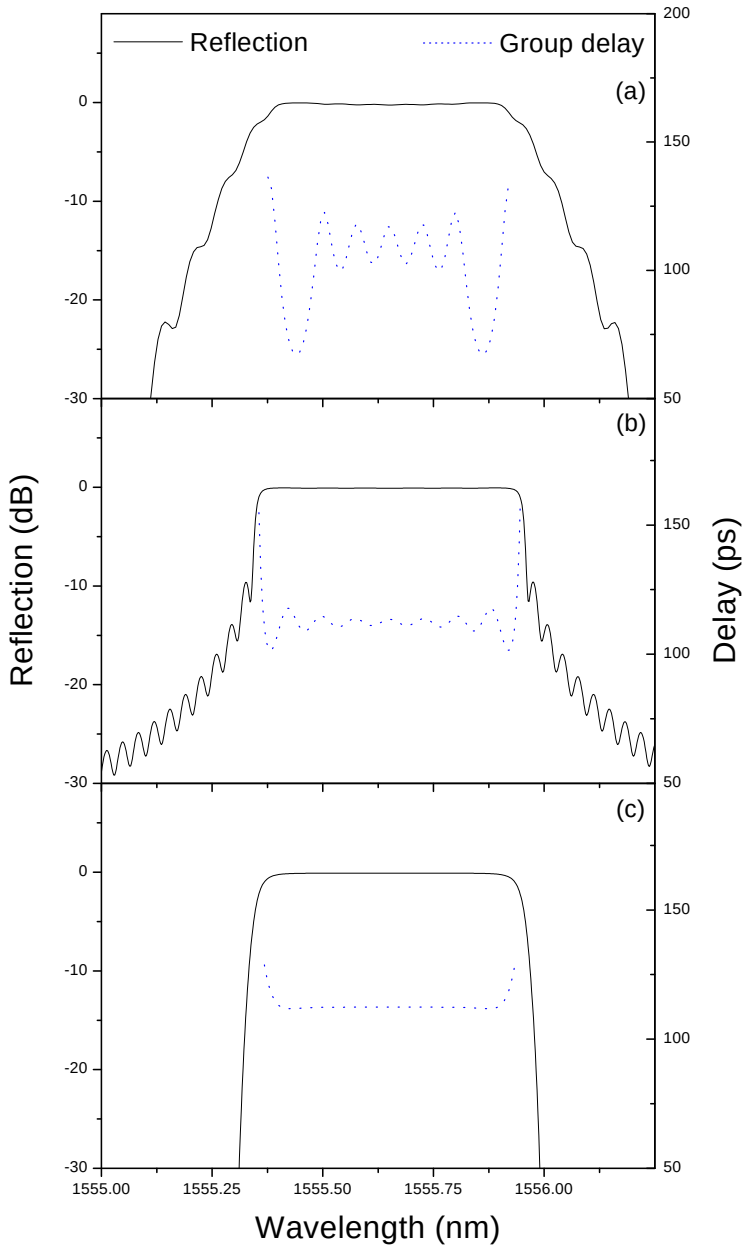

Figure 6.7: Simulated reflection and group delay of (a) a symmetric sinc grating and (b) an asymmetric dispersion reduced grating using the modulation profiles presented in Figures 6.5 and 6.6. (c) shows the simulated response from a grating with a Gaussian tapering of the asymmetric modulation profile of the grating presented in (b). All gratings were designed to have a transmission loss at the center wavelength of 16 dB.

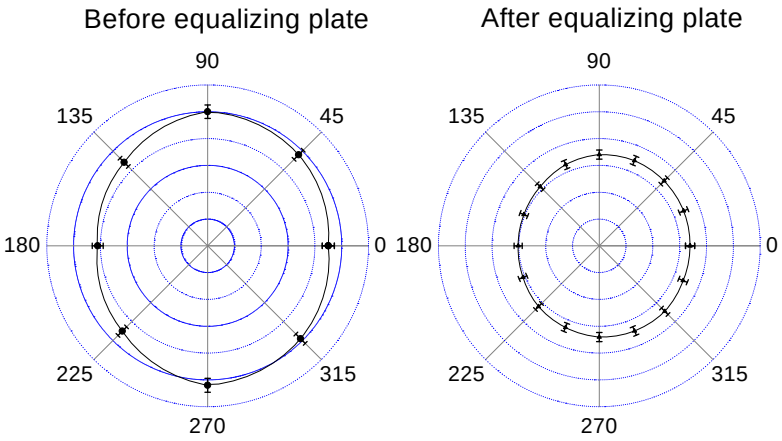

Figure 6.8: The irradiance distribution in the excimer laser beam before (left hand side) and after equalization (right hand side) by passing the beam through a silica plate, which is placed under an angle close to the Brewster angle thereby reducing primarily the irradiance of the s-polarized light.

6.6 Experimental setup

As mentioned in the introduction of this chapter the experimental setup used to implement the polarization control method is a modification of the setup used for the double-exposure technique. This section describes the new optics and equipment included in the setup in order to implement the polarization control method.

An excimer laser beam emits light in several polarization states. Due to the geometry of the discharge volume, where the light is generated, it furthermore has a preferential axis in the vertical plane. The energy distribution of the linearly polarized light emerging from the polarizer is hence asymmetric as can be seen in the left hand side of Figure 6.8. The asymmetry can be reduced significantly by inserting a silica plate in the beam path at an angle, which is adjusted to give an uniform distribution. As the right hand side of Figure 6.8 shows, it is possible to reduce the asymmetry to a level below 2% of the irradiance in a polarizer angle interval from $-90°$ to $90°$. This interval covers the range of polarizer angles used during a grating inscription and no effort was made to ensure a uniform distribution throughout the full range.

6.6.1 Polarizer

The polarizer design is based on the pile-of-plates principle [66] using two quartz plates. One is placed at the Brewster angle, θ_p, the other at $90° - \theta_\mathrm{p}$ as seen in Figure 6.9. This non-parallel alignment of the plates was chosen in order to avoid any movement of the beam as the polarizer is rotated. Tests using a linearly polarized frequency doubled argon ion laser operating at 244 nm showed no measurable transmission of the polarization state normal to the plane of incidence. The efficiency of the polarizer may be improved slightly by adding

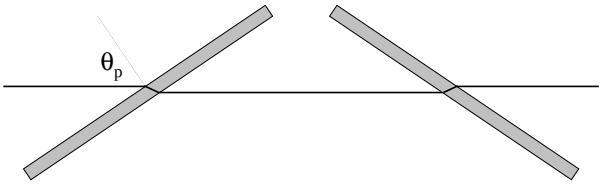

Figure 6.9: The pile-of-plates polarizer used in the experiments. The thin line marks the normal to the plate, while the thick line indicate the beam path through the polarizer. The Brewster angle, θ_p, is approximately 56° for a silica plate in air. The plates are coated to enhance the polarization effect to approximately 95% per plate.

more sets of plates, but based on our measurements we concluded that this was not necessary. Any residual light in the suppressed polarization will furthermore only result in a constant floor in the grating assuming no polarization dependence of the polarizer efficiency. By rotating the plates around the axis of propagation of the incident beam, the polarizer can be set to transmit either the *s*- or the *p*-polarized beams only or light with a distribution of the two polarizations. The ratio between the irradiance in the two single-polarization-state beams is determined by the angle, α, between the plane-of-incidence and the electric field vector of the *p*-polarization beam. A holder for the plates was designed and mounted in a computer controlled rotation stage.

6.6.2 Polarization beam splitter

The polarization beam splitter used in our experiment was a custom made Wollaston prism with a wedge angle, θ, of approximately 0.14°. This polarizer transmits both polarizations but introduces an angle equal to the wedge angle between the propagation vectors of the *s*- and *p*-polarizations of the UV beam as seen in Figure 6.10. The polarization beam splitter was positioned just above the phase mask in order to ensure a large overlap of the two independent refractive index modulation profiles generated by the two single-polarization-beams.

6.6.3 Phase mask holder

In order to have accurate control of the distance between the phase mask and the fiber core a holder for the phase mask was constructed. This holder enables manual correction of the distance between the phase mask and optical fiber as well as any longitudinal and vertical angle between the two. Especially the former is of crucial importance as the following pages will show. The image from an optical microscope mounted on the side of the setup was displayed on a monitor thus allowing for a very precise alignment of the fiber to phase mask distance. The only place in our setup where vibrations come into play are at the

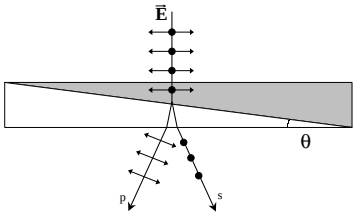

Figure 6.10: The Wollaston prism polarization beam splitter separating the s- and p-polarizations of the linearly polarized incident **E**-field. In our setup the wedge angle is approximate equal to $\theta = 0.14°$. This is also the angle between the two single-polarization-state beams emerging from the prism.

phase mask holder. Initially a more complex holder with more functionalities was designed, but this was sensitive towards vibrations and a simpler version was used instead. With the modifications made, vibrations are no longer a problem.

6.7 Characterization and optimization

Several components in the optical setup need careful optimization in order to write high quality gratings with the polarization control method. Poor alignment of the polarizer relative to the beam path decreases its efficiency and introduces an angle-dependent offset in the beam position. Especially the latter has proven to be detrimental for the method. The vertical alignment of the polarization beam splitter relative to the phase mask also needs to be precise in order to have an equal periodicity of the index modulation profiles induced by the s- and p- polarizations of the UV beam. Both the polarizer and polarization beam splitter angles relative to the beam path were aligned by visual inspection. The delicate alignment of the polarizer reference angle with respect to the optical fiber and the phase mask to fiber distance are discussed below in individual sections. Furthermore the induced change in the refractive index modulation must have a linear dependence on the accumulated fluence and be independent of the polarization of the UV light unless advanced compensation schemes are implemented. The characterization of the dependence of accumulated fluence and UV polarization are described in Sections 6.7.3 and 6.7.4.

6.7.1 Phase-mask to fiber distance

Thorough optimization of the fiber to phase mask distance is necessary in order to obtain high quality gratings. The adjustment of the distance was performed by writing weak sinc-gratings in test fibers. The spectral response is then compared with simulations to estimate the error in the distance. With some experience it is possible to evaluate the error by direct comparison with earlier test series. A fresh fiber is mounted and the distance is adjusted before the new test grating is written. A series of test exposures made on a deuterium-free

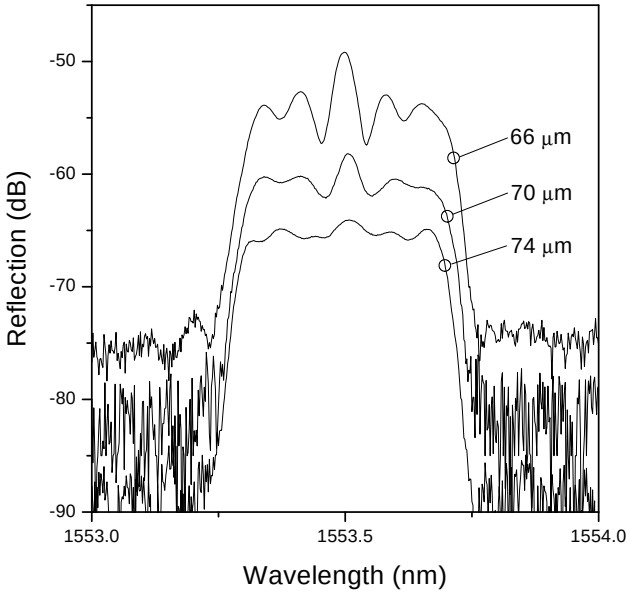

Figure 6.11: A series of test sinc gratings written in deuterium-free high germanium content fiber at different phase-mask to fiber distances. The gratings are offset for clarity.

high germanium content fiber is presented in Figure 6.11. The experiments and simulations show that careful adjustment of the phase mask to fiber distance is essential in order to obtain high quality gratings. The observed tolerance of $\pm 1\,\mu$m in the adjustment of d_{air} is set by the deviation angle between the two single-polarization-state beams. By using a smaller angle a higher tolerance can be achieved. The downside is that the limited coherence of the excimer laser eventually will become a problem when d_{air} approaches $500\,\mu$m as described in Section 5.4.1. By using high coherence UV sources such as the cw lasers described in Section 5.2.2 the maximum distance and thus the tolerance can be increased considerably.

6.7.2 Polarizer alignment

Test gratings were written using polarizer angles in the range from 0° to 55°. When operating in this range only, a positive offset in the polarizer reference angle results in a dip at the center wavelength of the reflection peak, while a peak occurs when the offset is negative as seen in Figure 6.12. In a sinc grating written using polarizer angles between 0° to 55° only, a negative offset in the polarizer angle will result in a small dip in the modulation amplitude profile in the center part of the sinc grating. When using an excimer beam with a beam length of 0.7 mm this dip is effectively smeared out and has no major significance. More importantly a negative offset will lead to an upward displacement of the refractive index modulation profile relative to the phase-shift line, while a positive offset results in a downward displacement. This is illustrated in Figure 6.13, which shows the normalized refractive index modulation

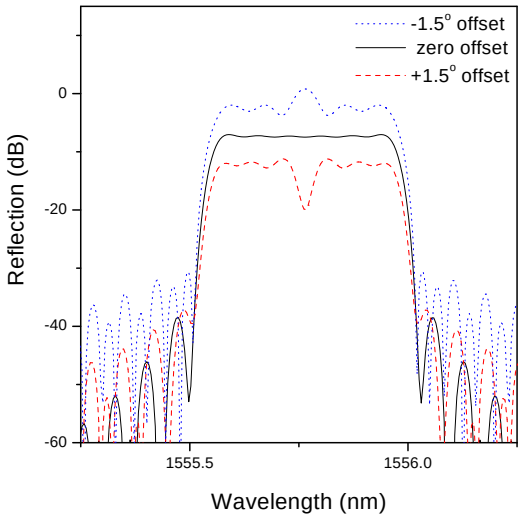

Figure 6.12: Simulated reflection peaks when the polarizer angle is offset by $\pm 1.5°$ compared with the zero offset reflection. The polarizer angle is in the range from 0° to 55° during the inscription.

profiles for two sinc gratings shifted by $\pm 1.5°$ relative to the correct polarizer angle. In both cases several phase shifts are missing and the position of those still present are no longer periodic. The alternate side bands on the modulation profile are hence either strengthened or reduced. For a negative offset the odd side bands are suppressed, while the even side bands increase in strength and length and *vise versa* for a positive offset. It is believed that the deviations in the side bands from the sinc profile are the dominant factor leading to the changes seen in the center of the reflection peak. Regardless of the mechanism responsible for the observed changes they provide a highly sensitive measure of the quality of the polarizer reference angle alignment. The initial rough alignment of the polarizer angle was made by visual inspection. For a more refined adjustment the same procedure as used to optimize the phase mask to fiber distance is performed with changing offsets on the polarizer angle. An example of the change in the reflection spectrum at different polarizer angle reference points is seen in Figure 6.14. This figure quite clearly shows the change in the center of the reflection peak as the polarizer angle reference point is changed from $-1.0°$ to $0.8°$. The initial peak found at negative offsets disappear and a dip emerge when positive offsets are used.

The changes in the reflection spectra are hence quite similar when adjusting the phase mask to fiber distance or the polarizer offset. Often both the phase-mask to fiber distance and offset need to be adjusted. Utilizing that only an offset in polarizer angle can give a dip in the reflection spectrum, the phase mask to fiber distance can be adjusted initially. Once this is done, the polarizer angle offset can be corrected. The alignment procedure is to some extent straightforward but care should be taken not to optimize at a "local minimum"

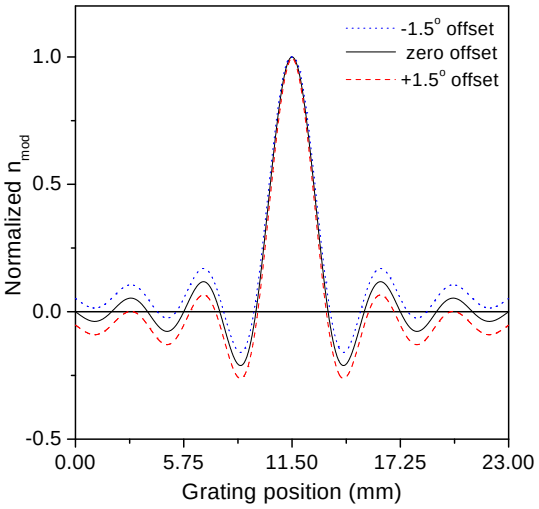

Figure 6.13: Normalized refractive index modulation amplitude profiles obtained with a polarizer angle offset of ±1.5° compared with the zero offset result. It is assumed that the polarizer angle is in the range from 0° to 55° during inscription.

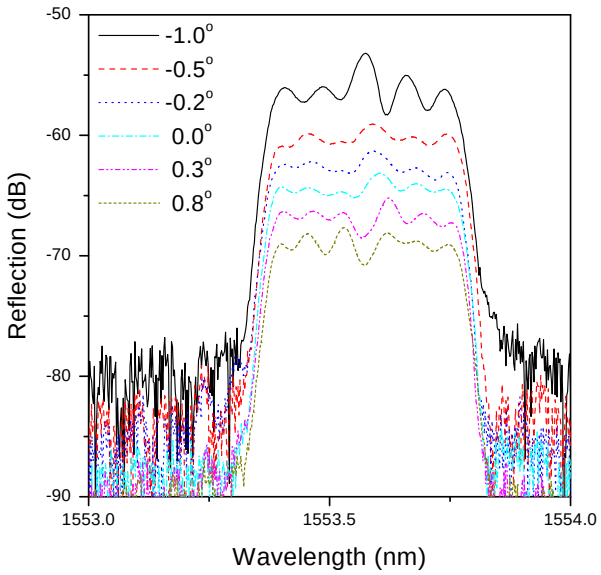

Figure 6.14: A series of test sinc gratings written in deuterium-free high germanium content fiber at different polarizer angle offsets. The gratings are offset for clarity.

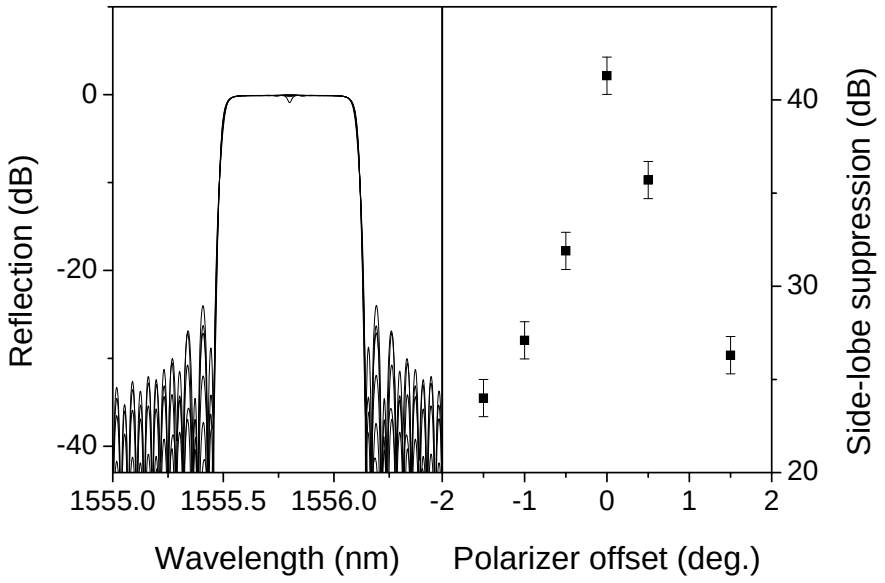

Figure 6.15: Simulations showing the effect of an offset in the polarizer angle. The side-lobe suppression is reduced by more than 10 dB if the angle is offset by 1°.

combination in the phase mask to fiber distance and polarizer angle offset parameter space. Such an adjustment will enable the writing of medium to high quality gratings but very high quality gratings require adjustment to near the global optimum.

The accuracy of the polarizer alignment determines the side-lobe suppression of the grating as exemplified by the simulations presented in Figure 6.15. This grating was designed to give a 40 dB suppression, which at an angle offset of $\pm 1^{o}$ is reduced to below 30 dB. From these simulations it is furthermore evident that the slope of the roll-off is not significantly affected by the error in the alignment. The phase properties of the grating are also influenced by the offset in the polarizer angle as seen in Figure 6.16, which shows the simulated group delay of the grating described above. Clearly the changes caused by the angle offset are significant and a careful alignment is required.

6.7.3 Fluence dependence

Two different optical fibers both supplied by Lucent Technologies Denmark[1] were used in the implementation of the polarization control method. The experimental HNLF fiber has a high germanium content thus making it photosensitive even without deuterium loading, while the commercially available TrueWave (TW) fiber on the other hand needs sensitization in order to show a significant photosensitivity. Unloaded HNLF fiber was used in several of the

[1]Now OFS Fitel

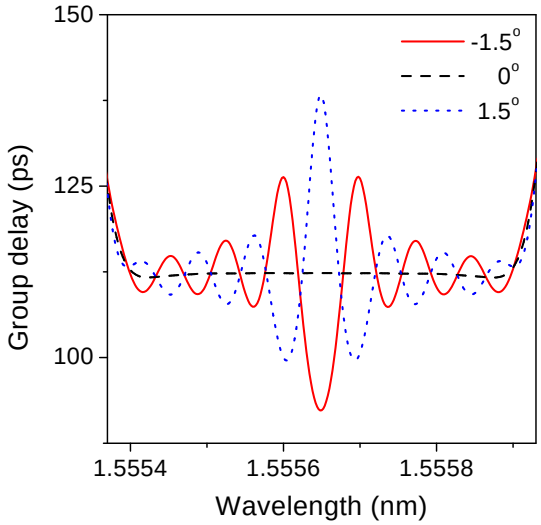

Figure 6.16: Simulations showing the group delay of the grating presented in Figure 6.15. The ripple introduced by a $\pm 1.5^{o}$ polarizer angle offset is evidently detrimental for the performance of the grating.

alignment exposures. It has a highly nonlinear photosensitivity preventing the inscription of very high quality gratings in this fiber. For alignment purposes the non-linearity was not a problem and it was chosen due to its fairly high photosensitivity without deuterium loading thus allowing pigtail splicing without prior heat treatment of the fiber ends. It should be noted that for a precise optimization of the fiber to phase mask distance the test exposures should be performed on a fiber similar to the one used for the actual grating. Deuterium loading changes the refractive index of the cladding and hence the optimum distance.
The nonlinearity is still present when the HNLF fiber is deuterium loaded but after an exposure of $50\,\mathrm{J/cm^2}$, the change in the refractive index modulation amplitude is linear as seen in Figure 6.17. Prior to the grating inscription the HNLF fibers were raised into the linear regime by a blanket pre-exposure of $60\,\mathrm{J/cm^2}$ without the polarization optics. Large index changes are evidently attainable in deuterium loaded HNLF fiber even at relatively low accumulated fluences. It is thus very suitable for the polarization control method, where a narrow UV beam is required in order to resolve the rapidly varying index modulation profile.
The deuterium loaded TrueWave fiber does not have as high photosensitivity as the HNLF fiber but it is linear from $\approx 50\,\mathrm{J/cm^2}$ and up. The growth curve for a 100 bar deuterium loaded TW fiber is shown in Figure 6.18

6.7.4 Polarization dependence

The polarization dependence of the UV induced changes in the refractive index of the optical fibers must be small in order to obtain a good performance of the polarization control method. If one of the polarizations of the UV beam

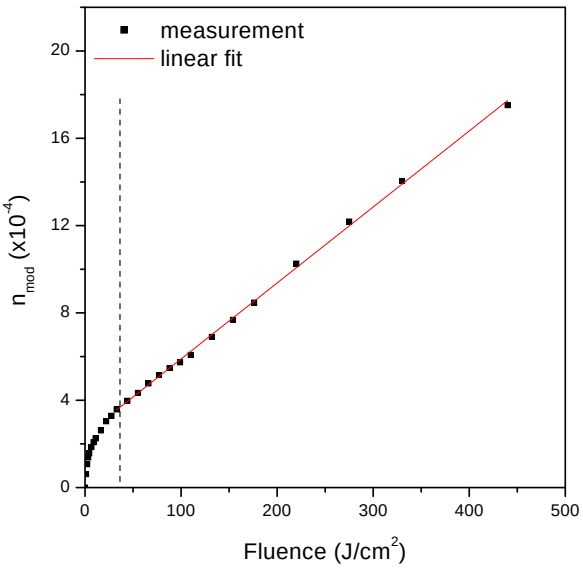

Figure 6.17: The growth of the refractive index modulation amplitude in a 100 bar deuterium loaded HNLF fiber supplied by Lucent Technologies Denmark. After an initial highly nonlinear regime, the growth is linear in the remaining fluence interval of interest.

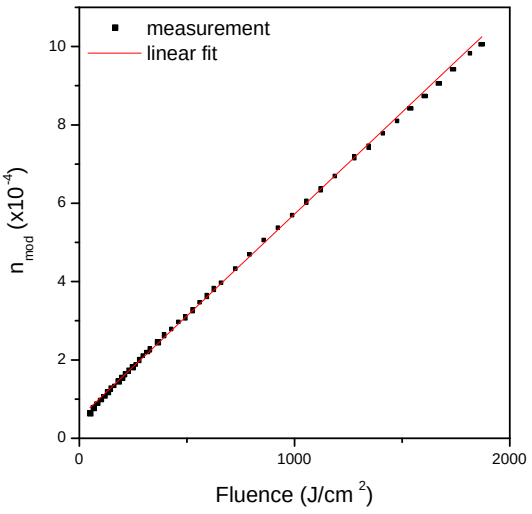

Figure 6.18: The growth of the refractive index modulation amplitude in a 100 bar deuterium loaded TrueWave fiber supplied by Lucent Technologies Denmark.

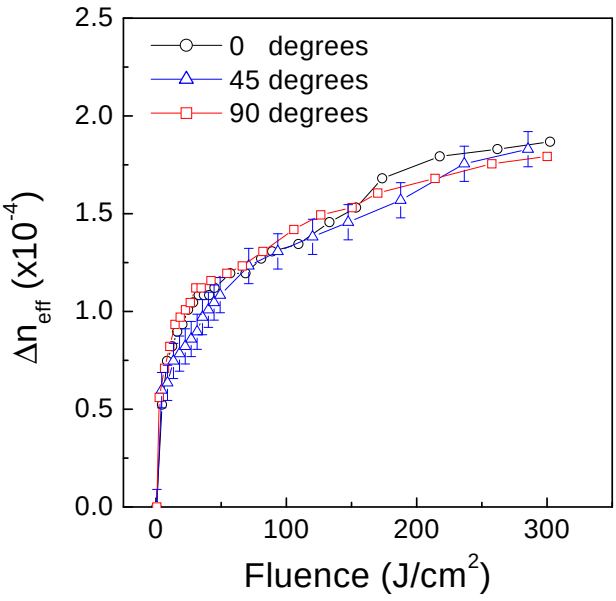

Figure 6.19: The polarization dependence of the induced refractive index change in a non-sensitized high germanium content optical fiber. Errorbars are not included on the 0° and 90° for clarity.

introduce a larger index change than the other, the index modulation profile is distorted and the phase shifts are displaced. Compensation can in principle be made by a small offset and tilt in the polarizer angle given by a linear transformation of α. This procedure requires detailed knowledge of the relationship between the refractive index change and the accumulated fluence for both polarizations. Measurements on a non-sensitized high germanium content fiber, show no measurable difference in photosensitivity when using s- or p-polarized light or a mixture as seen in Figure 6.19
We assume that the situation is the same for loaded fibers and that the photosensitivity is independent of the polarization of the UV beam.

UV induced birefringence

Several authors have reported UV induced birefringence depending on the polarization of the UV beam [71, 72]. The effect has been related to preferential defect bleaching and excitation by Poirier *et al.* [73]. The relatively large birefringence experienced after grating inscription using s-polarized light can be reduced by subsequent low fluence post-exposure with p-polarized light [74]. The reversal of the birefringence supports the model explaining the observed anisotropy by dipole alignment. High fluence is required to generate the defects responsible for the change in the refractive index, while a significantly lower dose is needed to align the exiting dipoles to the post-exposure UV field.
Post-exposure was not applied to remove birefringence in any of the polarization control method written Bragg gratings presented in this thesis. Given the quality of the gratings we concluded, that the effect of birefringence was not

detrimental to the gratings. At the level, to which the method has been developed today, birefringence may become an important factor and birefringence measurements and post-exposure test on the deuterium loaded optical fibers used in this study have been made [75]. These tests show that the fibers indeed are slightly birefringent and that a week p-polarized post-exposure reduces this to below the measurable level in good accordance with Erdogan *et al.* [72] and Meyer *et al.* [74].

6.8 Results

The presentation of the results obtained when using the polarization control method is divided into three sections describing the Gaussian, the symmetric sinc, and the dispersion reduced asymmetric gratings, respectively.

6.8.1 Gaussian gratings

Several Gaussian gratings were written especially in the early stages of the development of the polarization control method. Since no phase shifts are present in Gaussian gratings, these are less sensitive towards poor alignment of the phase mask to fiber distance and the polarizer angle reference point. The fabrication of Gaussian gratings still illustrate one of the advantages of the polarization method, which is the ability to write apodized gratings with constant effective refractive index in a single scan. A typical Gaussian profile used in this study is presented in Figure 6.4. The transmission and reflection spectra of a grating with this profile are displayed in Figure 6.20, which shows a 26 dB grating written in a deuterium loaded TrueWave fiber. The quality of this particular grating is representative for the gratings written in the beginning of the implementation of the model. Raised Gaussian gratings with excellent accordance between simulations and measured spectra are now produced routinely [76]. Once it was realized that the potential of the polarization control method most efficiently was tested by writing sinc gratings the focus was turned towards these gratings.

6.8.2 Sinc gratings

Sinc gratings are very sensitive to the alignment of the optical components allowing only small deviations in the phase mask to fiber distance and polarizer angle offset as described in Sections 6.7.1 and 6.7.2. Using this sensitivity to our advantage the optical setup was thoroughly aligned before the actual gratings were written. Both weak, medium strength, and strong sinc gratings were written in deuterium loaded TrueWave and HNLF fibers. The deuterium loaded TrueWave fiber was the favorite choice for the medium strength gratings, while the strong gratings usually were fabricated in the more sensitive deuterium loaded HNLF fiber. A high photosensitivity is required to keep the exposure time at a reasonable level. In order to resolve the detailed structure of the grating profile the beam width is reduced to 0.7 mm. Since the maximum allowed irradiance of the UV beam is limited by the damage threshold of the polarization beam splitter a pulse fluence of approximately $100\,\mathrm{mJ/cm^2}$ was

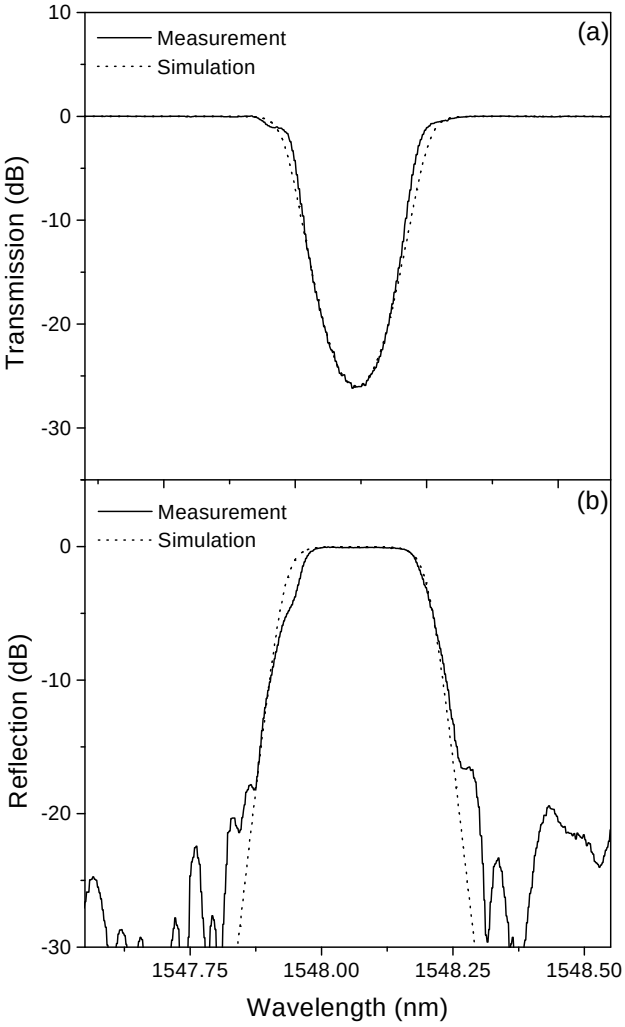

Figure 6.20: Transmission and reflection data for a 23 mm long raised Gaussian grating written in a deuterium loaded TrueWave fiber. The refractive index modulation amplitude and the polarizer angle profiles are seen in Figure 6.4.

used in the majority of the experiments. Even when running the laser with a repetition rate of 40 Hz the exposure times required to illuminate a 23 mm long grating by a dose of 400 J/cm^2 is almost an hour. In a deuterium loaded TrueWave fiber such an exposure dose leads to a refractive index modulation amplitude of $n_{\mathrm{mod}} = 2.6 \times 10^{-4}$. Strong sinc gratings require a modulation amplitude of up to 3 times this value thus making the TrueWave fiber less attractive for these gratings. In the deuterium loaded HNLF fiber pre-exposed into the linear regime a modulation amplitude of $n_{\mathrm{mod}} = 13.6 \times 10^{-4}$ is achieved after a 400 J/cm^2 exposure. This fiber is evidently well suited for the inscription of very strong gratings. The 60 J/cm^2 pre-exposure is performed with a several millimeter wide beam and is thus done within a few minutes.

Figures 6.21 and 6.22 show the transmission and reflection spectra of two sinc gratings written in pre-exposed deuterium loaded HNLF fibers. Both gratings were 23 mm long with a taper parameter of $s_{\mathrm{sinc}} = 1/6$. Additional Gaussian apodization was applied using a ratio of $\sigma_{\mathrm{Gauss}} = 7$ between the taper parameters of the Gaussian and sinc profiles. The simulated spectra seen in the figures were calculated using maximum index modulation amplitudes of $n_0 = 4.75 \times 10^{-4}$ and $n_0 = 19 \times 10^{-4}$ for the 6 dB and 50 dB gratings respectively. A bandwidth utilization factor, BWU, can be defined as the ratio between the 1 dB reflection bandwidth and the 30 dB reflection bandwidth. In the present grating the factor equals BWU = 70 % and the wall steepness at 10 dB is measured to be 1.5 dB/GHz. With the additional Gaussian apodization a strong side lobe suppression is anticipated in both gratings. The measured suppression is in general weaker than what is expected from the simulations as illustrated in Figure 6.21. This discrepancy may be caused by several factors. Weak but finite reflections occur at the fiber splices and at the connection to the optical measurement setup. The strength of these reflections will set the noise floor of the measurement. Given a 0.1 % reflection in the setup the noise floor will be at -30 dB. Furthermore may reflections from fiber splices also interfere with the side lobe ripples to increase the strength of these. A π phase shift between the two polarizations is only obtained exactly at the center of the fiber core. The distance dependent separation between the index modulation profiles of the two polarizations will cause an offset at the edges of the fiber core. This results in a weak tilted grating, which may interfere with the grating of interest to reduce the side lobe suppression. A small but finite polarization dependence on the UV induced n_{mod} will also result in a weak grating co-existing with the desired grating leading to a reduced side lobe suppression.

6.8.3 Asymmetric gratings

Strong dispersion reduced gratings were designed to give a square filter function with a constant strong reflection in the stop band and zero reflection in the pass band. The dispersion in both bands was set to equal zero. Most gratings were designed to have a transmission dip in the order $20 - 30$ dB, but also gratings with about -60 dB transmission were designed and realized. The grating design specify both the shape and strength of the modulation profile. Using a modula-

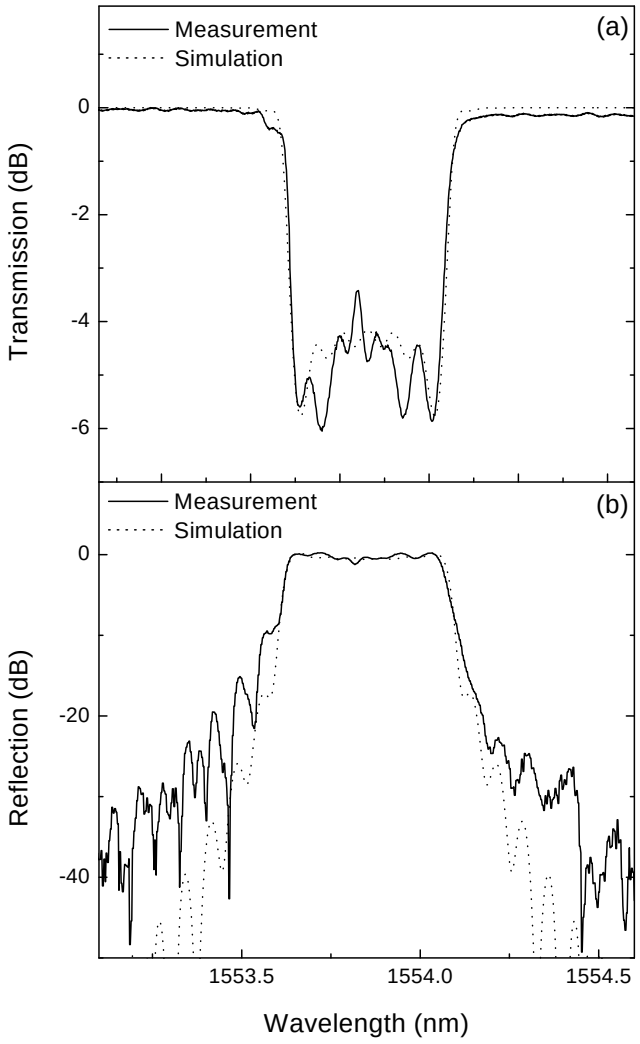

Figure 6.21: Transmission (a) and reflection (b) spectra for a 23 mm long medium strength symmetric sinc grating written in a pre-exposed deuterium loaded HNLF fiber. The refractive index modulation amplitude and the polarizer angle profiles are seen in Figure 6.5.

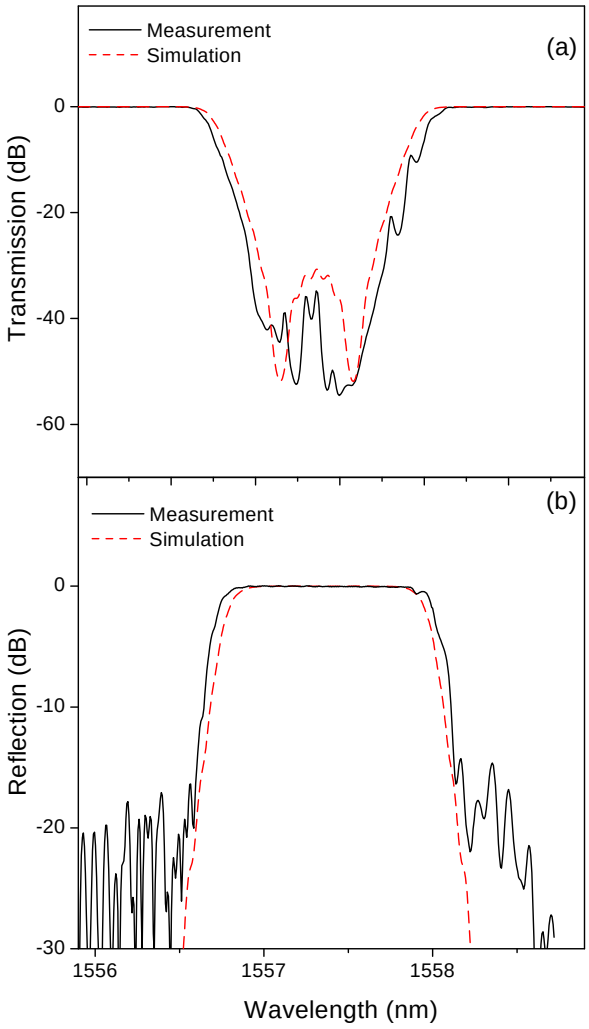

Figure 6.22: Transmission (a) and reflection (b) spectra for a 23 mm long symmetric very strong sinc grating written in a pre-exposed deuterium loaded HNLF fiber. The refractive index modulation amplitude and the polarizer angle profiles are seen in Figure 6.5.

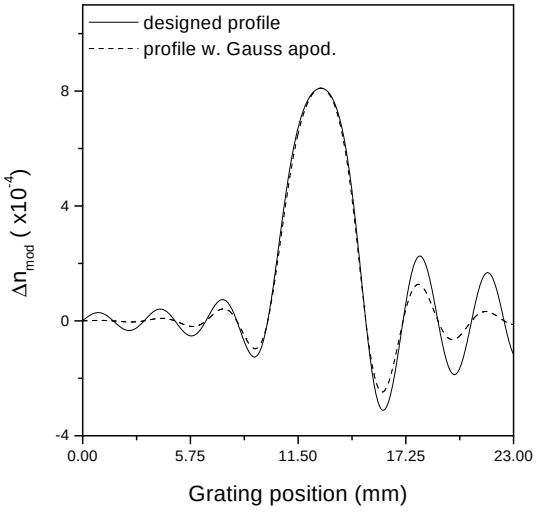

Figure 6.23: Modulation amplitude profile for a designed grating with and without the additional Gaussian apodization. The center of the Gaussian apodization profile must coincide with the center peak of the designed grating profile in order to obtain an efficient suppression of the Gibbs phenomenon. The grating is designed for inscription in a HNLF fiber.

tion amplitude 20 % off the optimum value will severely affect both the shape of the reflection peak and the dispersion properties of the grating. An example of the highly asymmetric gratings designed during this study was presented earlier in Figure 6.6. Both simulations and measurements of the amplitude response showed only negligible dependence on the direction of propagation of the pulse signal in the grating. This behavior has also been reported by other groups [6]. The phase response on the other hand strongly depends on the direction of propagation [8]. This indicates that the phase properties of the reflected pulse are highly influenced by the structure of the grating fringes and in particular the periodicity of the phase shifts.
The modulation amplitude profile for one of the designed Bragg gratings realized during this study is depicted in Figure 6.23. This grating was designed for inscription in a HNLF fiber. It was written in a pre-exposed deuterium loaded HNLF fiber with a 0.7 mm wide excimer beam. With the minimum distance of 1.6 mm between two adjacent phase shifts, this beam width is well below the acceptable upper limit. If a wider beam is used the pattern transfer to the fiber is severely affected, thus smearing out the detailed structure of the modulation amplitude profile. The transmission and reflection spectra of this grating are shown in Figure 6.24. The simulated data presented in this figure are calculated by estimating the maximum index modulation amplitude by comparison with the measured spectra. An example of a very strong sinc grating with -60 dB transmission is seen in Figures 6.25 and 6.26. The grating has a 1 dB reflection bandwidth of 100 GHz, and a wall steepness of 5.6 dB/GHz. Ignoring the side lobes and extrapolating the wall down to -30 dB a BWU of 88 % is found

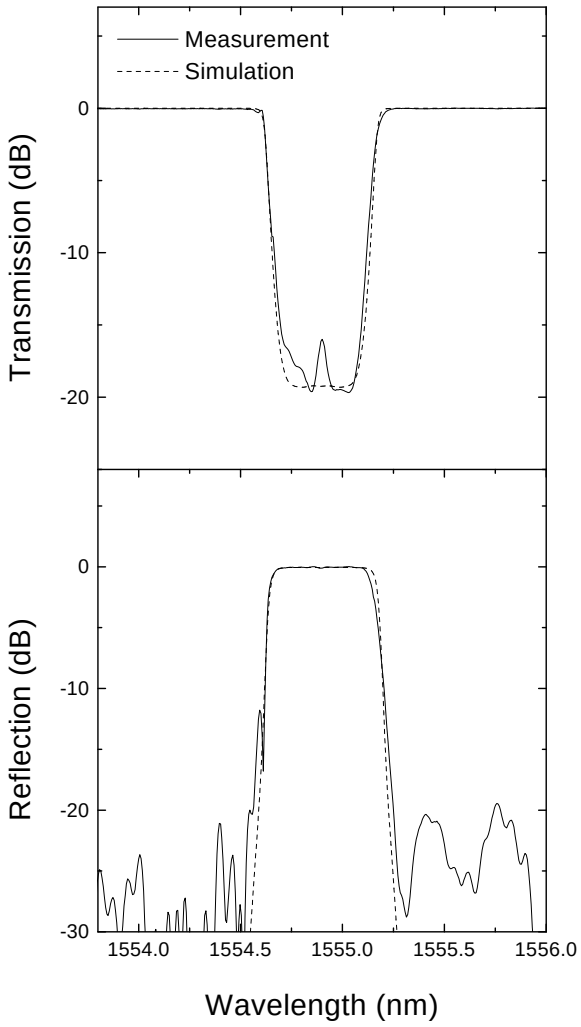

Figure 6.24: Transmission and reflection spectra of a grating with the index modulation profile presented in Figure 6.23.

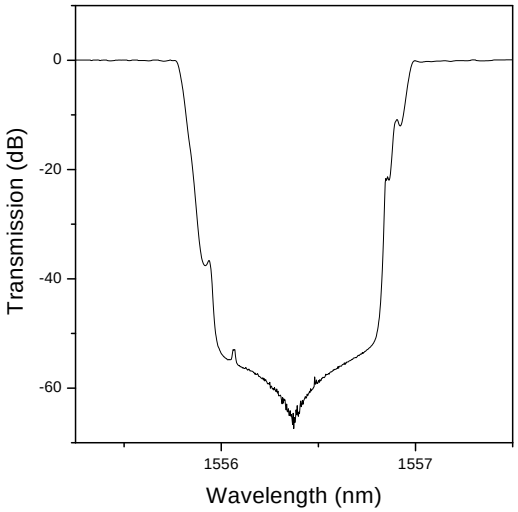

Figure 6.25: Transmission spectrum of a 23 mm long asymmetric very strong sinc grating written in a pre-exposed deuterium loaded HNLF fiber.

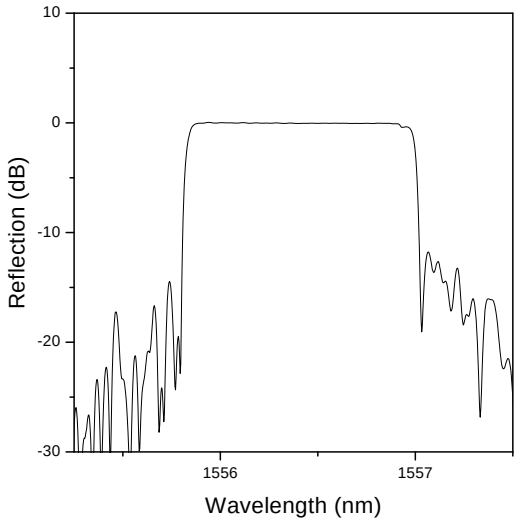

Figure 6.26: Reflection spectrum of a 23 mm long asymmetric sinc grating written in a pre-exposed deuterium loaded HNLF fiber.

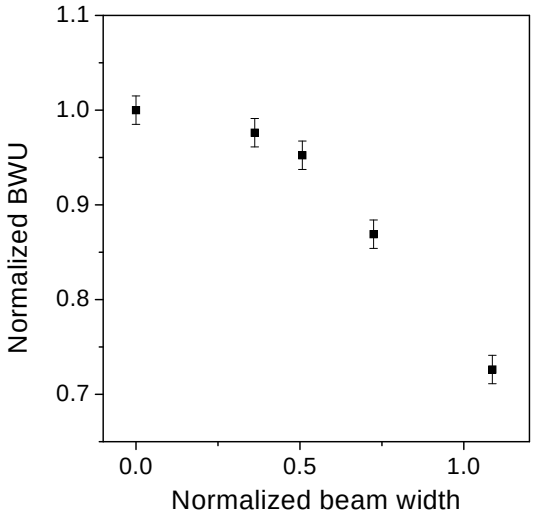

Figure 6.27: Bandwidth utilization normalized to the zero beam width case as a function of the ratio between the beam width at the distance between two neighboring phase shifts.

for this grating. Comparing this designed grating with the 100 GHz symmetric sinc grating presented in 6.22, the improvement is evident with the BWU factor increasing from the observed 70 % in the symmetric grating to the value described above.

The finite width of the excimer beam results in a decrease of the bandwidth utilization relative to the zero beam width case as seen in Figure 6.27. This figure shows the bandwidth utilization normalized to the zero beam width limit as a function of the ratio between the beam width and the distance between two neighboring phase shifts. This simulation shows that using beam widths as large as one half of the phase shift periodicity in the grating only have a weak influence on the properties of the written grating. The use of a 0.7 mm wide beam for inscription of gratings with a distance between successive phase shifts of 1.6 mm is thus acceptable. Once the beam width approaches the phase shift periodicity the normalized bandwidth utilization is reduced by 30%, which is unacceptable for high capacity DWDM transmission systems with closely spaced channels. For beam widths smaller than the phase shift distance, it is primarily the bandwidth utilization and side-lobe suppression that is affected and not the roll-off slope of the reflection peak.

The dispersion properties of two asymmetric gratings written during this study showed excellent accordance between measured and simulated phase delay. The amplitude and phase responses were measured from both sides and confirmed the results obtained in the simulations; the amplitude response is independent on which side of the grating the signal pulse is launched from, while the phase response is altered significantly. The results are presented elsewhere [8].

6.9 Comparison with competing methods

This section briefly describes some of the competing methods for UV writing of advanced Bragg gratings. All the mentioned methods are as the polarization control method capable of producing apodized gratings with a constant Bragg resonance wavelength throughout the grating. The double-exposure technique [60] defines the apodization profile in the first scan before a second scan without the phase mask raises the effective refractive index to a constant value throughout the grating. A second method using custom made phase masks with incorporated phase shifts [62] and/or variable diffraction efficiency [77, 61] provides a robust and highly reproducible method for inscription of gratings with a medium complexity. The flexibility of this approach is limited and a new often very expensive phase mask is required for every type of apodization profile. More advanced methods are capable of apodizing the grating by either applying a symmetric longitudinal stretch during the inscription [78], by using a wedge to introduce a path-length difference across the wavefront of one of two interfering beams [79], by writing consecutive subgratings slightly out of phase [80], or by applying a dither to the fiber during writing [81]. Of these methods only the last two are capable of producing arbitrary apodization profiles including several phase shifts and the polarization control method should primarily be compared with these two.

6.9.1 The moving fiber-scanning beam technique

One of the most successful techniques for the inscription of advanced gratings with several phase shifts is the moving fiber scanning beam technique [81]. The cornerstone of the method is the movement of the fiber relative to the phase mask, while the beam is scanning along the phase mask. By dithering the phase mask the amplitude of the index modulation can be varied continuously between the maximum (steady fiber) and zero modulation amplitude (dither amplitude equal to half the grating pitch). Since the accumulated fluence is constant along the fiber a pure apodization with a constant effective refractive index throughout the grating is realized. Phase shifts in the grating are realized by moving the fiber half the grating pitch when the scanning beam is at the position, where the phase shift is needed. Sinc gratings as well as phase shifted gratings for DFB lasers can hence be produced by using the moving fiber-scanning beam method.
The implementation of the moving fiber scanning beam method is a huge task due to the requirement for interferometric control of the position of the fiber relative to the phase mask.

6.9.2 Position weighting method

In the position weighting method, [80] (also referred to as the multiple printing in fiber method), the fiber is moved between every successive pulse. If the distance traveled between two pulses equals one full period of the grating the individual subgratings add to give the maximum grating strength. Any devia-

tions from this distance will reduce the grating strength with zero modulation amplitude when the subgratings are π out of phase. This facilitates a continuous change of the modulation amplitude and thus allows for the inscription of apodized gratings. When the offset between the subgratings is larger than half the modulation period, a phase shift is introduced in the grating. The position weighting method can hence be used to inscribe Bragg gratings with several phase shifts, such as sinc gratings.
The disadvantages of the position weighting method is the requirement for an extremely good control over the fiber position and the laser pulse timing. It is doubtful that this method could have been implemented using the excimer laser available in our laboratory. The necessary timing of the pulse would not be possible thus introducing random deviations in the modulation amplitude.

6.9.3 Conclusion

The force of the polarization control method is the capability of writing highly advanced gratings including several phase shifts using a uniform phase mask. Of the methods mentioned in this section only the moving fiber methods are capable of writing gratings of similar complexity. Compared with the polarization control method, where the modulation amplitude and the phase shifts are controlled by the angle of a polarizer, these two methods appear to be significantly more sensitive towards vibrations in the setup and require highly expensive equipment to control the fiber position. The moving fiber methods provide a slightly higher flexibility than the polarization control method and are most likely better when it comes to writing extremely sophisticated gratings. The polarization control method on the other hand is capable of writing very strong gratings with a lower price per component. Since the quality of gratings with similar apodization profiles written using either the moving fiber methods or the polarization control method are of comparable quality, we conclude that the polarization control method is a very strong alternative to the competing methods for UV writing of advanced gratings in optical waveguides.

6.10 Conclusion

In conclusion we have developed the flexible and easy-to-use polarization control method for UV writing of Bragg gratings with advanced apodization profiles including several phase shifts. Gratings are written by scanning a UV beam along the phase mask and fiber, which both are stationary during the exposure, while rotating a UV polarizer. The method is based on a spatial separation of the *s*- and *p*-polarizations of the UV beam. A polarization beam splitter positioned a few millimeters above the phase mask refract the two orthogonal polarizations of the beam in different directions. The two diverging single-polarization-state beams emerging from the beam splitter are diffracted by the phase mask and two slightly offset interference patterns are observed at the fiber core. The resulting modulation patterns in the refractive index of the fiber core are π out of phase at a certain distance between the phase mask and the fiber. A rough estimate of this distance can be calculated by using a simple pocket calculator

friendly equation. For a precise optimization of the distance weak sinc gratings were written. The reflection spectra of these gratings reflects the deviations from the optimum distance with a peak in the center of the reflection peak when there is an offset in the distance. The distance is adjusted accordingly and new test gratings are written until the reflection spectrum show that the distance is at the optimum value. When the phase mask is positioned at the correct distance to the fiber, a change of the polarization of the scanning UV beam will introduce a phase shift in the Bragg grating. The orientation of a pile-of-plates polarizer mounted on a computer controlled rotation stage determines the polarization of the incident beam thus allowing for a gradual change from one polarization to the other. A procedure similar to the optimization of the phase mask to fiber distance is performed to adjust the polarizer angle reference point. Maximum refractive index modulation is obtained when only one polarization is present i.e. when the polarizer angle is either 0° or 90° giving a pure p- or s-polarized beam respectively. When equal amounts of the two polarizations are present the resulting index modulation is zero. The change in the effective refractive index is determined only by the scan speed and is thus constant throughout the grating, while the polarizer angle determines the amplitude and phase of the refractive index modulation. Chirp-free apodized gratings can hence be written in a single scan in contrast to the double-exposure method, which requires a second scan to raise the effective refractive index to a constant level throughout the grating.

The by far most interesting aspect of the polarization control method is the capability of writing gratings with several phase shifts. When the polarizer angle crosses either $-45°$ or 45° a change in the dominant polarization occur and a phase shift is realized. In combination with the adjustable refractive index modulation amplitude this allows for the inscription of virtually any grating profile. In this study both symmetric sinc and asymmetric sinc-like gratings have been successfully realized in deuterium loaded optical fibers. Excellent accordance between simulated and measured spectra was obtained proving the usefulness of the polarization control method. Sinc gratings with transmission losses as high as 50 dB were written in deuterium loaded commercially available and experimental fibers. Strong dispersion reduced Bragg gratings were designed using commercial software. The resulting gratings showed band width utilization factors close to 90 % with wall steepness of the reflection peak of 5.6 dB/GHz.

The implementation of the polarization control method using an excimer laser is presently at a level, where only minor improvements can be made. The spectra of the fabricated gratings are in excellent accordance with simulations and the reproducibility of the written gratings is very good. The focus in the future application of the polarization control method is hence on the properties of the Bragg gratings rather than on the inscription of these. The performance of the Bragg gratings when used as components in Wavelength Division Multiplexing systems will become the primary focus area in the time to come. Especially the fabrication of low-dispersion gratings is an interesting subject, where the

polarization control method can realize very complex grating profiles designed to give the excellent performance.
If the performance of the polarization control method is to be improved significantly the technology should be transferred to a setup using a high coherence UV source such as the cw lasers described in Section 5.2.2. The cw lasers available at COM are inherently linearly polarized and the pile-of-plate polarizer must be replaced by a half-wave-plate or another polarization controller, which can rotate the field vector of the linearly polarized UV beam.

Chapter 7

Bragg gratings in planar waveguides

7.1 Fabrication

The planar waveguides used in this study were all produced at the cleanroom facilities at MIC and COM, DTU. This chapter briefly accounts for the production steps involved, while the author refers to D. A. Zauner [82] for more elaborate description. Samples for the experiments on ultra high pressure deuterium loaded waveguides were supplied by H.Ou (henceforth referred to as HO-A3) and J. M. Jouanno (JMJ-97), while the 100 bar D_2 loaded samples all were produced by L. Leick, D. A. Zauner and the author (LL708A) using recipes developed by D. A. Zauner and others.
The fabrication of planar waveguides includes a large number of steps where different processes come into play. The thin film layers in the structure are deposited by Plasma Enhanced Chemical Vapor Deposition (PECVD) as described in section 7.1.1, while the waveguides are defined by photolithography and subsequent removal of excess material by Reactive Ion Etching (RIE) as described in Sections 7.1.2 and 7.1.3.
The starting material for the fabrication of the planar waveguides used in this study were silicon wafers with a thermal oxide layer acting as buffer. The wafers were steam oxidized for 4 weeks resulting in a highly uniform 16 μm thick silica layer on both sides of the substrate. This procedure reduces the stress-induced bowing of the wafer otherwise experienced when the buffer layer is deposited by PECVD. This compressive stress is due to a difference in the thermal expansion coefficients of silica and silicon and arises primarily during cool-down after annealing.

7.1.1 Plasma Enhanced Chemical Vapor Deposition

In chemical vapor deposition (CVD) the chemical components react on the surface of the substrate to form a solid film. From the gas phase the components diffuse to the substrate surface, where they migrate until adsorption. The chemical reactions between the reactants then take place at the surface, where a

thin film of the solid product is formed. Some of the reactions are endothermic and require energy to proceed at a useful rate. In Plasma Enhanced CVD energy is supplied by a RF field thereby increasing the reaction rates to make the PECVD process a very attractive method for thin film deposition.

Doped silica glass

The refractive index of the thin film layers deposited is mainly determined by the composition, i.e. the chemical components and their concentrations. The process used to deposit pure silica is

$$SiH_4(g) + 2N_2O(g) \rightarrow SiO_2(s) + 2N_2(g) + 2H_2(g) \tag{7.1}$$

During the deposition there is an excess of N_2O, which reacts with the hydrogen molecules to produce water and nitrogen molecules. By adding different gases into the reaction chamber it is possible to dope the silica glass with materials that may alter both the optical and the mechanical properties of the film. The refractive index can be raised above that of pure silica by doping with either germanium or phosphor. An increase in the strength together with a slight shift in the wavelength of the electronic resonances [83, 84] raise the refractive index of germania above that of silica. The electronic configuration in the valence shell of Ge is identical to that of Si and the inclusion of germania in the silica thin film does not alter the mechanical properties. Phorphor on the other hand has a different configuration and is incorporated as P_2O_5. It is known to lower the melting point of the glass, thus improving the floating properties of the glass making phosphor doped silica suitable for filling small voids between closely spaced waveguides. Phosphor-doping is hence often used in the cladding layer. By codoping the cladding layer with a precise amount of boron, which reduces the refractive index of the glass, it is possible to match the refractive index of the buffer. The chemical processes used to deposit GeO_2, P_2O_5, and B_2O_3 are:

$$\begin{aligned} GeH_4(g) + 2N_2O(g) &\rightarrow GeO_2(s) + 2N_2(g) + 2H_2(g) \\ 2PH_3(g) + 5N_2O(g) &\rightarrow P_2O_5(s) + 5N_2(g) + 3H_2(g) \\ B_2H_6(g) + 3N_2O(g) &\rightarrow B_2O_3(s) + 3N_2(g) + 3H_2(g). \end{aligned} \tag{7.2}$$

7.1.2 Photolithography

Once the core layer is deposited and annealed to give a uniform layer, the waveguides are defined by photolithography. The wafer is coated by a UV sensitive polymer film by spin-coating followed by a pre-bake. The latter is included in order to obtain a homogeneous resist layer without imperfections. The resist

coated wafer and a mask are brought into contact in an aligner equipped with a mercury lamp. The mask consists of a transparent plate with the waveguide pattern defined by chromium lines. After exposure with a mercury lamp the solubility of the exposed areas is increased significantly and they can be removed by immersing the wafer in a suitable developer. After a hard-bake the resist pattern can be used as mask for the following removal of the core layer in between the waveguides by Reactive Ion Etching.

7.1.3 Reactive Ion etching

The removal of excess core layer material was done using Reactive Ion Etching (RIE). A plasma of highly reactive ions is generated above the wafer surface by a RF field. With the wafer positioned at the bottom electrode these ions can be accelerated towards the wafer surface. If the pressure in the chamber is high, the average kinetic energy of the ions from the plasma is low. The etching is then predominantly chemical giving an isotropic etch. This is not a desirable situation since the waveguide side-walls preferably should be straight and vertical. When the chamber pressure is reduced the velocity of the reactants in the plasma increase and the etching proceeds through sputtering and becomes highly anisotropic. At the intermediate chamber pressure the etch is still anisotropic, but now with slightly tilted side-walls. This regime has the advantage of improved step coverage of the waveguide during the subsequent deposition of the cladding layer. Our waveguides were etched using CHF_3 as etchant, which generate a polymer film at the side-walls during etching. This film protects the side-walls against excessive chemical etching and thereby preserve the almost vertical side-wall profile. After 70 minutes etching the core layer in the resist-free regions is completely removed and a short process was run to strip the resist of the wafer.

7.1.4 Fabrication steps

Prior to the PECVD deposition of the germanium doped core layer, test wafers were made using different flow rates of GeH_4 in order to determine the correct rate required to obtain the desired refractive index in the core layer. A GeH_4 flow rate of 1.1 Sccm was chosen for the deposition of the core layer resulting in a refractive index $n_{\text{core}} = 1.4518$. The PECVD deposition of the core layer is followed by a 2 hour 1100 °C anneal in steam, which ensures a good uniformity of both layer thickness and refractive index.
After waveguide definition by photolithography and Reactive Ion Etching a boron and phosphor doped top cladding layer is deposited by PECVD in two steps. First a 8 μm layer is deposited and annealed for 2 hours. The low viscocity of this film enables it to fill the voids between the waveguides. A second layer 14 μm thick is then deposited and finally annealed. The flow rates of the two dopants are determined before the deposition by a test wafer run including annealing to match the refractive index of the buffer.
The final result is a batch of high quality waveguides with an almost square core of dimensions $\approx 5.5 \times 5.5 \mu m^2$ with an absolute index step at the core of

0.007, giving a confinement factor of $\eta = 0.7$.

7.2 Photosensitivity

Growth curves were measured during UV exposure to determine the relation between the induced refractive index change and the accumulated UV fluence. Since the waveguides used in this study all were annealed in an oxygen rich atmosphere during fabrication, the photosensitivity is negligible unless the samples are sensitized by deuterium loading. Samples were hence room temperature loaded either at 100 or 1800 bar deuterium pressure for 10 respectively 21 days giving a nominal deuterium concentration in the core of 1.16 and 20.9 mole percent respectively [38], when assuming a linear relation between the loading pressure and the resulting concentration. The validity of this assumption is questionable at ultra high loading pressure and a deuterium concentration in the core slightly lower than 20 mole percent is expected. The relatively low deuterium concentration obtained using a 100 bar pressure did not alter the guiding properties of the waveguides significantly. When measuring on the 1800 bar loaded samples the author found an increase in the transmission loss in excess of 50dB. After deuterium out-diffusion the transmission loss was down at the normal level of a few dB. The change in the guiding properties is to be expected at the high deuterium concentration, where the deuterium molecules no longer can be expected only to occupy micro-cavities in the glass matrix. Unfortunately, this increase makes the growth curve measurements less precise than what can be obtained using 100 bar loaded samples.
A general observation in all the deuterium loaded planar waveguides was a complex growth in the beginning of the UV exposure i.e. the first $0 - 750\,\mathrm{J/cm^2}$. While the refractive index modulation and hence the reflection at the Bragg wavelength continuously increases, the change in the effective refractive index shows at least one local maximum. Similar behavior was encountered in several samples with different deuterium concentrations and fabrication histories. Figures 7.1 and 7.2 show the refractive index modulation n_{mod} and change in effective refractive index Δn_{eff} versus fluence for a 100 bar deuterium loaded LL708A waveguide. A plausible explanation for the observed behavior is a complex interplay between thermal assisted photo-dissociation of the deuterium molecules [18], tensile stress in the core [85] and creation of different germanium related oxygen deficient centers [29, 27]. Defect centers like Ge(1) and Ge(2) may affect only effective refractive index without causing any change in the index modulation [27]. After an initial growth a continued UV exposure may erase some of these defect centers leading to a decrease in the effective refractive index, without affecting the refractive index modulation. UV illumination of defects can hence both increase and decrease the effective refractive index as well as generate an index modulation depending on the nature of the activated defects. The photo-dissociation on the other hand will only give a decrease in the effective refractive index and hence the Bragg wavelength. The presence of D_2 molecules in the waveguide core increases the refractive index with 0.12% per mole % D_2 [44] corresponding to an increase in the refractive index of 0.14%

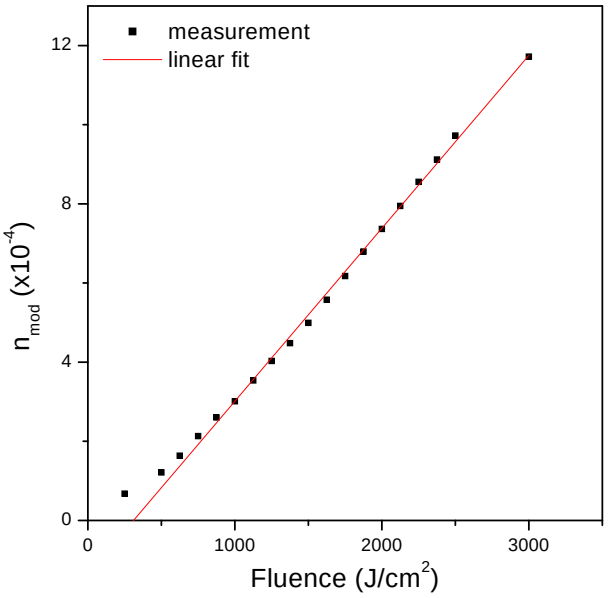

Figure 7.1: Growth of index modulation amplitude versus accumulated fluence in a LL708A sample. The measured values are fitted by $n_{\mathrm{mod}} = 1.91 \times 10^{-4} + 4.37 \times 10^{-7}(F - 750)$

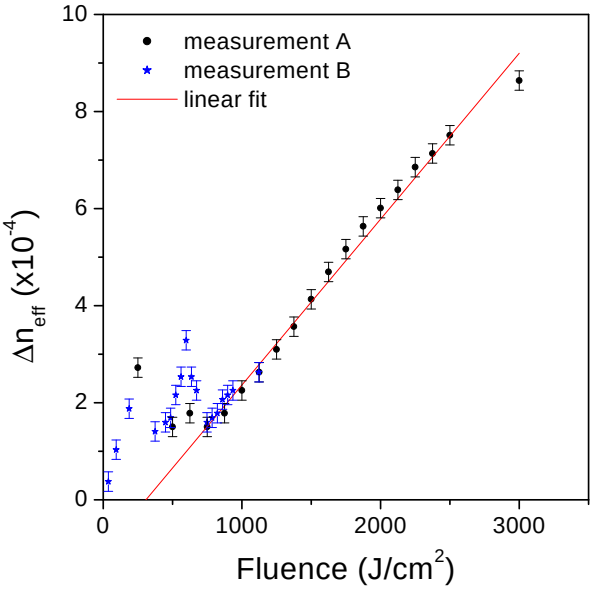

Figure 7.2: Growth of effective refractive index versus accumulated fluence in a LL708A sample. The experimental data are fitted by $n_{\mathrm{eff}} = 1.51 \times 10^{-4} + 3.42 \times 10^{-7}(F - 750)$

in the 100bar loaded samples. Using a phase mask of period $\Lambda_{\text{mask}} = 1070\,\text{nm}$ this gives a change in the Bragg wavelength of almost 1.5 nm. UV-induced tensile stress in the core can result in a 30% reduction of the refractive index [85]. The number and complexity of the processes active during UV exposure may thus result in the complex behavior seen in the beginning of the exposure. Once the UV absorbing defect centers are activated, the change in the refractive index is dominated by the UV induced creation of other defects such as GeE' centers, which raise the refractive index through the Kramers-Kronig relation. Quantification of the complex behavior is out of the scope in this study.
For a large number of the Bragg gratings written in planar waveguides the author did a $750\,\text{J/cm}^2$ blanket pre-exposure to raise the waveguides above the initial region. From this point and on, the change in n_{mod} and Δn_{eff} are both linear as seen in Figures 7.1 and 7.2. The effective refractive index and the index modulation at a fluence of $F = 750\,\text{J/cm}^2$ then accounts for the induced changes during the activation processes in the beginning of the exposure. In the fabrication of uniform gratings this pre-exposure may be omitted. Nice uniform gratings with spectra in excellent agreement with simulations were produced without a pre-exposure as seen in Figure 7.5 and 7.6. This could indicate that the visibility of the phase mask defined interference pattern was low. The modulation profile then only covers a small part of the growth curve thus making the grating less dependent on a completely linear refractive index dependence of the accumulated fluence. In the uniform grating the average fluence is constant throughout the grating and the evolution in the effective refractive index versus accumulated fluence is not critical.
For a given exposure fluence the change in the refractive index in the 1800 bar loaded waveguides was significantly increased compared to the 100 bar loaded waveguides. An index modulation of 1.6×10^{-3} was induced by a $1\,\text{kJ/cm}^2$ exposure in the 1800 bar loaded sample HO-A3, which is approximately 5 times higher than in the 100 bar loaded LL708A waveguide. This result is similar to what have been reported earlier on the dependence of the photosensitivity of the loading pressure [86].

7.2.1 Anneal experiments

The temporal stability of the Bragg gratings is evidently of major importance since any decay of the induced refractive index changes not only affect the strength of the grating but also its center wavelength. In a typical 20 mm long 30 dB strong raised Gaussian grating the UV induced change in the effective refractive index is in the order of 5×10^{-4} corresponding to a shift in the Bragg wavelength of 0.54 nm. In such a grating the 3 dB width of the reflection peak is 0.22 nm and a shift in the center wavelength of only 0.11 nm, i.e. a 20% decrease in n_{eff} will be devastating for the grating performance. A decrease in the refractive index modulation will cause an increase in cross talk when the grating is used as for instance an Add-Drop multiplexer. Using the model by Erdogan [39] or the dipole-quadropole model by Kristensen [22] it can be seen that a pre-anneal of the grating by heating the waveguide to above room temperature will erase the short lived defects and leave only long term stable

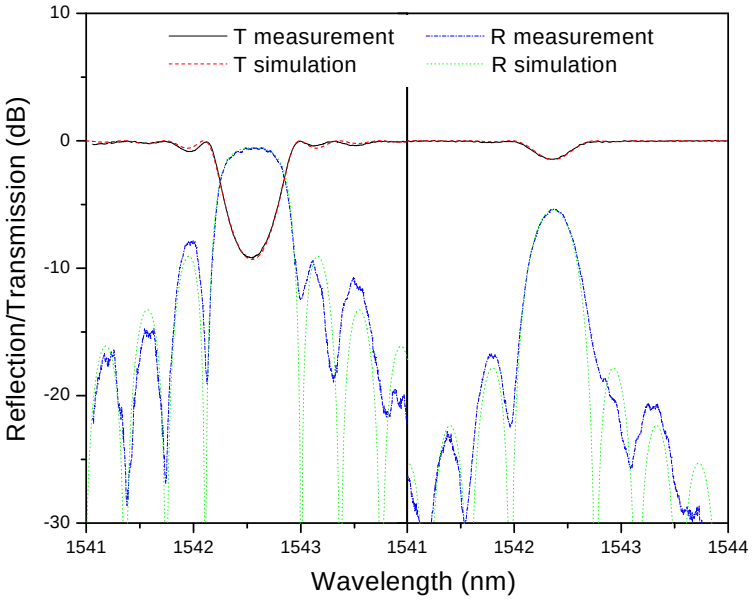

Figure 7.3: Transmission and reflection spectra of a 2.1 mm uniform grating written in a 100 bar deuterium loaded LL708A waveguide before (left graph) and after (right graph) a 3 hour anneal at 500 °C. The refractive index modulation decreases from 5.8×10^{-4} to 2.0×10^{-4}, while the blue shift in Bragg wavelength is 0.18 nm.

defects. In this study the author was primarily interested in how the use of Ultra High Pressure (UHP) loading affected the temporal stability of the induced gratings. As mentioned in Section 7.2 the photosensitivity is approximately 5 times higher when using UHP loading compared to the standard 100 bar loaded samples. Obviously this improvement is only of commercial interest if the UV induced changes are as stable as those obtained in the standard loaded samples. The stability was investigated in an annealing experiment, where both 100 bar and 1800 bar loaded samples were annealed at 500 °C for 3 hours leaving only very stable index changes in the waveguides. The transmission and reflection spectra before and after annealing are seen in Figure 7.3 and 7.4. Evidently the thermal induced decay is similar for the two deuterium loading concentrations. Given the similarities in the growth curves and the subsequent annealing experiment it seems reasonable to conclude that the UV induced changes in the refractive index originates from the same defects when using standard and ultra high pressure loaded samples. Extrapolating these results to gratings with higher refractive index modulations, still in the regime with a linear refractive index growth, ultra high pressure loading facilitates the fabrication of Bragg gratings with $n_{\mathrm{mod}} > 10^{-3}$ after a 500 °C anneal using exposure fluences below 2 kJ/cm^2. Ultra high pressure loading is evidently an effective method for sensitizing optical waveguides in order to obtain large stable changes in the refractive index by UV exposure.

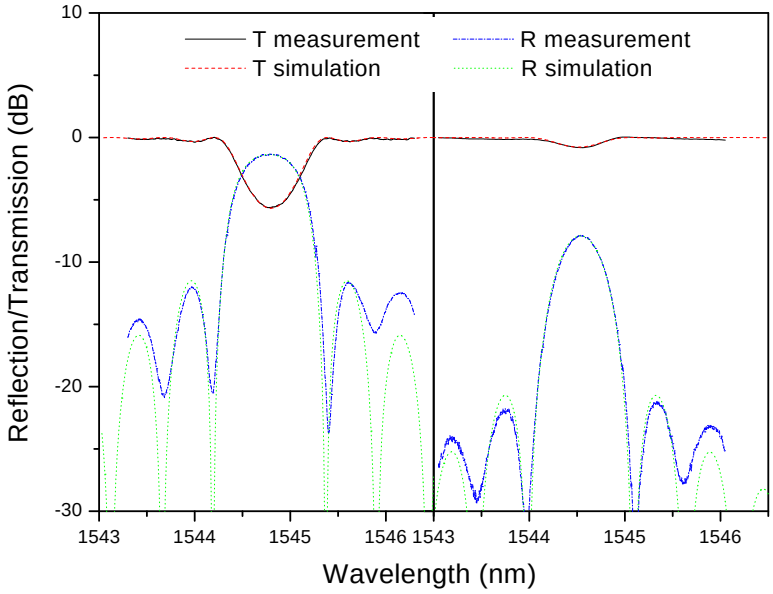

Figure 7.4: Transmission and reflection spectra of a 1.5 mm uniform grating written in a 1800 bar deuterium loaded HO-A3 waveguide before (left graph) and after (right graph) a 3 hour anneal at 500 °C. The refractive index modulation decreases from 5.9×10^{-4} to 2.0×10^{-4}, while the blue shift in Bragg wavelength is 0.23 nm.

7.3 Dual-scan method written gratings

In the dual-scan setup used for Bragg grating inscription in optical fibers and planar waveguides the beam is moved relative to the sample by a mirror mounted on a translation stage. The software designed to control the translation stage position and velocity relative to the sample can in principle be used to write any apodization profile, which does not require a phase shift. In this part of the study the author has focused on writing Gaussian and raised Gaussian gratings using the dual-scan method [78]. In this method, the index modulation profile is defined in the first scan followed by a second scan without the phase mask. The latter raises the effective refractive index to the same constant value throughout the grating, while maintaining the index modulation profile required the photosensitivity is a linear function of the accumulated fluence. The results on gratings written in deuterium loaded planar waveguides using this setup is the topic of this section.

7.3.1 Uniform gratings

By scanning the laser beam along the waveguide and defining the grating length by UV absorbing glass plates, a true uniform fluence profile is achieved. The glass plates are required to obtain the correct uniform profile. If they are omitted, a tapering is seen at both entrance and exit of the grating resulting in a distorted grating spectrum. It is possible to derive the exact analytical expression for the transmission through a uniform grating as seen in Section 4.3.1. With the exact expression in hand the uniform grating is an excellent probe of the quality of the planar waveguides. It is seen in Figures 7.5 and 7.6 that the measured data are very convincingly fitted by the theoretical expression. Beside a week coupling to the cladding modes there is no transmission loss away from the center of the Bragg grating as plotted in Figure 7.7. Short Bragg gratings with length in the order of a few millimeters can conveniently be written by parking the beam at the desired position. The excimer laser beam profile along the scan direction is Gaussian as mentioned in Section 5.2.1, but when only the center part of the beam is used, it is a good approximation to assume that the beam is uniform. This is supported by the excellent match between the measured and simulated spectral shape of the grating presented in Figure 7.3, where the grating length of 2.1 mm was defined by thick glass plates.

7.3.2 Apodized gratings

In order to obtain a better side-lobe suppression than that seen in the uniform gratings in Section 7.3.1 an apodization of the grating modulation profile is required as described in Section 4.4. To simplify the analysis, this study focus on the Gaussian and the raised Gaussian profiles. Gaussian gratings are inherently chirped due to the non-constant effective refractive index throughout the grating. The spectral response of a Gaussian grating written in a standard loaded waveguide is seen in Figure 7.8 and 7.9 showing the transmission and reflection spectra of a 20mm long Gaussian grating inscribed in a LL708A planar

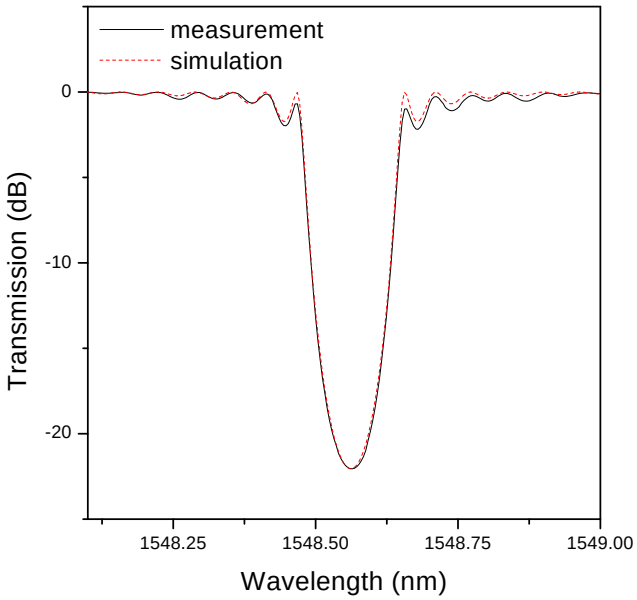

Figure 7.5: The measured transmission spectrum for a 12.5mm uniform grating written in the deuterium loaded planar waveguide LL708A and the simulation using a refractive index modulation of $n_{\mathrm{mod}} = 1.82 \times 10^{-4}$.

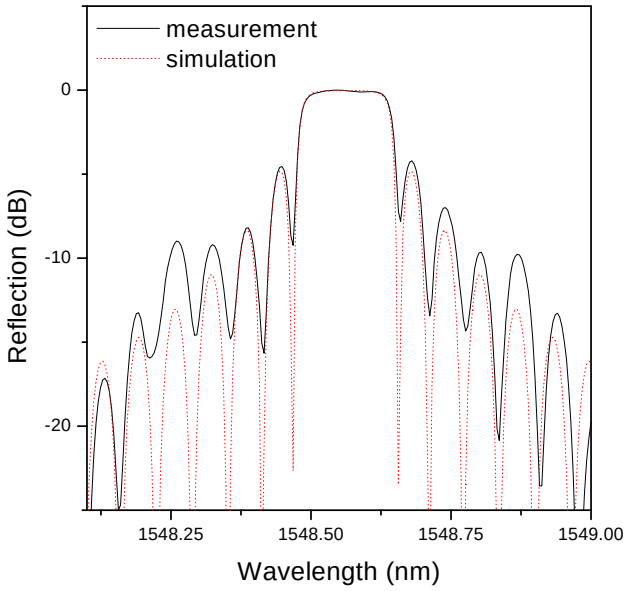

Figure 7.6: The measured reflection spectrum for a 12.5mm uniform grating written in the deuterium loaded planar waveguide LL708A and the simulation using a modulation of $n_{\mathrm{mod}} = 1.82 \times 10^{-4}$.

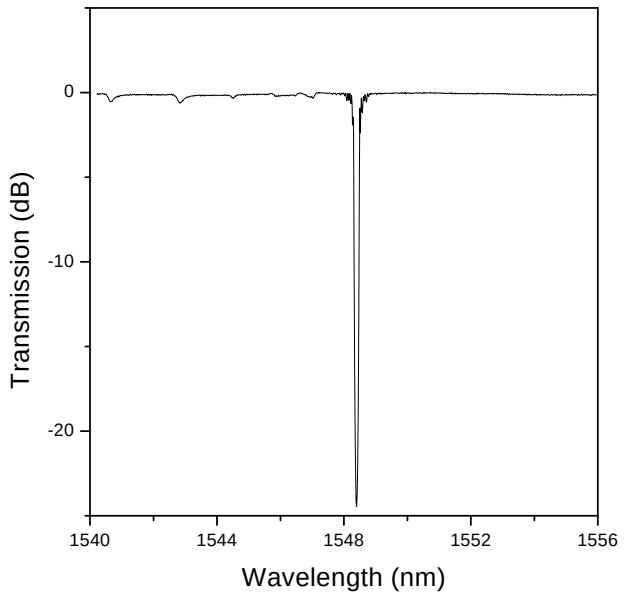

Figure 7.7: A wide span measurement of the transmission loss of a 12.5mm uniform grating written in the deuterium loaded planar waveguide LL708A, showing only a week coupling to the cladding modes

waveguide. The apodization clearly results in a suppression of the side lobes on the long wavelength side of the reflection peak, while the chirp causes the structure on the short wavelength side. In gratings, where an additional exposure without the phase mask was used to raise the effective refractive index to a constant level the side lobes suppression was improved as seen in Figure 7.10.

7.3.3 Sampled gratings

Sampled gratings with their multiple reflection peaks are well suited for wavelength division multiplexing (WDM) systems working for instance as multiple-wavelength add-drop devices. The channel spacing remains almost constant throughout the grating and is easily controlled by the periodicity, z_0, of the amplitude mask used in the fabrication. As described in Section 4.7 the spacing between the reflection peaks in a sampled grating is given by

$$\Delta\lambda \approx \frac{n_{\text{eff}}\Lambda^2_{\text{mask}}}{2z_0} \tag{7.3}$$

From this expression it is seen that by using an amplitude mask with periodicity $z_0 = 700\,\mu m$ the resulting sampled grating will have a channel separation of approximately 150 GHz. The coupling coefficient of the m^{th} reflection peak in a uniform sampled grating is given by [54]

$$\kappa(m) = \kappa_0 \frac{z_1}{z_0} \frac{\sin(\pi m \frac{z_1}{z_0})}{\pi m \frac{z_1}{z_0}} e^{-i\pi m \frac{z_1}{z_0}} \tag{7.4}$$

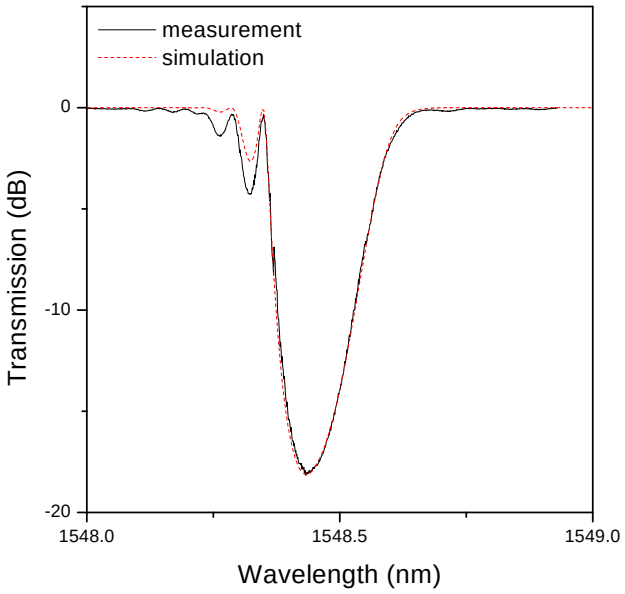

Figure 7.8: The transmission spectrum of a 20mm Gaussian grating written in a deuterium loaded planar waveguide LL708A. Prior to the grating exposure, the waveguide was pre-exposed using a blanket exposure with fluence $F = 750\,J/cm^2$. The simulated data are calculated using $n_{mod} = 2.6 \times 10^{-4}$ together with the taper parameter $s = 0.41$

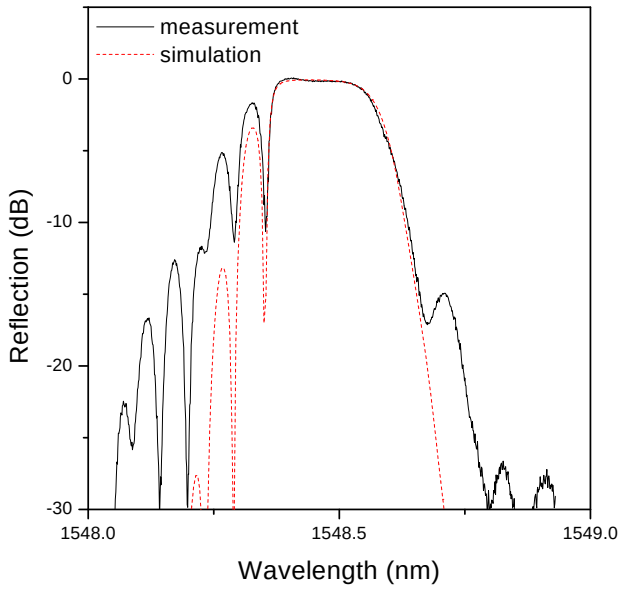

Figure 7.9: Reflection spectrum from a 20mm Gaussian grating written in a D_2 loaded planar waveguide LL708A. Prior to grating exposure, the waveguide was pre-exposed using an exposure of fluence $F = 750\,J/cm^2$. The simulated data are calculated using $n_{mod} = 2.6 \times 10^{-4}$ and taper parameter $s = 0.41$

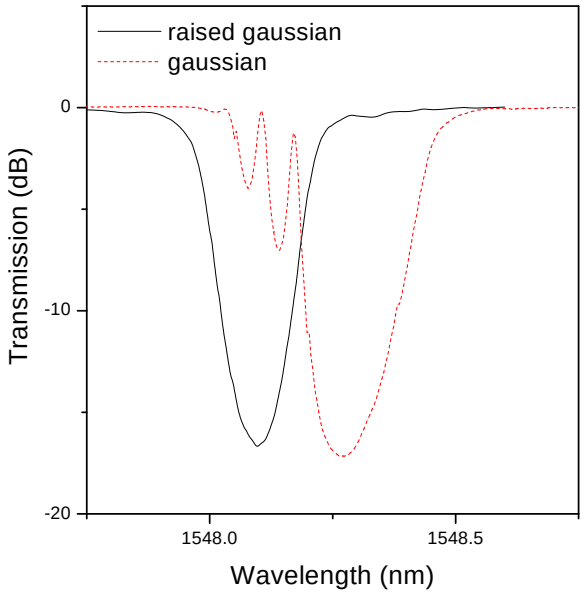

Figure 7.10: Transmission spectra of a Gaussian and a raised Gaussian grating. Both waveguides were pre-exposed with a fluence of $F = 750\,\mathrm{J/cm^2}$.

where the exponential term describes the phase and $\kappa_0 = \kappa(0)$ is the coupling coefficient for the center peak. From this equation it follows that $\kappa(m)$ scales with the inverse of the sampling periodicity, while it grows with the sampling length z_1. The spectral envelope of the full reflection spectrum is determined by the $\sin(x)/x$ term in Equation 7.4. In order to obtain a broad range of reflection peaks, i.e. have a large number of $\kappa(m)$'s with values similar to $\kappa(0)$, one cannot allow z_1 to become large. If a 20% reduction in $\kappa(5)$ relative to $\kappa(0)$ is accepted the ratio z_1/z_0 must be equal to or smaller than 1/14. In order to obtain a strong reflection in each channel one therefore rely on either κ_0 or the full grating length L to be large. L is limited by the size of the wafer, which leaves κ_0 as the only free parameter. This coupling coefficient is determined by the refractive index modulation and very photosensitive material is thus needed in order to write strong uniform sampled gratings with channel spacings in the order of 1 nm. Ultra high pressure loading of the planar waveguides is hence an obvious choice when working with sampled gratings. An example of a 30 mm uniform sampled grating with $z_0 = 700\,\mu\mathrm{m}$, $z_1 = 50\,\mu\mathrm{m}$, and $\Lambda_{\mathrm{mask}} = 1071\,\mathrm{nm}$ is seen in Figure 7.11. Prior to the measurement presented in this figure one polarization was suppressed at the center wavelength. As the peaks move further away from the center peak the suppression gradually decreases. This may be explained by wavelength dependent polarization rotation in the optical measurement setup, where long optical fibers were used. In order to obtain a sampled grating showing no reduction in the reflection away from the center wavelength requires a sinc apodization of the individual sampling periods. This may be accomplished by using advanced amplitude masks.

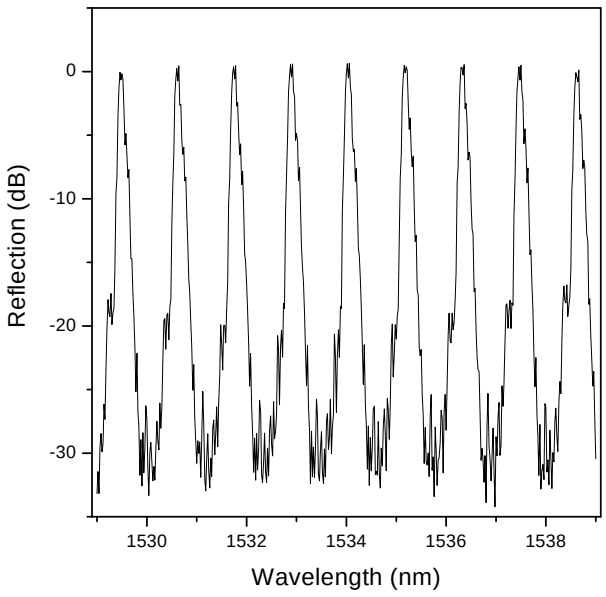

Figure 7.11: The spectrum of a 30mm sampled grating written in a ultra high pressure deuterium loaded JMJ-0997 waveguide using a uniform exposure of fluence F = 1000 J/cm^2

In high capacity WDM systems the channel spacing is evidently a key parameter. In the continued development of optical communication systems the frequency spacing will be pushed down towards 50 GHz, which corresponds to a wavelength spacing $\Delta\lambda$ in the order of 0.4 nm. Sampled gratings for such dense WDM systems require an apodization of the overall grating profile in order to suppress the side lobes on the individual peaks in the reflection spectrum as described in Section 4.7. Without this suppression there will be a significant reflection in between the individual peaks making the component useless for dense WDM purposes. To realize a chirp-free apodized grating using the setup build for the dual-scan exposures, we need to remove the phase mask after the initial scan, while avoiding any displacement of the amplitude mask. With the present setup for dual-scan writing of Bragg gratings this is a very difficult task, but together with N. Plougmann such gratings have been written in optical fibers with success [19].

7.4 Conclusion

This chapter has summarized the results obtained on Bragg gratings in deuterium loaded planar waveguides. The comparision between the measured and simulated reflection and transmission spectra show that the waveguides produced in the cleanroom are of excellent quality. During the fabrication process the waveguides are annealed in an oxygen rich atmosphere in order to improve the guiding properties. Seen from the Bragg grating fabrications point of view

this is unfortunate since the oxygen anneal results in a very low concentration of oxygen deficient defects centers and hence a very low photosensitivity.
Sensitization of the waveguides by deuterium loading was hence required to obtain the required photosensitivity. Samples were D_2 loaded at either 100 or 1800 bar thereby making the waveguides sensitive towards UV light. The measured growth curves, showing the change in effective refractive index and refractive index modulation versus accumulated UV fluence, indicated that initially several processes in the glass determined the nature and concentration of the UV induced defects responsible for the changes in the refractive index. After the initial activation of UV absorbing defects the growth in both effective refractive index and refractive index modulation were linear in the accumulated fluence. The stability of the induced changes in the refractive index is evidently of major importance. A hard anneal at 500 °C, which only leaves highly stable defects, revealed that the stability of defects written in ultra high pressure loaded waveguides is as good as that obtained by using a standard pressure. This is to be expected since we may assume that the majority of the generated defects in the two cases are identical.
Gaussian and raised Gaussian apodization of the gratings was applied to increase the suppression of the side-lobes seen in the spectra of the uniform grating. The inherent chirp in the Gaussian grating causes strong side-lobes at the low-wavelength side of the transmission dip. When the effective refractive index is raised to a constant level throughout the grating the spectra become symmetrical around the center wavelength without any significant side-lobes. Using the dual-scan method for the inscription of apodized gratings requires a linear photosensitivity and the waveguides were thus pre-exposed into the linear regime.
Sampled gratings with their multiple reflection peaks are well suited for WDM systems. The spacing between the channels is determined by the periodicity of the amplitude mask used in the production. Nice uniform sampled gratings were written in ultra high pressure loaded waveguides with channel separations down to 150 GHz. As the need for transmission capacity continues to grow the channel spacing will be reduced, which puts some strong demands on the spectral response of the sampled gratings. An apodization of the overall grating is required in order to suppress the side-lobes on the individual reflection peaks. The dual-scan setup in its present state is not suitable for apodization of sampled gratings, but it has been used to write sampled gratings with a raised Gaussian apodization of the full grating in optical fibers fibers.

Chapter 8

Conclusion

This thesis summarizes the work on Bragg gratings in optical waveguides performed during this Ph.D. study. The effort has been focused on implementing the polarization control method and to a minor extent the fabrication of planar waveguides and inscription of Bragg gratings in these. The novel polarization control method allows for inscription of highly advanced Bragg gratings with the possibility of including several phase shifts. The development of the setup used to implement the method proved to be a huge task with a large number of challenges during the process. Different optical components for handling the polarization of the UV beam from an excimer lasers were tested before the final choices were made. The adjustment of the fiber to phase mask distance and the polarizer angle offset is essential and thorough optimization of both is needed in order to obtain high quality gratings. The results presented in this thesis show that the method now has been developed to a level, where only minor improvements can be made in order to obtain a better correspondence between simulated and measured spectra. The method has been applied to write Bragg gratings with different apodization profiles. The Gaussian apodization is relatively insensitive towards imperfections in the alignment of the setup and nice gratings were written already in the early stages of this work. More advanced profiles such as the sinc-apodization, which includes several phase shifts, are more affected by poor alignment of the setup. This makes sinc-gratings a very sensitive probe on the quality of the alignment. Strong sinc gratings with transmission loss up to 50 dB showing good accordance between simulated and measured spectra were written in deuterium loaded optical fibers. The Fourier transform approach, linking the reflection spectrum to the coupling coefficient of the grating, is only strictly valid for weak Bragg gratings. The fabrication of strong Bragg gratings with square-like reflection peaks thus requires apodization profiles, which are slightly different from the pure sinc profile. A commercial software program was used to design Bragg gratings based on a user input of the desired amplitude and phase response. The resulting asymmetric gratings were then written using the polarization control method with excellent comparison between measured and simulated spectra. In conclusion the polarization control method developed in this study is a very powerful tool for UV writing of highly advanced Bragg gratings in optical waveguides.

The novelty of the work on planar waveguides is limited and no publications were produced on this subject. The results are clear though and it can be concluded that the planar waveguides produced in this study were of excellent quality. This conclusion is supported by the very good accordance between simulated and measured transmission and reflection spectra of Bragg gratings with uniform, Gaussian and raised Gaussian profiles. Bragg gratings were written in deuterium sensitized waveguides loaded at a pressure of either standard pressure (100 bar) or ultra high pressure (1800 bar). An annealing experiment showed that the stability of the induced refractive index change is similar for the standard and ultra high pressure loaded samples. The increased photosensitivity at the higher deuterium concentration in the core is thus very useful in order to reduce fabrication time, while still obtaining a high index modulation.

A comparison of the photosensitivity of germanosilicate waveguides when exposed by 244 nm or 266 nm continuous-wave light was made. The dominant absorption band responsible for the UV induced changes in the refractive index peaks around 242 nm. It was concluded that the higher power available in the turn-key 266 nm solid-state laser compensates for the reduced photosensitivity at this wavelength when writing Bragg gratings in deuterium loaded optical fibers. In non-sensitized waveguides the use of lasers operating at wavelength close to the absorption peak is still far more efficient than the 266 nm laser.

8.1 Outlook

The polarization control method is now developed to a level, where only minor improvements are needed. The primary candidate for the remaining problems is the low beam quality of the excimer laser used in the inscription, but also nonlinearities and a small but finite polarization dependence in the photosensitivity will influence the result. The focus in the continued effort on the polarization control method has recently shifted from the implementation to the use of the method. The design and writing of Bragg gratings with specific spectral properties may be the main subject for the time to come. Especially low-dispersion gratings and sampled gratings are interesting applications, where the method can prove its capacity. The amplitude response of a sampled grating consists of a number of equally spaced reflection peaks thus making sampled gratings interesting for WDM purposes. For dense WDM systems the spectral shape of the individual peaks is important. The Fourier analysis presented in the theory shows that a sinc apodization of the overall grating profile results in a square filter response of the individual peaks. The polarization control method may hence be used to write sampled gratings with excellent spectral properties for use in dense WDM systems.
Transferring the method to a continuous-wave laser setup with a high coherence beam also has a high priority in order to improve the quality of the written gratings. An additional advantage of this laser is the possibility of focusing the beam to a very small spot size. This will allow for a reduction of the

spacing between adjacent phase shifts in the gratings and will thus give more freedom in the grating design. Furthermore, it will be interesting to apply a sinc apodization to the individual peaks in a sampled grating thus giving a uniform peak reflection.
Using the polarization control method to write advanced Bragg gratings in planar waveguides is evidently also very interesting. The combination of Bragg gratings with specific spectral properties and other integrated functionalities will open up for a number of opportunities.

Appendix A

Uncertainty of Δn_{eff} and n_{mod}

This appendix addresses the uncertainty in the growth curves showing the measurement of the change in the effective refractive index, Δn_{eff}, or the growth of the refractive index modulation amplitude, n_{mod}, during a UV exposure. In general the errors that introduce the uncertainty in the measurements can be divided into two categories. One is the error on the accuracy of the measurement, which is related to any systematic errors, the other is the precision of the measurement. In the following text the uncertainty in the two types of growth curves are described in individual sections.

A.1 Effective refractive index

The accuracy of the measurement is correlated to any systematic errors, which for instance could originate from the evaluation of the mode index prior to the UV exposure. The extrapolation of the Bragg wavelength data down to the zero fluence limit introduces a constant error in the measurement of Δn_{eff}. This will cause a shift in the position of the growth curve, but the actual shape of the Δn_{eff}-curve is not influenced. The accuracy of the measurement is also affected by other errors such as poor alignment of the phase mask. When this happens the actual periodicity of the refractive index modulation profile differs form the expected. This error scales with $\cos\theta$, where θ is the angle between the waveguide and the grating normal. As long as θ is below 10^{o} the contribution form poor phase mask alignment is less than 2%.

The precision of the Bragg wavelength measurement of a high quality grating is primarily set by the resolution of the spectrum analyzer, which is 0.01 nm when using the ANDO6317B spectrum analyzer together with an ASE source. When the ASE source is replaced by a tunable laser source (ANDO4321D) the resolution is improved to a level better than 0.003 nm. Figure A.1 shows the spectrum of a Bragg grating written in a HNLF fiber using the frequency doubled argon-ion laser operating at 244 nm. The wavelength range spanned with an uncertainty in the measurement of ± 0.01 nm is indicated in the graph. For gratings with a far from ideal spectrum the determination of the Bragg wavelength can be attached with an uncertainty well above 0.01 nm.

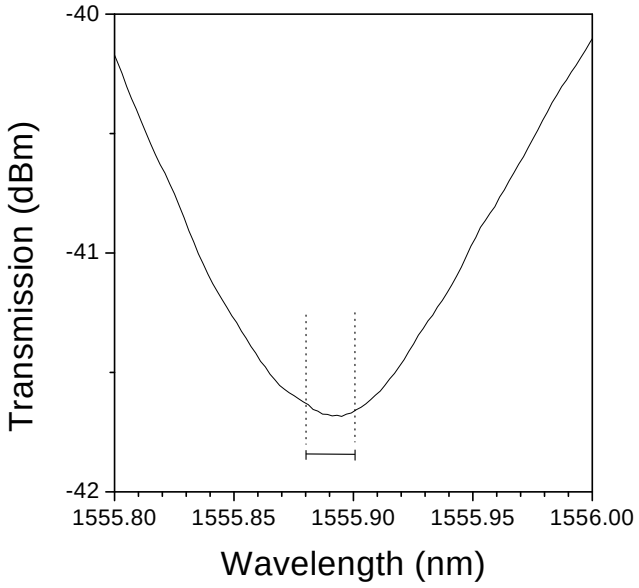

Figure A.1: The change in the effective refractive index during UV exposure is determined from the Bragg wavelength of the grating. The uncertainty in the measurement is set by the resolution of the spectrum analyzer, which in this case is 0.01 nm. The Bragg wavelength of this grating equals 1555.89 ± 0.01 nm.

The temperature dependence of the refractive index of silica glass should also be considered since the waveguide is heated during the exposure. In general all measurements on a growth curve should be made under the same conditions. If the laser beam is blocked/turned off prior to the individual measurements a constant time interval from light off to measurement should be maintained. This will also prevent errors from short-lived defects [87] to interfere with the measurements. Imprecise measurement of the pulse fluence of the excimer laser or the irradiance of the beam from a cw laser also introduces an uncertainty in the growth curves corresponding to a scaling of the x-axis of the graph.

A.2 Refractive index modulation amplitude

The amplitude of the refractive index modulation profile is determined by comparing the measured transmission spectra with simulated spectra. The precision of this method evidently relies on the quality of the grating and how well we can compare it with simulations. An example of the precision of this approach is given in Figure A.2, which shows a comparison between the measured and simulated transmission spectrum of a 12.5 mm uniform grating written in a planar waveguide. From this figure the uncertainty is estimated to be less than $\pm 1\%$. Throughout this thesis the precision in the n_{mod} growth curves is smaller than the points used to present the measured values.

The accuracy of the measurement of n_{mod} is determined by a number of factors.

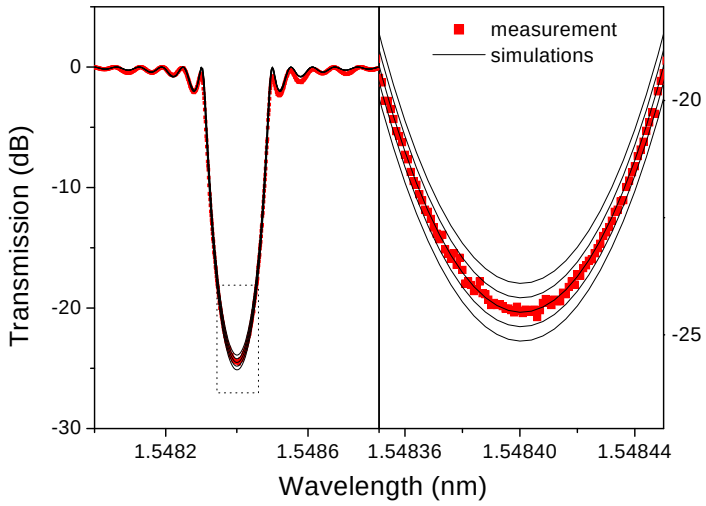

Figure A.2: The refractive index modulation amplitude is determined by comparing the measured transmission spectrum with simulated spectra. The simulated spectra are calculated using $n_{\mathrm{mod}} \times 10^4 = 1.94$, 1.96, 1.98, 2.00, and 2.02, with the latter giving the strongest grating. The right-hand-side graph shows a close-up of the part of the spectrum marked with a box on the left-hand-side graph. The uncertainty in the measurement of n_{mod} is evidently in the order of $\pm 0.02 \times 10^{-4}$ for this particular grating.

Any uncertainty in the evaluation of the grating length, the confinement factor of the guided mode, the beam width and intensity, the deuterium concentration, the temperature of the waveguide and so forth influences the accuracy. Especially in optical waveguides with a highly nonlinear growth curve small changes in the writing conditions may cause large deviations from one growth curve to another. The changes are usually in to order of 10 % but may be as high as 50 % in extreme cases [22]. The magnitude of the error bars related to the accuracy of a specific growth curve is very difficult to determine and it has been omitted in all n_{mod} growth curves presented in this thesis. For the dispersion reduced gratings written using the polarization control method the deviation from the expected modulation amplitude can cause significant degradation of the spectral properties of the grating. For a grating such as the one presented in Figure 6.23 a 20 % reduction of n_{mod} will reduce the side lobe suppression by more than 10 dB.
Some steps may be taken to minimize the problem. Regarding the evaluation of the grating length, a comparison between measured and simulated grating spectra can be used to determine the length with a relatively good accuracy. Alternatively a slit of a well known width should be used to define the grating length. For fibers such as the deuterium loaded HNLF fiber a pre-exposure, which raises the fiber from a highly nonlinear regime into a linear regime on the growth curve also improves the accuracy of the measurement. Performing a large number of growth curves to extract an averaged growth curve will also

reduce the problem slightly. For industrial applications a good rule-of-thumb is never to change anything in a running setup. The beam shaping optics should be kept in the same position at all times and the fiber and phase mask positioning must be identical for every exposure. The same deuterium concentration in the core of the waveguide during the exposure is also required. This is ensured by using identical loading pressure, temperature and time, equivalent duration of the period from the removal of fiber from the pressure chamber or freezer to the start of the exposure and a constant temperature in the laboratory.

Bibliography

[1] K.O. Hill, Y. Fujii, D.C. Johnson, and B.S. Kawasaki. "Photosensitivity in optical waveguides; Application to reflection filter fabrication". *Appl. Phys. Lett.*, **32** (10), pp. 647-649 (1978).

[2] M.J. Cole, W.H. Loh, R.I. Laming, M.N. Zervas, and S. Barcelos. "Moving fibre/phase mask-scanning beam technique for enhanced flexibility in producing fibre gratings with uniform phase mask". *Electron. Lett.*, **31**, pp. 1488-1490 (1995).

[3] R. Feced, M.N. Zervas, and M.A. Muriel. "An efficient inverse scattering algorithm for the design of nonuniform fiber Bragg gratings". *IEEE Jour. of Quantum Electron.*, **35** (8), pp. 1105-1114 (1999).

[4] L. Poladian. "Simple grating synthesis algorithm". *Opt. Lett.*, **25**, pp. 787-789 (2000).

[5] M. Ibsen, M.K. Durkin, M.J. Cole, and R.I. Laming. "Optimised square passband fibre Bragg grating filter with in-band flat group delay response". *Electron. Lett.*, **34** (8), pp. 800-802 (1998).

[6] M. Ibsen, P. Petropoulos, M.N. Zervas, and R. Feced. "Dispersion-free fibre Bragg gratings". in OSA *Trends in Optics and Photonics (TOPS) Vol 54, Optical Fiber Communication Conference,* Technical Digest, Postconference Edition (Optical Society of America, Washington DC, 2001), pp. MC1/1-MC1/3.

[7] J.B. Jensen, N. Plougmann, H.-J. Deyerl, P. Varming, J. Hübner, and M. Kristensen. "Polarization control method for UV writing of advanced Bragg gratings". *Opt. Lett.*, 27 (12), pp. 1004-1006 (2002).

[8] H.-J. Deyerl, N. Plougmann, J.B. Jensen, J. El-Bez, H.R. Sørensen, C. Peucheret, and M. Kristensen. "Low-dispersion fibre Bragg gratings written using the polarization control method". to be presented at *ECOC2002, European Conference on Optical Communication (2002),* Paper No. 07.2.7.

[9] P. Varming, V.C. Lauridsen, J.H. Povlsen, J.B. Jensen, M. Kristensen, and B. Pálsdóttir. "Design and fabrication of Bragg grating based DFB fiber lasers operating above 1610 nm". in OSA *Trends in Optics and Photonics (TOPS) Vol 37, Optical Fiber Communication Conference,* Technical

Digest, Postconference Edition (Optical Society of America, Washington DC, 2000), pp. ThA6/1-ThA6/3.

[10] A. Othonos and K. Kalli. *Fiber Bragg Gratings.* Artech House, (1999).

[11] R. Kashyap. *Fiber Bragg Gratings.* Optics and Photonics. Academic Press, (1999).

[12] J.C. Knight, J. Broeng, T.A. Birks, and P.St.J. Russell. "Photonic band gap guidance in optical fibers". *Science*, **282** (5393), pp. 1476-1478 (1998).

[13] K. Okamoto, K. Syuto, H. Takahashi, and Y. Ohmori. "Fabrication of 128-channel arrayed-waveguide grating multiplexer with 25 Ghz channel spacing". *Electron. Lett.*, **32** (16), pp. 1474-1475 (1996).

[14] R. Syms and J. Cozens. *Optical Guided Waves and Devices.* McGraw-Hill Book Company, (1992).

[15] F. Ladouceur and J.D. Love. *Silica-based Buried Channel Waveguides and Devices.* Optical and Quantum Electronics. Chapman & Hall, (1996).

[16] A.G. Agrawal. *Fiber-Optic Communication Systems.* Wiley Series in Microwave and Optical Engineering. John Wiley & Sons, Inc., (1997).

[17] M.O. Berendt. *Gratings in passive and active optical waveguides.* PhD thesis, Research Center COM, DTU, (1999).

[18] B. Malo, J. Albert, K.O. Hill, F. Bilodeau, and D.C. Johnson. "Effective index drift from molecular hydrogen diffusion in hydrogen-loaded optical fibres and its effect on Bragg grating fabrication". *Electron. Lett.*, **30** (5), pp. 442-444 (1994).

[19] N. Plougmann. *Advanced techniques for fabricating Bragg gratings.* Master thesis, Research Center COM, DTU, (2001).

[20] Kymata Netherlands, Selene 4.2, (http://www.kymata.nl).

[21] D.P. Hand and P.St.J. Russell. "Photoinduced refractive index changes in germanosilicate optical fibers". *Opt. Lett.*, **15** (2), pp. 102-104 (1990).

[22] M. Kristensen. "Ultraviolet-light-induced processes in germanium-doped silica". *Phys. Rev. B*, **64**, pp. 144201 (2001).

[23] J.P. Bernardin and N.M. Lawandy. "Dynamics of the formation of Bragg gratings in germanosilicate optical fibers". *Opt. Commun.*, **79**, pp. 194 (1990).

[24] I. Riant, S. Borne, P. Sansonetti, and B. Poummellec. "Evidence of densification in UV-written Bragg gratings in fibers". in *Photosensitivity and Quadratic Nonlinearity in Waveguides: Fundamentals and Applications*, Vol 22, 1995 OSA Technical Digest Series (Optical Society of America, Washington DC, (1995):51–55.

[25] M. Douay, W.X. Xie, T. Taunay, P. Bernage, P. Niay, P. Cordier, B. Poummelec, L. Dong, J.F. Bayon, H. Poignant, and E. Delevaque. "Densification involved in the UV based photosensitivity of silica glasses and optical fibers". *Jour. of Lightwave Technol.*, **15** (8), pp. 1329-1342 (1997).

[26] P.Y. Fonjallaz, H.G. Limberger, R.P. Salathe, F. Cochet, and B. Leuenberger. "Tension increase correlated to refractive-index change in fibers containing UV-written Bragg gratings". *Opt. Lett.*, **20** (11), pp. 1346-1348 (1995).

[27] T.E. Tsai, G.M. Williams, and E.J. Friebele. "Index structure of fiber Bragg gratings in Ge-SiO_2 fibers". *Opt. Lett.*, **22** (4), pp. 224-226 (1997).

[28] H. Hosono, Y. Abe, D.L. Kinser, R.A. Weeks, K. Muta, and H. Kawazoe. "Nature and Orgigin of the 5-eV band in SiO_2:GeO_2 glasses". *Phys. Rev. B*, **46** (18), pp. 11445-11451 (1992).

[29] V. Grubsky, D.S. Starodubov, and J. Feinberg. "Photochemical reaction of hydrogen with germanosilicate glass initiated by 3.4-5.4-eV ultraviolet light". *Opt. Lett.*, **24** (11), pp. 729-731 (1999).

[30] J.-L. Archambault, L. Reekie, and P.St.J. Russell. "100% reflectivity Bragg reflectors produced in optical fibres by single excimer laser pulses". *Electron. Lett.*, **29** (5), pp. 453-455(1993).

[31] H. Scholze. *Glass: Nature and Structure of Glass.* Springer, (1990).

[32] M. J. Yuen. "Ultraviolet absorption studies of germanium silicate glasses". *Appl. Opt.*, **21**, pp. 136-140 (1982).

[33] D.S. Starodubov, V. Grubsky, J. Feinberg, B. Kobrin, and S. Juma. "Bragg grating formation in germanosilicate fibers by use of near-UV light: a new pathway for refractive index changes". *Opt. Lett.*, **22** (14), pp. 1086-1088 (1997).

[34] J. Nishii, K. Fukumi, H. Yamanaka, K. Kawamura, H. Hosono, and H. Kawazoe. "Photochemical reactions in GeO_2-SiO_2 glasses induced by ultraviolet irradiation: Comparision between Hg lamp and excimer laser". *Phys. Rev. B*, **52**, pp. 1661-1665 (1995).

[35] R.M. Atkins, V. Mizrahi, and T. Erdogan. "248 nm induced vacuum UV spectral changes in optical fibre preform cores: support for a colour centre model of photosensitivity". *Electon. Lett.*, **29**, pp. 385-387 (1993).

[36] P.J. Lemaire, R.M. Atkins, V. Mizrahi, and W.A. Reed. "High Pressure H_2 loading as a technique for achieving ultrahigh UV photosensitivity and thermal sensitivity in GeO_2 doped optical fibres". *Electron. Lett.*, **29** (13), pp. 1191 (1993).

[37] P.J. Lemaire. "Reliability of optical fibers exposed to hydrogen: prediction of long-term loss increases". *Opt. Eng.*, **30** (6), pp. 780-789 (1991).

[38] J.F. Schakelford, P.L. Studt, and R.M. Fulrath. "Solubility of gasses in glass. II. He, Ne, and H_2 in fused silica". *Jour. Appl. Phys.*, **43** (4), pp. 1619-1626 (1972).

[39] T. Erdogan, V. Mizrahi, P.J. Lemaire, and D. Monroe. "Decay of ultraviolet-induced fiber Bragg gratings". *Jour. of Appl. Phys.*, **76** (1), pp. 73-80 (1994).

[40] H. Hosono, M. Mizuguchi, H. Kawazoe, and J. Nishii. "Correlation betweeen GeE' centers and optical absorption bands in SiO_2:GeO_2 glasses". *Jap. Jour. of Appl. Phys.*, **35**, L235-236 (1996).

[41] L. Dong, J.L. Archambault, L. Reekie, P.St.J. Russell, and D.N. Payne. "Photoinduced absorption change in germanosilicate preforms: evidence for the color-center model of photosensitivity". *Appl. Opt.*, **34** (18), pp. 3436-3440 (1995).

[42] C. Fiori and R.A.B. Devine. "Ultraviolet irradiation induced compaction and photoetching in amorphous thermal SiO_2". *Materials Research Society Symposium Proceedings*, **61**, pp. 187-195 (1986).

[43] R.M. Atkins. "Measurement of the ultraviolet absorption spectrum of optical fibers". *Opt. Lett.*, **17** (7), pp. 469-471 (1992).

[44] M. Svalgaard. *Ultraviolet light induced refractive index structures in germanosilica.* Ph.d. thesis, Microelectronic Center, DTU, (1997).

[45] J. Martin and F. Ouellette. "Novel writing technique of long and highly reflective in-fibre gratings". *Electron. Lett.*, **30**, pp. 811 (1994).

[46] J.B. Jensen, P. Varming, B. Liu, and W. Gries. "Comparison of Photosensitivity in Germanium Doped Silica Fibers using 244nm and 266nm Continuous-Wave Lasers". in OSA *Trends in Optics and Photonics (TOPS) Vol 54, Optical Fiber Communication Conference,* Technical Digest, Postconference Edition (Optical Society of America, Washington DC, 2001), pp. WDD90/1-WDD90/3.

[47] T. Komukai and M. Nakazawa. "Fabrication of high-quality long-fiber bragg grating by monitoring 3.1-eV radiation (400nm) from Ge0 defects". *IEEE Photon. Tech. Lett.*, **8** (11), pp. 1495-1497 (1996).

[48] H. Patrick and S. L. Gilbert. Growth of Bragg gratings produced by continuous-wave ultraviolet light in optical fiber. *Opt. Lett.*, **18** (18), pp. 1484-1486 (1993).

[49] T. Erdogan. "Fiber grating spectra". *Jour. of Lightwave Technol.*, **15** (8), pp. 1277-1249 (1997).

[50] A. Yariv. "Coupled-mode theory for guided-wave optics". *IEEE Jour. of Quantum Electron.*, Vol. QE-9, pp. 919-933 (1973).

[51] H. Kogelnik. "Filter response of nonuniform almost-periodic structures". *Bell System Technical Journal*, **55**, pp. 109-126 (1976).

[52] M. Yamada and K. Sukada. "Analysis of almost-periodic distributed feedback slab waveguides via a fundamental matrix approach". *Appl. Opt.*, **26** (16), pp. 3474-3478 (1987).

[53] S.W. Smith. *The Scientist and Engineer's Guide to Digital Signal Processing.* California Technical Publishing, (http://www.dspguide.com).

[54] M. Ibsen, J. Hübner, J.E. Pedersen, R. Kromann, L.-U.A. Andersen, and M. Kristensen. "30 dB sampled gratings in germanosilicate planar waveguides". *Electron. Lett.*, **32** (24), pp. 2233-2235 (1996).

[55] W. Chin-Hua, L.R. Chen, and P.W.E. Smith. "Analysis of chirped-sampled and sampled-chirped fiber Bragg gratings". *Appl. Opt.*, **41** (9), pp. 1654-1660 (2002).

[56] J. Hübner. *Index Engineering with Excimer Light.* PhD thesis, Microelectronik Centret, DTU, (1998).

[57] E. Zanger, R. Mueller, B. Liu, M. Koetteritzsch, and W. Gries. "Diode-pumped high-power cw all solid-state laser at 266nm". in *Proceedings of the 1999 Solid State Lasers VIII, SPIE Vol. 3613*, pages 184–189, (1999).

[58] G. Meltz, W.W. Morey, and W.H. Glenn. "Formation of Bragg gratings in optical fibres by transverse holographic method". *Opt. Lett.*, **14** (15), pp. 823-825 (1989).

[59] K.O. Hill, B. Malo, F. Bilodeau, D.C. Johnson, and J. Albert. "Bragg gratings fabricated in monomode photosensitive optical fiber by UV exposure through a phase mask". *Appl. Phys. Lett.*, **62** (10), pp. 1035-1037 (1993).

[60] B. Malo, S. Thériault, D.C. Johnson, F. Bilodeau, J. Albert, and K.O. Hill. "Apodised in-fibre Bragg grating reflectors photoimprinted using a phase mask". *Electron. Lett.*, **31** (3), pp. 223-225 (1995).

[61] J.J. Pan and Y. Shi. "Steep skirt fibre Bragg grating production using a new apodised phase mask". *Electron. Lett.*, **33** (22), pp. 1895-1896 (1997).

[62] R. Kashyap, P.F. McKee, and D.J. Armes. "UV written reflection grating structures in photosensitive optical fibres using phase-shifted phase-masks". *Electron. Lett.*, **30** (23), pp. 1977-1978 (1994).

[63] J. Canning and M.G. Sceats. "π-phase-shifted periodic dristibuted structures in optical fibres by UV post-processing". *Electron. Lett.*, **30**, pp. 1977-1978 (1994).

[64] M. Ibsen, M.K. Durkin, M.J. Cole, and R.I. Laming. "Sinc-Sampled Fiber Bragg Gratings for Identical Multiple Wavelength Operation". *IEEE Photon. Tech. Lett.*, **10** (6), pp. 842-844 (1998).

[65] P. Varming, J.B. Jensen, N. Plougmann, M. Kristensen, and J. Hübner. "New and simple method for fabrication of advanced UV written Bragg gratings". in *Bragg Gratings, Photosensitivity, and Poling in Glass Waveguides,* OSA Technical Digest, Optical Society of America, Washington DC, 2001, pp. BWA5/1-BWA5/3*).*

[66] E. Hecht. *Optics.* Addison-Wesley, third edition, (1998).

[67] N. Plougmann. Unpublished.

[68] Optiwave Corporation, IFO Gratings 4.0, (http://www.optiwave.com).

[69] G. Lenz, B.J. Eggleton, C.K. Madsen, C.R. Giles, and G. Nykolak. "Optimal dispersion of optical filters for WDM systems". *IEEE Photon. Technol. Lett.*, **10** (4), pp. 567-569 (1998).

[70] J.E. Sipe, B.J. Eggleton, and T.A. Strasser. "Dispersion characteristics of nonuniform Bragg gratings: Implications for WDM communication systems". *Opt. Comm.*, **152**, pp. 269-274 (1998).

[71] F. Ouellette, D. Gagnon, and M. Poirier. "Permanent photoinduced birefringence in a Ge-doped fiber". *Appl. Phys. Lett.*, **58**, pp. 1813-1815 (1991).

[72] T. Erdogan and V. Mizrahi. "Characterization of UV-induced birefringence in photosensitive Ge-doped silica optical fibers". *Jour. Opt. Soc. Am. B*, **11**, pp. 2100-2105 (1994).

[73] M. Poirier, S. Thibault, J. Lauzon, and F. Ouellette. "Dynamic and oriental behavior of UV-induced luminescence bleaching in Ge-doped silica optical fiber". *Opt. Lett.*, **18**, pp. 870-872 (1993).

[74] T. Meyer, P.-A. Nicati, P.A. Robert, D. Varelas, H.-G. Limberger, and P. Salath. "Reversibility of Photoinduced Birefringence in Ultralow-birefringence Fibers". *Opt. Lett.*, **21** (20), pp. 1661-1663 (1996).

[75] N. Plougmann, C. Zhang, and H.-J. Deyerl. Unpublished.

[76] C. Zhang. Unpublished.

[77] J. Albert, K.O. Hill, B. Malo, S. Thériault, F. Bilodeau, D.C. Johnson, and L.E. Erickson. "Apodisation of the spectral response of fibre Bragg gratings using a phase mask with variable diffraction efficiency". *Electron. Lett.*, **31** (3), pp. 222-223(1995).

[78] R. Kashyap, A. Swanton, and D.J. Armes. "Simple method for apodising chirped and unchirped fibre Bragg gratings". *Electron. Lett.*, **32**, pp. 1226-1228 (1996).

[79] H.-G. Fröhlich and R. Kashyap. "Two methods of apodization of fibre-Bragg-gratings". *Opt. Comm.*, **157**, pp. 273-281 (1998).

[80] H. Storøy, H.E. Engan, B. Sahlgren, and R. Stubbe. "Position weighting of fiber Bragg gratings for bandpass filtering". *Opt. Lett.*, **22** (11), pp. 784-786 (1997).

[81] W.H. Loh, M.J. Cole, M.N. Zervas, S. Barcelos, and R.I. Laming. "Complex grating structures with uniform phase masks based on the moving fiber-scanning beam technique". *Opt. Lett.*, **20** (20), pp. 2051-2053 (1995).

[82] D.A. Zauner. *Integrated optical devices for wavelength division multiplexing using PECVD and direct UV-writing techniques.* Ph.d. thesis, Microelectronic Center, DTU, (1999).

[83] I.H. Malitson. "Interspecimen comparison of the refractive index of fused silica". *J. Opt. Soc. Am.*, **15** (10), pp. 1205-1209 (1965).

[84] J. Fleming. "Dispersion in GeO_2-SiO_2 glasses". *Appl. Opt.*, **23** (4), pp. 4486 (1984).

[85] H.G. Limberger, P.Y. Fonjallaz, and R.P. Salath. "UV induced stress changes in optical fibers". in *Photosensitivity and Quadratic Nonlinearity in Waveguides: Fundamentals and Applications*, Vol 22, 1995 OSA Technical Digest Series (Optical Society of America, Washington DC, 1995):pp. 56–60.

[86] J.F. Brennan III, D. Sloan, M. May, and D.L. LaBrake. "The photosensitivity and UV-induced loss of silica optical fibers exposed to very high-pressure hydrogen environments". *SPIE*, **3847**, pp. 42-47 (1999).

[87] J. Canning. "Photosensitivity in Si/SiO_2-Based Planar Waveguides". in *proceedings of the Euro-Summer School on Photosensitivity in Optical Waveguides and Glasses, POWAG2000*, Giens Peninsula (Toulon), Var, France (2000).